RCA REVIEW

a technical journal

RADIO AND ELECTRONICS
RESEARCH • ENGINEERING

Published quarterly by
RCA LABORATORIES
in cooperation with all subsidiaries and divisions of
RADIO CORPORATION OF AMERICA

VOLUME XXIII | MARCH 1962 | NUMBER 1

CONTENTS

RCA REVIEW is regularly abstracted and indexed by *Applied Science and Technology Index, Bulletin Signalétique des Télécommunications, Chemical Abstracts, Electronic and Radio Engineer, Mathematical Reviews,* and *Science Abstracts* (I.E.E.-Brit.).

RCA REVIEW

BOARD OF EDITORS

STABLE LOW-NOISE TUNNEL-DIODE FREQUENCY CONVERTERS*

By

F. Sterzer and A. Presser

RCA Electron Tube Division
Princeton N. J.

Summary—Experimental UHF and microwave tunnel-diode frequency converters that are stable with input VSWR's exceeding 10:1 are described. Conversion losses (~0 decibels) and noise figures (2.5 to 3 decibels) of these converters are lower than can be obtained with conventional crystal-diode converters. The Fourier coefficients of the conductance and of the equivalent shot-noise currents of a germanium tunnel-diode converter are given for a wide range of bias voltages and local-oscillator amplitudes; thus conversion gain and noise figure can be calculated by use of the classical theory of nonlinear-conductance frequency converters.

Introduction

PRACTICALLY all existing low-noise UHF and microwave receivers make use of the heterodyne principle, i.e., the frequency of the received signal is shifted before high amplification takes place. For frequencies above a few hundred megacycles, crystal diodes are almost universally used in the frequency converters of such receivers. However, the best UHF crystal converters have conversion losses of 3 to 4 decibels and noise figures of 4 to 5 decibels; at microwave frequencies, both conversion losses and noise figures are somewhat higher. Until the recent advent of very-low-noise preamplifiers such as masers, parametric amplifiers, and traveling-wave tubes, crystal frequency converters were generally placed directly at the input of the receiver. Now a low-noise preamplifier is placed ahead of the crystal if very low receiver noise figures are desired.

There is little likelihood that the noise figure of crystal mixers can be significantly improved by further research. Crystal diodes, which are passive devices, must have some conversion loss, and their noise figure must always equal or exceed this loss. Recently, however, microwave diodes with a negative-resistance region (tunnel diodes) have become available. These diodes, whose unique properties depend on quantum mechanical tunneling, exhibit active properties even at millimeter-wave frequencies.[1]

* Manuscript received 26 January 1962.

[1] C. A. Burrus, "Millimeter Wave Esaki Diode Oscillator," *Proc. I.R.E.*, Vol. 48, p. 2024, December 1960.

Although crystal-diode converters must have conversion loss, tunnel-diode converters can have arbitrarily large conversion gain. K. K. N. Chang and his co-workers at RCA Laboratories were apparently the first to recognize this fact and demonstrate it.[2] They also derived expressions for the gain and noise figure of tunnel-diode converters. This paper* differs in two important respects from the pioneering work of Chang et al. First, in Chang's theory the current–voltage characteristic of the tunnel diode was approximated by a second-degree power series. This particular approximation yields valid results for gain and noise figure when the diode is biased near its peak current, and when the local-oscillator amplitude is limited to a few millivolts. For bias points near the valley of the diode or for large local-oscillator swings, however, the second-order approximation is inadequate. In this paper, the current–voltage characteristic of the diode and its shot noise current–voltage characteristic are approximated by tenth-degree power series, and a theory is developed for a wide range of bias points and for local-oscillator amplitudes up to a few hundred millivolts.

In addition, Chang's high-gain converters were sensitive to variations in input impedance. This paper, on the other hand, describes low-gain tunnel-diode frequency converters that are exceptionally stable with variations in input impedance. These stable converters have lower conversion loss, lower noise figures, larger dynamic range, and greater resistance to burn-out than crystal-diode converters; their use could eliminate the need for preamplifiers in many applications.

Equivalent Circuit of Tunnel-Diode Frequency Converter

Because of the great practical importance of heterodyne reception, much effort has been devoted in the past to the theory of mixing in nonlinear-conductance devices.[3-8] Most of this theory dates back to the 1930's and 1940's; it is, therefore, almost exclusively concerned

---

[2] K. K. N. Chang, G. H. Heilmeier and H. J. Prager, "Low-Noise Tunnel-Diode Down Converter Having Conversion Gain," *Proc. I.R.E.*, Vol. 48, p. 854, May 1960.

* Most of the material contained in this paper was first presented by the authors at the Western Electronic Show and Convention, San Francisco, August, 1961. See also F. Sterzer and A. Presser, "Stable Low-Noise Tunnel-Diode Frequency Converter," *Proc. I.R.E.*, Vol. 49, p. 1318, August 1961 and p. 1572, October 1961.

[3] M. J. O. Strutt, "Diode Frequency Changers," *Wireless Eng.*, Vol. 13, p. 73, 1936.

[4] E. Peterson and L. W. Hussey, "Equivalent Modulator Circuits," *Bell Syst. Tech. Jour.*, Vol. 18, p. 32, January 1939.

[5] E. W. Herold, "Frequency Mixing in Diodes," *Proc. I.R.E.*, Vol. 31, p. 575, October 1943.

with passive mixers. However, much of the early theory is directly applicable to tunnel-diode frequency converters. For example, Figure 1 shows an equivalent linear circuit, dating back to at least 1939, which is useful for calculating the gain of tunnel-diode mixers.[4]

In a frequency converter, an input signal of frequency f_s and a local-oscillator signal of frequency f_0 are impressed across a nonlinear device. In general, a complete set of sideband frequencies is produced, i.e., all frequencies $f_{m,n} = mf_s + nf_0$ (m and n take on all integral values) are present. However, in most practical nonlinear-conductance

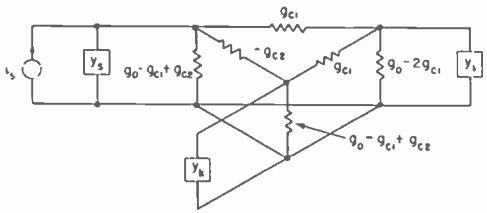

Fig. 1—Equivalent linear three-port frequency-translation network for tunnel-diode frequency converter.

converters, significant power flow takes place only at the input-signal frequency f_s, the oscillator-frequency f_0, the intermediate frequency f_i ($= |f_s - f_0|$), and the image frequency f_k ($= |2f_0 - f_s|$). In this case, the nonlinear-conductance converter can be represented by the linear three-port frequency-translation network shown in Figure 1, provided that the amplitude of the sinusoidal local-oscillator voltage across the nonlinear resistor is much greater than the sum of the amplitudes of the voltages at signal, intermediate, and image frequencies.[4,6]

In Figure 1, Y_s is the total admittance at the signal frequency connected across the nonlinear conductance; similarly, Y_k and Y_i are, respectively, the total image- and intermediate-frequency admittances. The quantity g_0 is the average value of the nonlinear conductance driven by the sinusoidal local oscillator, g_{c1} is the fundamental conversion conductance, and g_{c2} is the second-harmonic conversion conductance.*

[6] E. W. Herold, R. R. Bush and W. R. Ferris, "Conversion Loss of Diode Mixers Having Image Frequency Impedance," *Proc. I.R.E.*, Vol. 33, p. 603, September 1945.

[7] H. C. Torrey and C. A. Whitmer, *Crystal Rectifiers*, McGraw-Hill Book Company, Inc., New York, 1948.

[8] R. V. Pound, *Microwave Mixers*, McGraw-Hill Book Company, Inc., New York, 1948.

* The equivalent circuit of Figure 1 can also be used to calculate the gain of a converter where the signal mixes with the nth harmonic of the local oscillator ($f_s = |2nf_0 - f_i|$). In this case, g_{c1} and g_{c2} must be replaced by g_{cn} and g_{c2n}, respectively.

Conversion Conductances of Germanium Tunnel Diodes

The quantities g_0, g_{c1}, and g_{c2} were evaluated for a typical germanium tunnel diode by use of the following tenth-degree power series:

$$I = \sum_{n=0}^{10} \alpha_n V^n. \tag{1}$$

The approximate current–voltage characteristic of the diode calculated from this equation, together with the measured characteristics of a

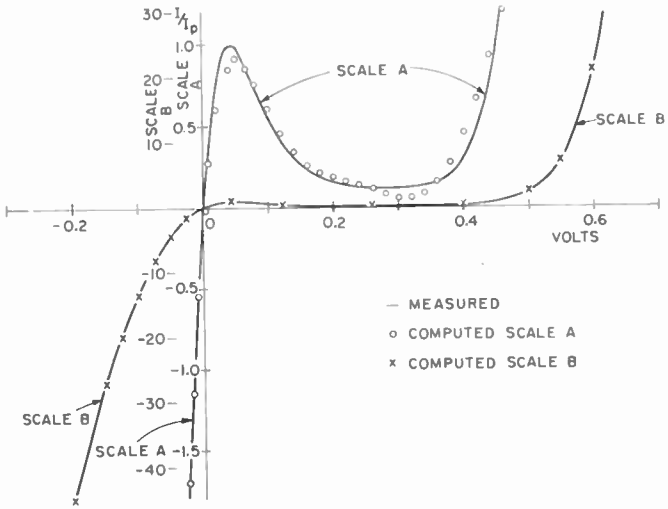

Fig. 2—Normalized current I/I_p of germanium tunnel diode as a function of voltage. Both measured values and values calculated from Equation (1) are shown.

germanium tunnel diode, is shown in Figure 2. These curves indicate that the power series approximates the measured characteristic for bias voltages from —0.2 to +0.6 volt.

The dynamic conductance g of the diode is then given by

$$g = \frac{dI}{dV} = \sum_{n=1}^{10} n\alpha_n V^{n-1}. \tag{2}$$

When the d-c bias voltage, V_B, and the local-oscillator voltage, $V_0 \cos \omega_0 t$, are substituted in Equation (2), the following equation for g is obtained:

$$g = \sum_{n=1}^{10} n\alpha_n (V_B + V_0 \cos \omega_0 t)^{n-1} \tag{3}$$

$$= g_0 + 2g_{c1} \cos \omega_0 t + 2g_{c2} \cos 2\omega_0 t + \ldots .$$

Figure 3 shows curves of g_0, g_{c1}, and g_{c2} as functions of V_0 for several values of V_B, as evaluated from Equation (3).**

The equivalent circuit of Figure 1 and the conductance curves of Figure 3 can also be used to calculate the gain of self-oscillating or autodyne converters,[9] provided the self oscillations are nearly sinusoidal. In this case V_0 must be replaced by the amplitude of the self oscillations.

In practical positive nonlinear-conductance mixers, the following inequalities must always be satisfied:[6]

$$g_0 > 0, \quad g_0 > |g_{c1}|, \quad g_0 > |g_{c2}|. \tag{4}$$

However, these restrictions do not apply to tunnel-diode converters because, as shown in Figure 2, tunnel diodes exhibit a negative conductance over part of their current–voltage characteristic. For example, all three inequalities are reversed in Figure 3(b) for a local-oscillator amplitude of 0.07 volt.

Conversion Gain of Tunnel-Diode Frequency Converters

Expressions for the conversion gain (i.e., the ratio of i-f output power to the available signal power) can be derived from the equivalent circuit shown in Figure 1. If, for simplicity, it is assumed that Y_s, Y_k, and Y_i are pure conductances equal to the internal conductance of the generator g_g, the image conductance g_k, and the load conductance g_i, respectively, then the conversion gain K can be expressed as follows:

$$K = \frac{4g_i g_g M^2}{(g_g + g_{in})^2}, \tag{5}$$

where

** An experimental method for obtaining the fundamental and the harmonic conversion conductances of a tunnel diode is described by B. Christensen, "Measurement of Tunnel-Diode Conductance Parameters," *Proc. I.R.E.*, Vol. 49, p. 1581, October 1961.

[9] F. Sterzer, A. Presser and A. H. Solomon, "Microwave Tunnel Diode Autodyne Receiver," Digest of Technical Papers, *International Solid State Circuits Conference*, Philadelphia, Pa., February 1961.

$$M = \frac{g_{c1}(g_0 + g_k - g_{c2})}{(g_0 + g_k)(g_0 + g_i) - {g_{c1}}^2},$$

and where g_{in}, the input conductance, is given by

$$g_{in} = \frac{{g_{c1}}^2(2g_{c2} - 2g_0 - g_k) - (g_0 + g_i)({g_{c2}}^2 - {g_0}^2 - g_0 g_k)}{(g_0 + g_k)(g_0 + g_i) - {g_{c1}}^2}.$$

Passive converters must have conversion loss, as can be shown by inserting inequality (4) into Equation (5). Tunnel-diode converters, on the other hand, may have conversion gain when any one of the inequalities (4) is reversed. This conversion gain can be made arbitrarily large, and will approach infinity as $-g_{in}$ approaches g_g.

There are three special cases of particular interest:

1. short-circuited image impedance ($g_k = \infty$),
2. open-circuited image impedance ($g_k = 0$),
3. image impedance equal to generator impedance ($g_k = g_g$).

For these special cases Equation (5) takes the following forms:

$$K = \frac{4g_i g_g {g_{c1}}^2}{(g_0 + g_i)^2 (g_g + g_{in})^2} \qquad (6)$$

$$g_k = \infty$$

$$g_{in} = \frac{-{g_{c1}}^2 + g_0(g_0 + g_i)}{(g_0 + g_i)}.$$

$$K = \frac{4g_i g_g {g_{c1}}^2 (g_0 - g_{c2})^2}{({g_0}^2 + g_0 g_i - {g_{c1}}^2)^2 (g_g + g_{in})^2} \qquad (7)$$

$$g_k = 0$$

$$g_{in} = \frac{{g_{c1}}^2(2g_{c2} - 2g_0) - (g_0 + g_i)({g_{c2}}^2 - {g_0}^2)}{{g_0}^2 + g_0 g_i - {g_{c1}}^2}.$$

$$K = 4g_g g_i \left[\frac{g_{c1}}{(g_0 + g_i)(g_{c2} + g_0 + g_g) - 2{g_{c1}}^2} \right]^2 \qquad (8)$$

$$g_k = g_g$$

$$g_{in} = \frac{{g_{c1}}^2(2g_{c2} - 2g_0 - g_g) - (g_0 + g_i)({g_{c2}}^2 - {g_0}^2 - g_0 g_g)}{(g_0 + g_g)(g_0 + g_i) - {g_{c1}}^2}.$$

Equations (5) through (8), when used in conjunction with Figure

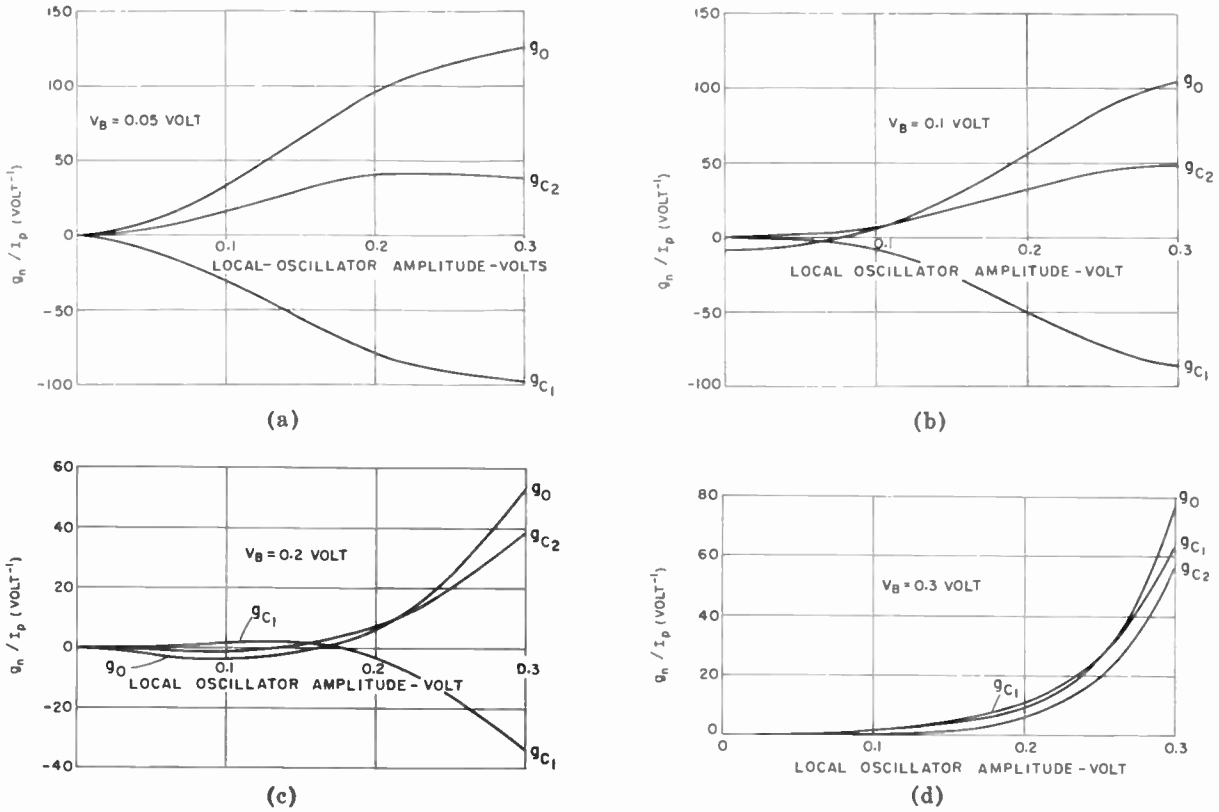

Fig. 3—Curves showing the normalized average conductance, g_0, the normalized fundamental conversion conductance, g_{c1}, and the normalized second-harmonic conversion conductance, g_{c2}, as functions of local-oscillator voltage for four values of d-c bias, V_B. All curves were calculated from the power-series approximation shown in Figure 2.

3, permit direct numerical evaluation of conversion gain, provided that the reactive components of Y_s, Y_k, and Y_t can be neglected. Figure 4 shows two curves of conversion gain as a function of local-oscillator voltage calculated from Equation (8) and Figure 3(a), together with several experimental points. For these curves, $V_B = 0.05$ volt, $Y_s = Y_k = Y_t$, and Y_s/I_p is 20 and 10 volt^{-1}. The maximum calculated conversion gain for $Y_s/I_p = 10$ volt^{-1} is about 4.7 decibels; for $Y_s/I_p = 20$ volt^{-1} the minimum conversion loss is about 2 decibels.

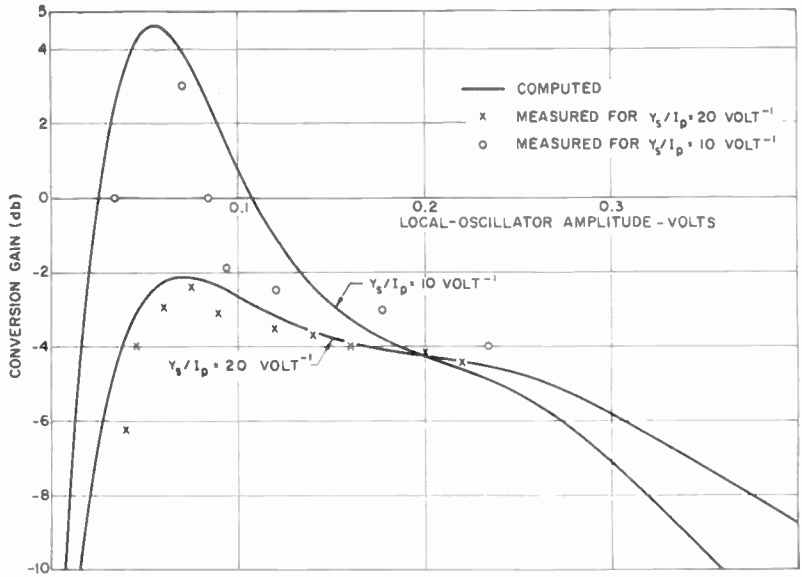

Fig. 4—Measured and computed conversion gain as a function of local-oscillator amplitude for a tunnel-diode frequency converter ($V_B = 0.05$ volt, $Y_s = Y_k = Y_t$).

The experimental points were measured at a signal frequency of 1 megacycle and an i-f frequency of a few kilocycles. At these low frequencies, the parasitic reactances of the diode may be neglected and accurate measurements of local oscillator amplitude and conversion gain are relatively simple.

The agreement between measured and calculated values of conversion gain in Figure 4 is fair. For some values of local-oscillator amplitude, however, the discrepancy between measured and calculated values is about 3 decibels. Similar, and sometimes even larger, discrepancies were observed at other bias points. It appears that most of the observed differences were caused by the internal impedance of

the local oscillator used in the experiments. The values of the Fourier coefficients of $g(t)$ in Figure 3 are calculated for a pure sinusoidal local-oscillator voltage across the diode. In most practical applications, however, the voltage drop across the internal impedance of the local oscillator causes considerable clipping and similar distortion of the local-oscillator voltage across the diode. For example, Figure 5 shows oscilloscope tracings of local oscillator voltages across a 2-milliampere tunnel diode for three values of internal impedance of a sinusoidal local oscillator. For an internal impedance of 2 ohms, the voltage across the diode is nearly sinusoidal (Figure 5a), but for impedances of 50 and 600 ohms, this voltage is strongly nonsinusoidal (Figures 5b and 5c).

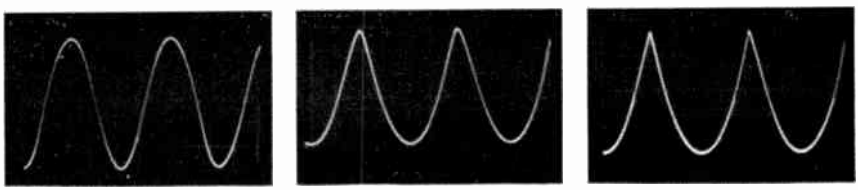

(a) (b) (c)

Fig. 5—Oscilloscope traces of local oscillator voltages across a 2-ma tunnel diode for three values of internal impedance, R_g, of a sinusoidal local oscillator: $V_B = 0$ volt, vertical axis = 0.02 volt/large division, horizontal axis = 10 μsec/large division. (a) $R_g = 2$ ohms, (b) $R_g = 50$ ohms, (c) $R_g = 600$ ohms.

Equation (5) shows that the conversion gain is proportional to $g_g/(g_g + g_{in})^2$. Figure 6 shows the calculated conversion gain of two converters as a function of input admittance. In general, the higher the maximum gain of a converter, the more sensitive is its gain to variations in input impedance.

For a range of bias voltages, the fundamental conversion conductance, g_{c1}, becomes zero for finite values of local-oscillator voltage (see, for example, Figure 3c), and the unusual situation arises where two signals of different frequencies interact simultaneously with a nonlinear device, and yet no difference frequency is produced. Figure 7 shows calculated values of K as a function of local-oscillator amplitude for a tunnel-diode converter biased at 0.15 volt. The conversion gain drops to zero for a local-oscillator amplitude of about 0.105 volt, i.e., at the voltage where $g_{c1} = 0$.

The value of g_{c1} is finite for local-oscillator amplitudes higher or lower than 0.105 volt, and the conversion gain rises from $-\infty$ to about —17 decibels for a voltage change of only 20 millivolts. This

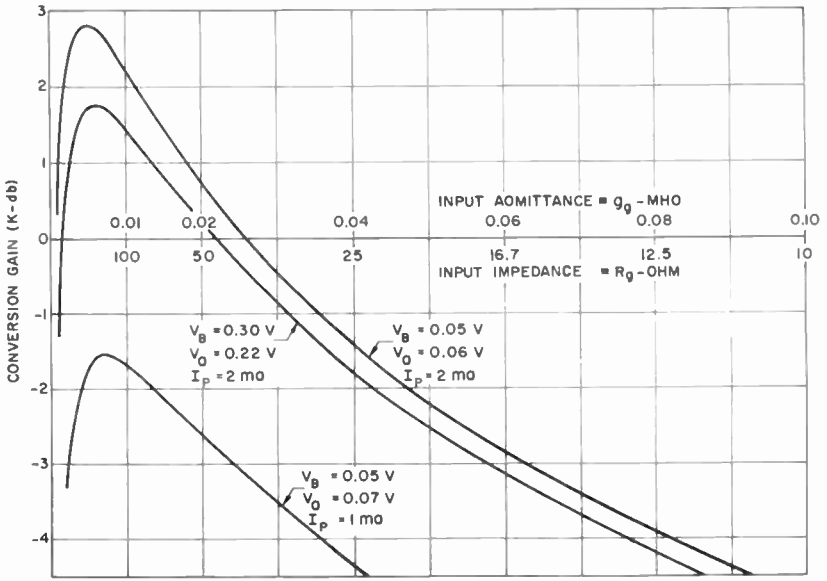

Fig. 6—Computed conversion gain as a function of input admittance for two tunnel-diode frequency converters ($Y_L = \infty$, $g_i = 0.02$ mho). The two upper curves are for a converter using a 2-ma diode, the lower curve for a converter using a 1-ma diode.

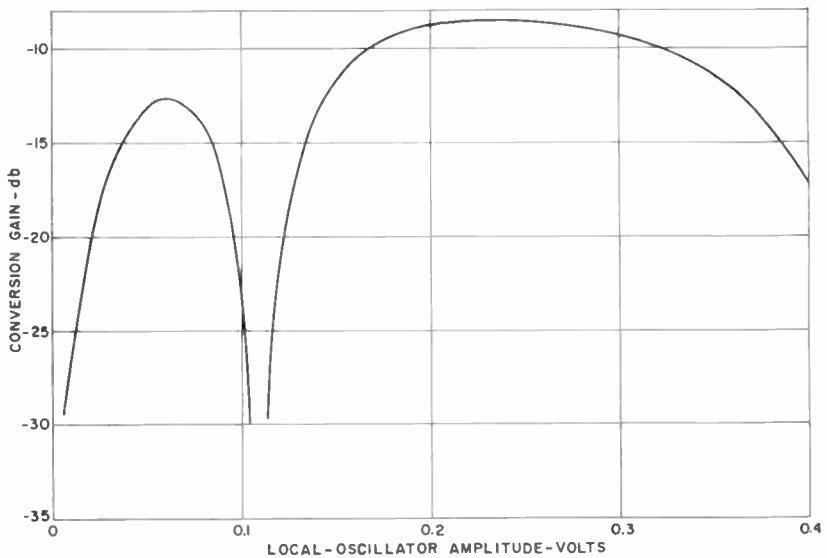

Fig. 7—Calculated conversion gain as a function of local-oscillator amplitude for tunnel-diode frequency converter ($V_B = 0.15$ volt, $g_s/I_p = 100$ volt^{-1}, $g_i/I_p = 10$ volt^{-1}).

effect, which is readily observed experimentally, might be useful in simple r-f amplitude stabilizing circuits.

Bandwidth of Tunnel-Diode Frequency Converters

The conversion gain of a nonlinear-conductance frequency converter containing no reactances is independent of frequency. Tunnel diodes, however, contain parasitic capacitances and inductances, and the gain of tunnel diode frequency converters is therefore frequency dependent. With available tunnel diodes, the effect of these reactances is usually negligible at conventional i-f frequencies ($f_{i\text{-}f} \leq 30$ megacycles), but must be taken into account at UHF and microwave frequencies.

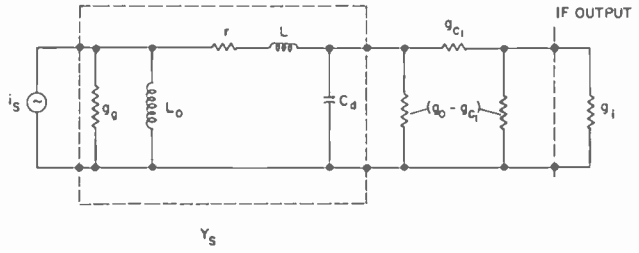

Fig. 8—Equivalent circuit used in the bandwidth calculations of Figures 9-11 ($Y_k = \infty$, $Y_i = g_i$).

An approximate equivalent a-c circuit for an encapsulated tunnel diode consists of three elements connected in series: an inductance L_d, a resistance r_d, and a voltage-dependent resistance $R_d(v)$ $(= 1/g)$ shunted by a voltage-dependent capacitance $C_d(v)$. L_d results mainly from the inductance of the housing; r_d is the resistance of the ohmic contact, the base, and the internal leads of the package, and is a function of frequency due to skin effect. $C_d(v)$ is the junction capacitance,* and $R_d(v)$ is the total a-c resistance of the junction, where v is the voltage across R_d and C_d.

The bandwidth of the converter can be calculated in a straightforward fashion by incorporating r_d, L_d, and C_d into the admittances Y_s, Y_k, and Y_i of the equivalent circuit of Figure 1, and then using this equivalent circuit to calculate gain as a function of frequency. We have carried out a number of bandwidth calculations using the equivalent circuit of Figure 8. Some results of these computations are

* The variations of C_d with voltage may be approximated for voltages less than the valley voltage by $C_d(v) \approx K(\phi - v)^{-1/2}$ where K and ϕ are constants. For germanium, $\phi \approx 0.6$ volt. For a diode driven by a sinusoidal local oscillator, the average value of C_d is approximately equal to the value of C at the bias point.

plotted in normalized form in Figures 9-11. These figures can be used to get an estimate of bandwidth for most diodes used in practical converters. Figure 9 is a graph of calculated conversion gain as a function of $|\omega C_d - 1/\omega L_0|/I_p$ for a converter with $L = r = 0$. Curves corresponding to three values of g_g/I_p are plotted. Figures 10a, b, and c are graphs of correction factors to Figure 9 for several values of L and r. In Figure 11, conversion gain is plotted for four values of L_0 and several values of L and r.

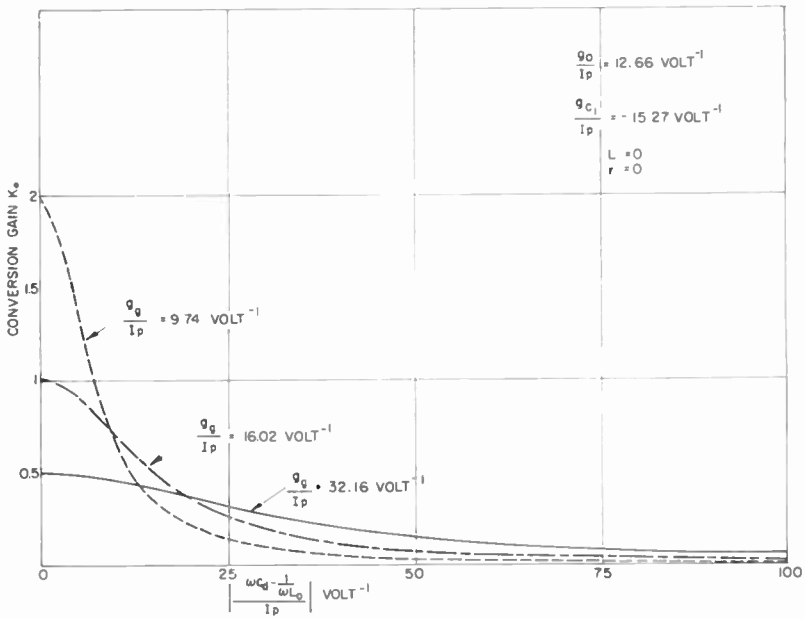

Fig. 9—Calculated conversion gain K_0 as a function of $|\omega C_d - (1/\omega L_0)|/I_p$ for the circuit of Figure 8 ($Y_L = \infty$, $Y_i = g_i = g_0 - g_{c1}^2/(g_0 + g_g)$).

Spurious Oscillations

A tunnel diode biased in its negative-resistance region, or driven into this region by an applied local oscillator voltage, can generate r-f oscillations. In autodyne frequency converters, advantage is taken of the self-oscillations of the tunnel diode to supply the local oscillator drive. In converters with external local oscillators, however, self-oscillation must be prevented, since these oscillations cause spurious responses and instabilities, and usually increase the noisiness of the converter.

Converter circuits that do not oscillate at any bias voltage when

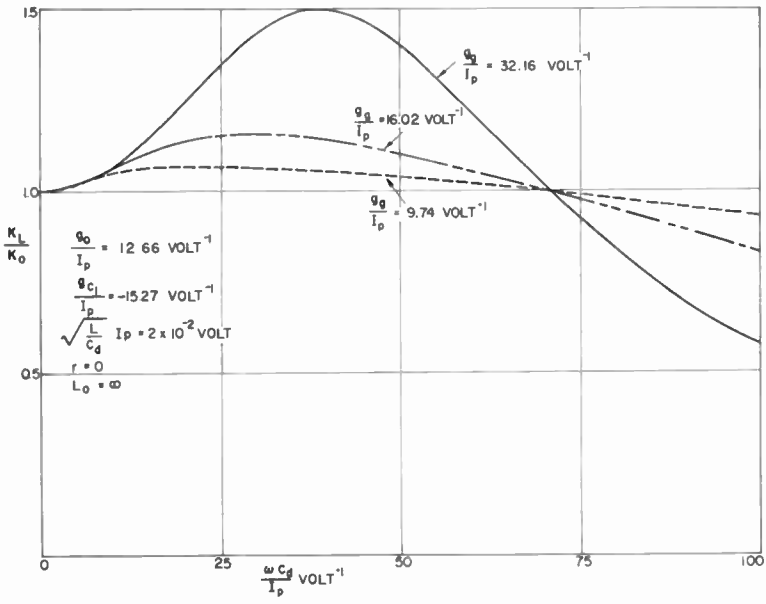

Fig. 10(a)—K_L/K_0 as a function of $\omega C_d/I_p$. K_L = calculated conversion gain, K_0 = conversion gain of Figure 9 ($Y_k = \infty$, $Y_t = g_t = g_0 - g_{c1}^2/(g_0 + g_g)$).

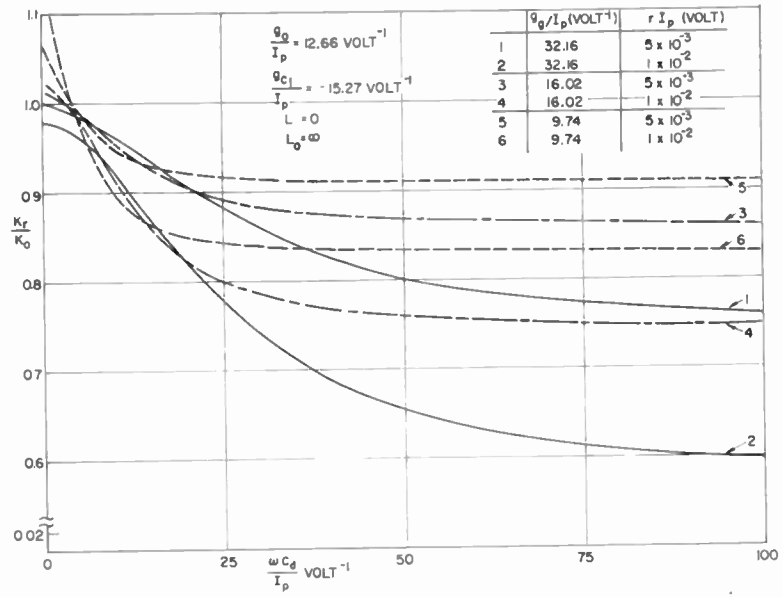

	g_g/I_p (VOLT^{-1})	$r I_p$ (VOLT)
1	32.16	5×10^{-3}
2	32.16	1×10^{-2}
3	16.02	5×10^{-3}
4	16.02	1×10^{-2}
5	9.74	5×10^{-3}
6	9.74	1×10^{-2}

Fig. 10(b)—K_r/K_0 as a function of $\omega C_d/I_p$. K_r = calculated conversion gain (K_0, Y_k, and Y_t as in Figure 10(a)).

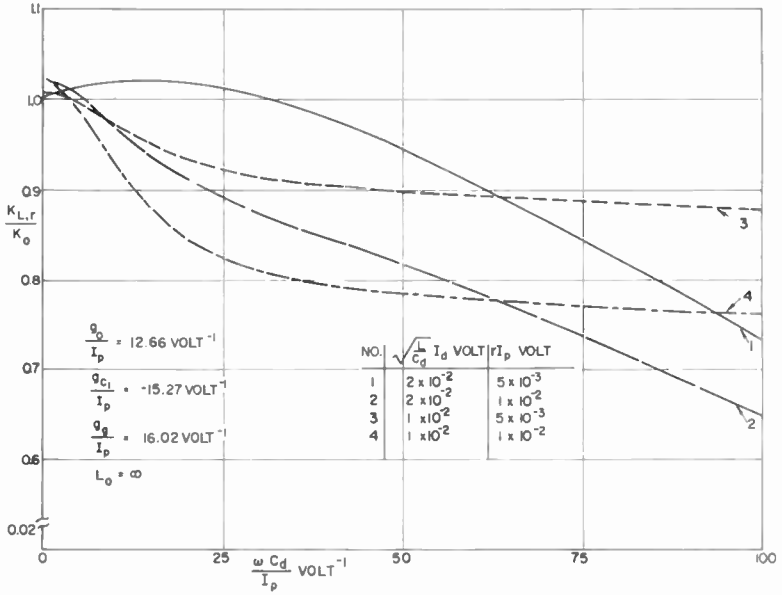

Fig. 10(c)—$K_{L,r}/K_0$ as a function of $\omega C_d/I_p$. $K_{L,r}$ = calculated conversion gain (K_0, Y_k, and Y_t as in Figure 10(a)).

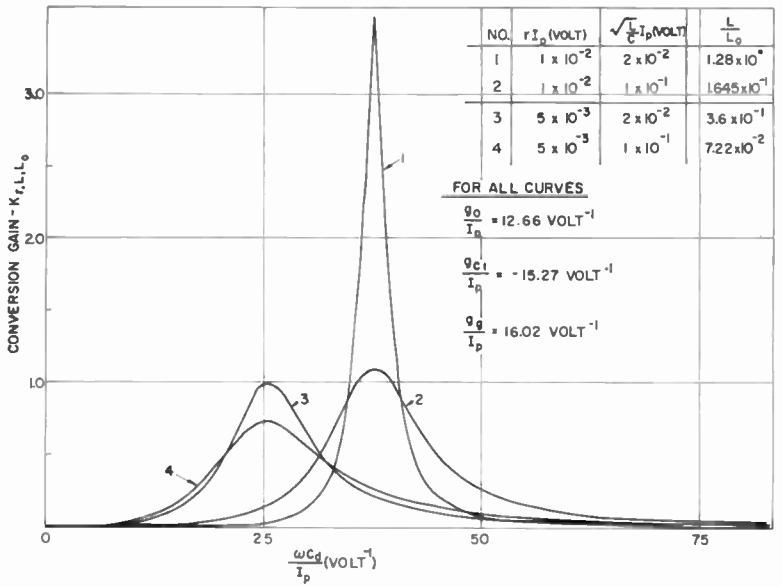

Fig. 11—Calculated conversion gain K_{L,r,L_0} as a function of $\omega C_d/I_p$. (Y_k and Y_t as in Figure 10(a)).

no local oscillator drive is applied are also stable at any bias when driven by the local oscillator. This type of converter circuit must use 'stable' diodes, i.e., diodes for which the following inequality holds:[10]

$$L_d < 3\,R_d^2 C_d. \tag{9}$$

For stable diodes, the limits on the maximum usable peak current, I_p, and the minimum time constant $R_d C_d$ are set by inequality (9), while these parameters for unstable diodes are limited only by semiconductor fabrication techniques. Consequently, unstable tunnel diodes are often useful in high-power or high-frequency converters.† It has been found experimentally that spurious oscillations in converters using unstable tunnel diodes can be prevented by applying a large ($V_0 > 0.1$ volt) local-oscillator drive. This procedure is most effective if the local-oscillator frequency is close to the self-oscillation frequency of the converter.

Shot Noise in Tunnel Diodes

The theory of noise in passive nonlinear-conductance frequency converters as developed by Strutt[11] also applies to tunnel-diode converters.[12-14] This theory requires a knowledge of the Fourier coefficients of the noise current in the nonlinear conductance.

At VHF and higher frequencies, the noise current in tunnel diodes is essentially pure shot noise.[15] However, the equivalent mean-squared shot-noise current I_{SN} is, for a large range of bias voltage, not proportional to the direct current through the diode; therefore, the coefficients used for Equation (1) cannot be used to approximate the equivalent shot-noise current.

---

[10] L. I. Smilen and D. C. Youla, "Stability Criteria for Tunnel Diodes," *Proc. I.R.E.*, Vol. 49, pp. 1206-1207, July, 1961.

† The power-handling capability of a diode is, in general, proportional to I_p. Also, the cutoff frequency, i.e., the frequency above which the real part of the diode impedance becomes positive, is proportional to $(|R_d|C_d)^{-1}$.

[11] M. J. O. Strutt, "Noise Figure Reduction in Mixer Stages," *Proc. I.R.E.*, Vol. 34, p. 942, December 1946.

[12] D. I. Breitzer, "Noise Figure of Tunnel Diode Mixer," *Proc. I.R.E.*, Vol. 48, p. 935, May 1960.

[13] D. G. Peterson, "Tunnel-Diode Down Converters," *Proc. I.R.E.*, Vol. 49, p. 1225, July 1961.

[14] C. S. Kim, "Tunnel-Diode Converter Analysis," *I.R.E. Trans.*, Vol. ED-8, p. 394, September 1961.

[15] J. J. Tieman, "Shot Noise in Tunnel Diode Amplifiers," *Proc. I.R.E.*, Vol. 48, p. 1418, August 1960.

I_{SN} can be computed from the actual diode current, I, by use of the following approximate equation:[12]

$$I_{SN} \approx |I| \frac{1 + \exp\left(-\frac{qV}{kT}\right)}{1 - \exp\left(-\frac{qV}{kT}\right)} \tag{10}$$

where q is the electronic charge, k is Boltzmann's constant, and T is the absolute temperature of the diode. Equation 10, using the meas-

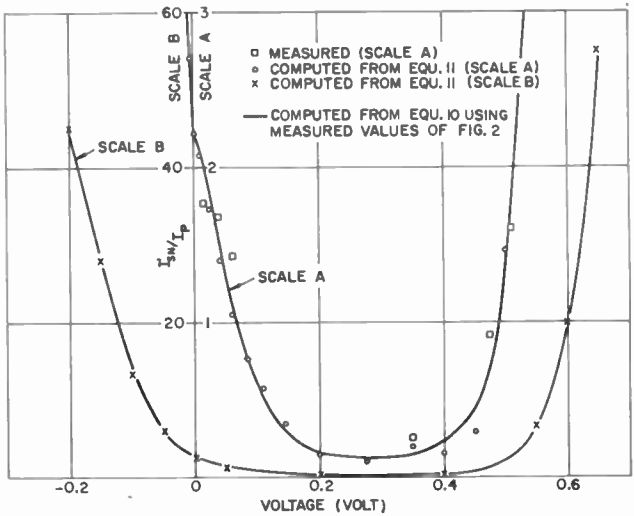

Fig. 12—Normalized mean-square shot-noise current as a function of voltage for a germanium tunnel diode. Values computed from Equation (10) and Figure 2 and from Equation (11) and measured values are shown.

ured values of I of Figure 2 and a temperature T of 300°K, is plotted in Figure 12, together with points computed from the following tenth-degree power series approximation:

$$I'_{SN} = \sum_{n=0}^{10} \beta_n V^n. \tag{11}$$

Good agreement is obtained in the range from —0.2 to 0.63 volt between values calculated from the power series and values calculated from Equation (10). Also shown in Figure 12 are several experi-

mental values of I'_{SN} measured at 30 megacycles. Agreement between measured and calculated values is good.

Equation (10) indicates that the equivalent shot-noise current always exceeds the actual diode current. However, if $qV/kT \gg 1$, $I_{SN} \approx |I|$. Thus, a comparison of Figures 2 and 12 shows that I'_{SN} is appreciably larger than $|I|$ in the neighborhood of the origin, but that the difference between the two currents decreases to about 5 per cent at a bias of ± 0.1 volt. If the diode is cooled below room temperature, the difference between I_{SN} and $|I|$ is reduced for all values of bias voltage and, in the limit as T approaches 0°K, I_{SN} approaches $|I|$ regardless of bias.

Equation (11) can be rewritten in terms of the d-c bias voltage, V_B, and the local-oscillator voltage, $V_0 \cos \omega_0 t$, as follows:

$$I'_{SN} = \sum_{n=0}^{10} \beta_n (V_B + V_o \cos \omega_o t)^n, \tag{12}$$

$$= I_0 + 2I_{c1} \cos \omega_0 t + 2I_{c2} \cos 2\,\omega_0 t + \cdots$$

The equivalent shot-noise conductance of the diode G_N is given by

$$G_N = \frac{q}{2kT} I_{SN}. \tag{13}$$

At room temperature ($T = 300$°K), this conductance is given by

$$G'_N = 20\, I'_{SN} \tag{14}$$

$$= G_0 + 2G_{c1} \cos \omega_0 t + 2G_{c2} \cos 2\,\omega_0 t + \cdots$$

Figure 13 shows curves for G_0, G_{c1}, and G_{c2} as functions of V_0 for several values of V_B as evaluated from Equations (12) and (14).

The Fourier coefficients of G'_N can be written as follows:

$$G_0 = \frac{1}{2\pi} \int_0^{2\pi} G'_N \, d(\omega_0 t),$$

$$G_{c\alpha} = \frac{1}{2\pi} \int_0^{2\pi} G'_N \cos \alpha\, \omega_0 t \, d(\omega_0 t). \tag{15}$$

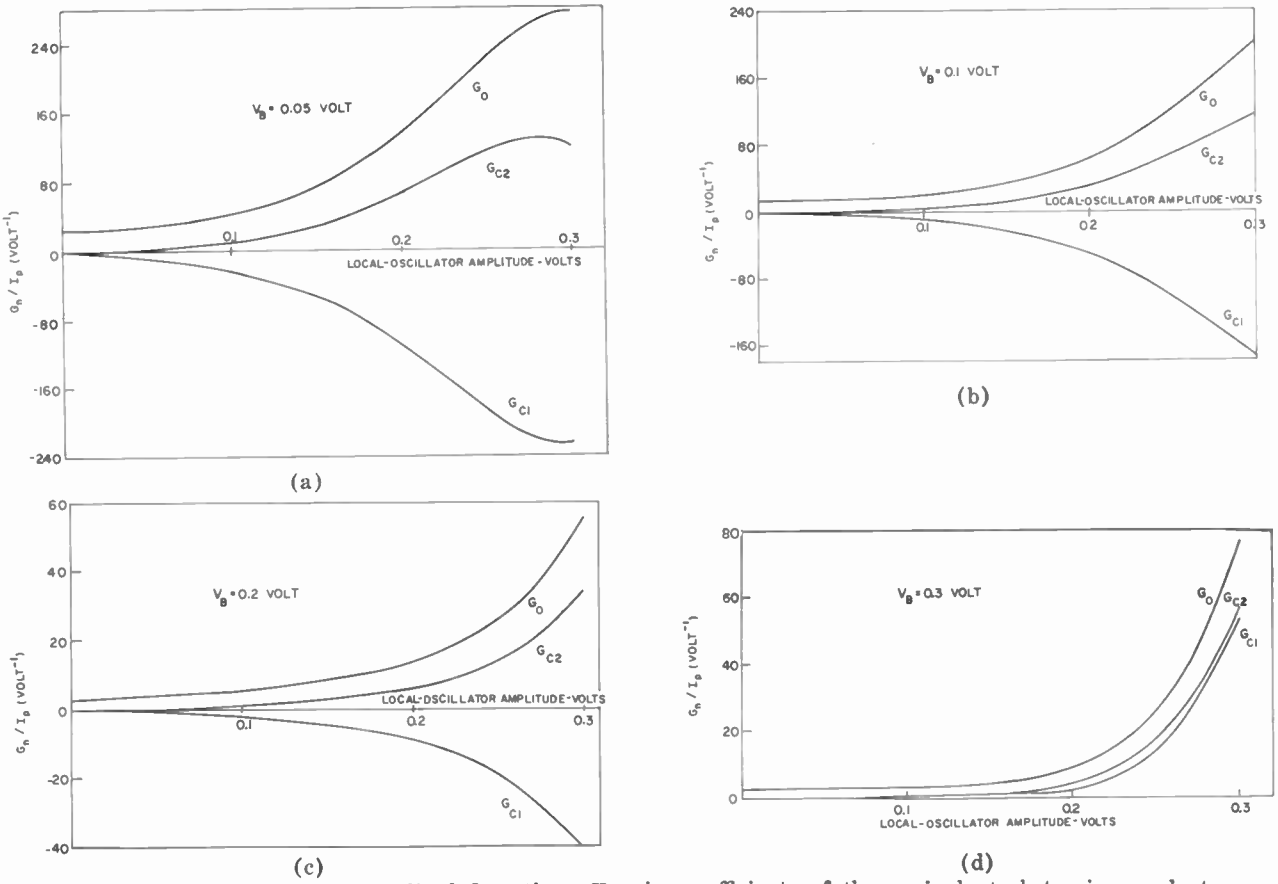

Fig. 13—Curves of the normalized first three Fourier coefficients of the equivalent shot-noise conductance of a germanium tunnel diode as functions of local-oscillator voltage for four values of d-c bias, V_B.

Because G'_N is always positive, it follows that

$$G_0 > 0, \qquad G_0 > G_{ca}. \tag{16}$$

A similar inequality applies, of course, to the Fourier coefficients of G_N at any temperature.

Noise Figure of Tunnel-Diode Frequency Converters

The noise figure, F, of a nonlinear-conductance converter with short-circuited image impedance ($Y_k = \infty$) and with real input admittance can be written as follows:*

$$F = 1 + \frac{T}{T_0}\left(\frac{G_0(g_0 + g_g)^2}{g_g\, g_{c1}{}^2} - \frac{2(g_0 + g_g)G_{c1}}{g_g\, g_{c1}} + \frac{G_0}{g_g}\right), \tag{17}$$

where T is the ambient temperature and T_0 is the standard reference temperature. In the derivation of Equation (17) it has been assumed that the noise currents at the signal and intermediate frequencies generated by the pumped nonlinear conductance are fully correlated. Also, in accordance with the IRE definition,[16] the noise figure is written in terms of available noise output power, and does not take into account any noise contributions from the i-f load.†

Because of inequality (16), the noise figure of a tunnel diode frequency converter, like the noise figure of a passive converter, must always exceed unity. However, the minimum noise figure that can be achieved with a tunnel diode converter is lower than the minimum noise figure of a passive converter, since the conductances g_o and g_{c1} in a tunnel diode converter are not restricted by inequality (4).

The calculated noise figure of a tunnel-diode converter ($g_g/I_p = 20$ volt^{-1}), minimized with respect to local-oscillator amplitude at every bias point, is shown as a function of bias voltage in Figure 14. Also shown are experimental values of noise figure measured on a UHF converter ($f_s = 512$ megacycles, $f_{Lo} = 482$ megacycles) with more than 10 decibels of image rejection. The graph shows fair qualitative agreement between measured and calculated values for bias voltages exceeding about 0.05 volt. For bias voltages below 0.05 volt, the qualitative agreement is poor; the calculated noise figure increases with

* For the case $Y_k \neq \infty$, see Equation (62) of Reference (14).

[16] I.R.E. Standards on Electron Tubes: Definitions of Terms, 1957, *Proc. I.R.E.*, Vol. 45, p. 1000, July 1957.

† Breitzer[12] has derived a noise-figure expression that does take the noise contribution from the load into account.

decreasing bias voltage, while the measured noise figure decreases.

The severe discrepancies between the measured and the calculated values of Figure 14 may be attributed to a number of causes, as follows:

1. The local oscillator used in the experiments had an appreciable internal resistance, and the local-oscillator voltage across the diode was therefore not a pure sinusoid. This effect is probably the most important cause of the observed discrepancy for bias voltages between

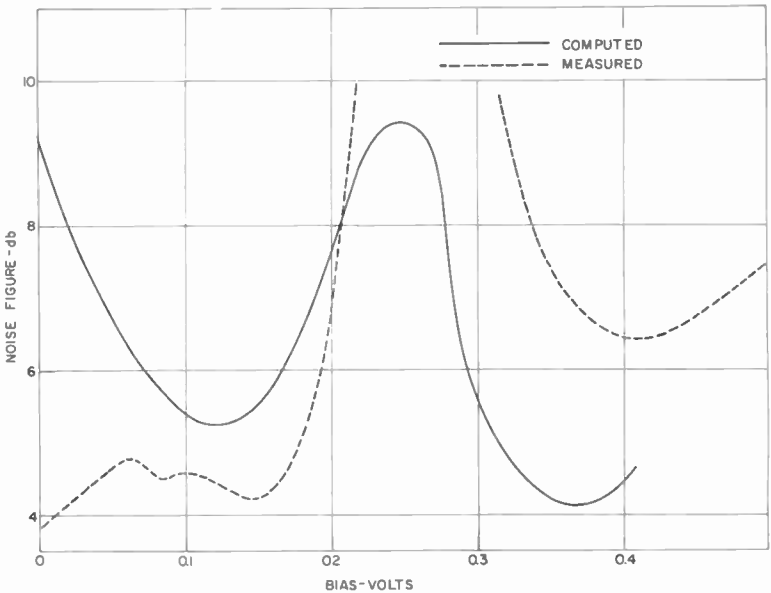

Fig. 14—Calculated and measured noise figure as a function of bias voltage for a tunnel-diode frequency converter ($g_g/I_g = 20$ volts^{-1}, $Y_L = \infty$). The noise figure is minimized with respect to local-oscillator voltage at every bias point. The measurements were taken with a UHF converter ($f_s = 512$ mc, $f_{LO} = 482$ mc).

0 and 0.05 volt. The impedance of the diode is very low for negative voltages, and considerable distortion of the negative cycles of the local-oscillator voltage occurs at small values of forward bias as shown, for example, by the wave shapes in Figure 5.

2. The noise figure depends to an important extent on the shape of the I–V characteristics of the diode.* The calculated values of noise

* For example, converters using special developmental RCA tunnel diodes have minimum noise figures for bias voltages of about 0.4 volt, while the optimum bias of the converter of Figure 14 is zero volts. The characteristics of the RCA diodes have steeper slopes in the 0.3 to 0.4 volt range than the diode of Figure 2.

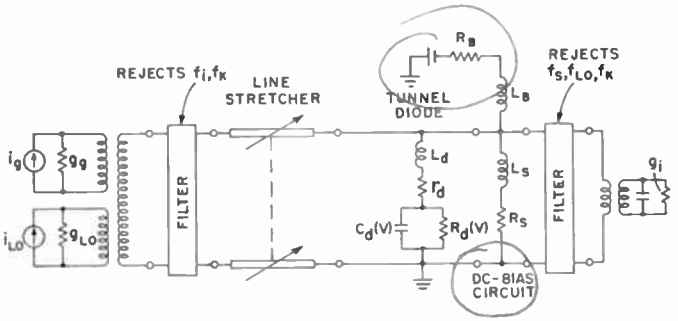

Fig. 15—Simplified equivalent circuit of tunnel-diode frequency converter with image rejection.

figure of Figure 14 are based on the I–V characteristics shown in Figure 2. However, the shape of the I–V characteristics of the diode used in the experiments differed somewhat from Figure 2, particularly for voltages in the valley region. This difference may be responsible for most of the observed discrepancy in the 0.2- to 0.4-volt region.

3. The effect of the parasitic elements of the diode, r_d, L_d, and C_d, which is probably significant at UHF frequencies, is not taken into account by Equation (17).

Experimental UHF and Microwave Tunnel-Diode Converters

Several low-noise UHF tunnel-diode frequency converters have been built and tested. Some of these converters were broadband (no image rejection), while others had built-in image-rejection filters. The intermediate frequency was 30 megacycles in all cases.

Figure 15 shows a simplified equivalent circuit for a converter with image rejection. Except for the d-c bias circuit, which is designed to prevent spurious oscillations while the diode swings through the negative-resistance region, the equivalent circuit is similar to conventional passive frequency converters. Figure 16 is a photograph of an actual

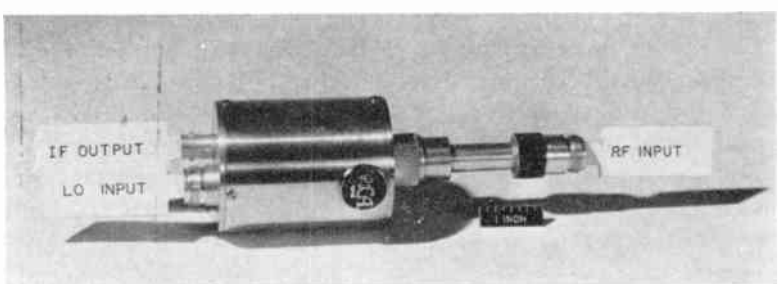

Fig. 16—Photograph of UHF tunnel-diode frequency converter.

converter. It can be seen that its size is comparable to that of miniaturized passive frequency converters.

The conversion gain of these converters could be adjusted to any convenient value by suitable choice of diode and circuit parameters, bias voltage, and local-oscillator drive. As expected, converters with conversion gain exceeding a few decibels were extremely sensitive to variations in input impedance (see Figure 6). On the other hand,

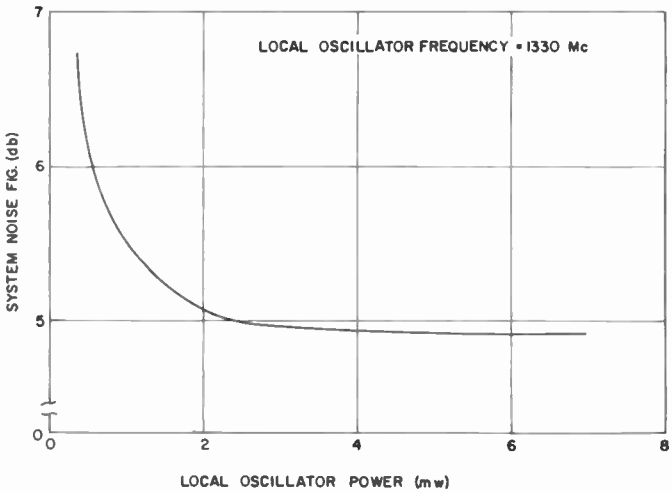

Fig. 17—System noise figure as a function of local oscillator power for a balanced converter (noise figure of i-f amplifier = 1.7 db).

converters with 0 decibels conversion gain, or with conversion loss, were in general stable with input VSWR's exceeding 10:1 varied through all phases. Furthermore, the lowest system noise figures (using an i-f amplifier with a 1.7-decibel noise figure) were obtained with converters having conversion losses in the neighborhood of zero decibels.

The system noise figure of a balanced L-band converter is plotted in Figure 17 as a function of local oscillator power. It is seen that the noise figure varies little for local oscillator power in the range from about 2-7 milliwatts. The use of this relatively high pump power results in a large dynamic range.* Figure 18 shows the conversion loss of a typical single-ended converter as a function of input power. The curve shows that the conversion loss is increased by 3 decibels at an

* Saturation effects occur only when the signal voltage across the diode becomes a significant fraction of the local-oscillator voltage.

input of about 0.1 milliwatt.† The sensitivity of this converter to inputs at unwanted frequencies was comparable to that of crystal-diode converters. For one-per-cent intermodulation distortion, the power in the unwanted signal was about —30 dbm.

Burnout, i.e., detectable deterioration of performance, occurred for CW powers of 2 watts, and for pulse energies of 170 ergs. These results show that tunnel diodes can handle roughly one order of magnitude more CW power and pulse energy than conventional point contact mixer diodes.

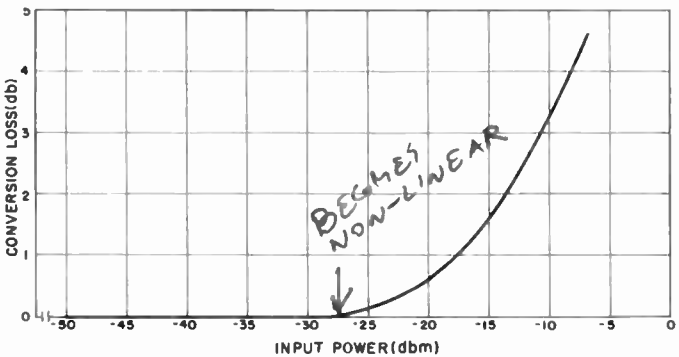

Fig. 18—Conversion loss as a function of input power for a UHF tunnel-diode frequency converter.

A broadband ($g_g = g_k$) converter operating with a local-oscillator frequency of 780 megacycles, had a double-sideband (radiometer) noise figure of 2.5 decibels and unity conversion gain.‡ It is of interest to note that both the minimum radiometer noise figure and the minimum conversion loss of a broadband positive-resistance frequency converter always exceed 3 decibels. Also, the tunnel diode used in the converter had a minimum I_0R_d value of about 1.2 (I_0 = direct current through diode, R_d = magnitude of negative resistance at bias point). The radiometer noise figure of a high-gain amplifier using this diode would exceed 3.5 decibels,[17] as compared to a noise figure of only 2.9

† In some more recent experiments with balanced mixers, 3-db gain compression occurred at a signal level of about 1 mw. The bandwidth of these converters was 250 megacycles centered at a frequency of 1270 megacycles.

‡ Passive circuit losses in front of the converter, amounting to 0.5 db, are not included in the quoted gain and noise figure. These losses were due to the local-oscillator input circuit and an i-f rejection filter, and can, in principle at least, be eliminated by more careful design.

[17] M. E. Hines and W. W. Andersen, "Noise Performance Theory of Esaki (Tunnel) Diode Amplifiers," *Proc. I.R.E.*, Vol. 48, p. 789, April 1960.

decibels for a high-gain system using the converter together with the best commercially available 30-megacycle i-f amplifier ($NF = 0.7$ decibel).

In converters with image rejection, the lowest measured single-sideband (radar) converter noise figure was 3 decibels. In this case the signal frequency was 512 megacycles, and rejection at the image frequency ($f_k = 452$ megacycles) was 11 decibels.

A tunnel-diode frequency converter was tested in the front end of a UHF television set and compared with a commercial UHF tuner using a point-contact diode converter. In this experiment, the tunnel-

Table I—Measured System Noise Figures Using a 30-Mc IF Amplifier With 1.7-db Noise Figure. (The quoted single-sideband noise figures include the losses of the image-rejection filters.)

Local Oscillator Frequency (mc)	Signal Frequency (mc)	Double-sideband System Noise Figure (db)	Single-sideband System Noise Figure (db) (image rejection ≧ 10 db)
482	512	——	5
780	——	3.9	——
1340	——	4.3	——
1340	1370	——	5.5
2000	——	5.5	——

diode converter was followed by an i-f amplifier with a 1.7-decibel noise figure, while the commercial tuner used a Nuvistor i-f amplifier with a 3-decibel noise figure. The over-all noise figure of the commercial tuner was 10 decibels. The tunnel-diode converter produced about 4.5 decibels improvement in sensitivity (see Figure 19 for a comparison of picture quality under very weak signal conditions), and appeared to be similar to the commercial tuner in all other operating characteristics, e.g., intermodulation distortion, linearity at high signal levels, and the like. Further experiments are planned in collaboration with the current Federal Communications Commission's UHF television tests.

It should be pointed out that the performance characteristics described here were obtained in the laboratory with experimental equipment. The use of tunnel-diode converters in a commercial product would probably necessitate certain compromises due to cost considerations, and the noise figures would be somewhat higher than those given here.

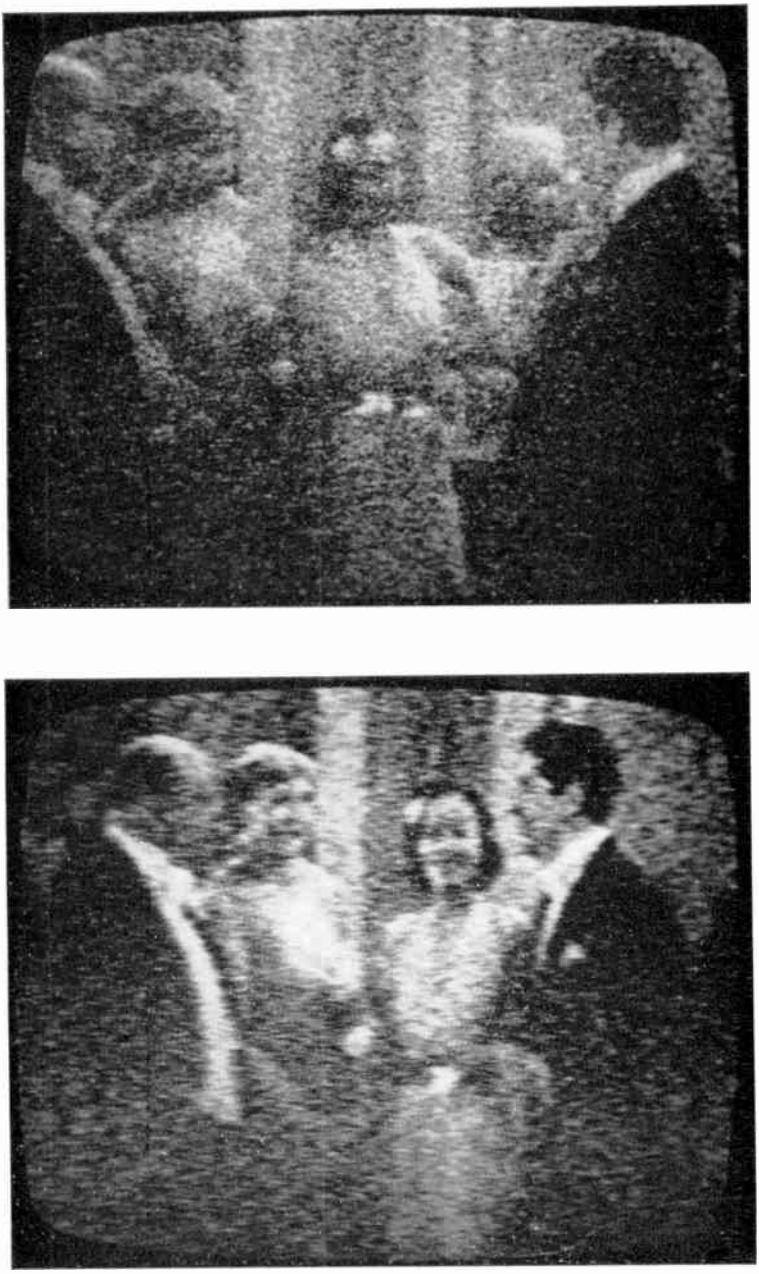

Fig. 19—Photographs of pictures displayed on UHF television picture tube: top picture received with point-contact diode frequency converter at input of receiver, and bottom picture received with tunnel-diode frequency converter at input of receiver.

Table I lists the lowest system noise figures measured to date. There is little doubt that significantly lower noise figures and higher operating frequencies than those listed in this table can be achieved in the near future. Possible methods for achieving these improvements include: (1) use of i-f amplifiers with noise figures of less than 1.7 decibels, (2) use of tunnel diodes with *I-V* characteristics specially tailored for low noise converter applications, (3) use of tunnel diodes with cutoff frequencies at X-band or higher, and (4) better use of nonsinusoidal pumping.

Conclusion

It has been demonstrated experimentally that stable UHF and microwave tunnel-diode frequency converters can have lower conversion loss, lower noise figures, larger dynamic range, and greater resistance to burn-out than crystal-diode converters.

The present converter theory covers only the case of sinusoidal local oscillator drive. In practice, however, the local oscillator is frequently strongly nonsinusoidal, and in this case quantitative agreement between theory and experiment is poor. In particular the measured noise figures are significantly lower than predicted by theory.

Acknowledgment

The authors extend their thanks to K. K. N. Chang, H. C. Johnson, J. L. Poirier, A. H. Solomon, and F. E. Vaccaro for their discussions and assistance.

SILICON JUNCTION NUCLEAR PARTICLE DETECTORS†*

By

R. L. Williams and P. P. Webb

RCA Victor Research Laboratories
Montreal, Canada

Summary—An encapsulated form of silicon junction nuclear particle detector is described, and resolution measurements are given for alpha and beta particles. Diode speeds of response, dead layers, and design considerations are discussed along with amplifier considerations. The future development of detector forms is briefly reviewed.

Introduction

THE feasibility of detecting ionizing nuclear particles by means of reverse-biased p-n junctions has been known for over 10 years.[1] However, the fabrication of useful devices has only occurred in the past 2 to 3 years, during which time the development of high-quality detectors has advanced very rapidly. Several devices were reported at the 7th Scintillation Conference, April 1960;[2] further and more-detailed results were presented at the IRE Conference on Solid State Counters, held at Gatlinburg in October 1960.[3]

Principle of Operation

The nuclear particle detector is depicted in Figure 1. The starting material is high-resistivity p-type single-crystal silicon, into which is diffused a shallow layer of an n-type impurity. When a reverse bias is applied to the p-n junction so formed, a wide depletion layer develops. An ionizing nuclear particle entering this depletion layer liberates

* Manuscript received 26 September 1961.

† The work has been supported in part by the Defence Research Board of Canada through the Electronic Component Research and Development Committee and by the Atomic Energy of Canada Ltd.

[1] K. G. McKay, "A. Germanium Counter," *Phys. Rev.*, Vol. 76, p. 1537, November 15 (Letters to the Editor), 1949.

[2] Proceedings of the Seventh Scintillation Counter Symposium, Washington, Feb. 1960, *Trans. I.R.E. PGNS*, Vol. NS-7, pp. 178-201, June-September 1960.

[3] Proceedings of the Gatlinburg Conference on Solid State Detectors, Oct. 1960, *Trans. I.R.E. PGNS*, Vol. NS-8, pp. 2-161, January 1961.

electrons and holes which are swept clear by the electric field in the depletion layer. The energy per electron–hole pair for all types of radiation appears to be very close to 3.5 electron volts. A 5.5-Mev alpha particle thus produces approximately 1.6×10^6 electron–hole pairs. Of those pairs liberated in the surface layer portion of the ionized track, many are lost by recombination, resulting in the counter having a window, or dead layer.

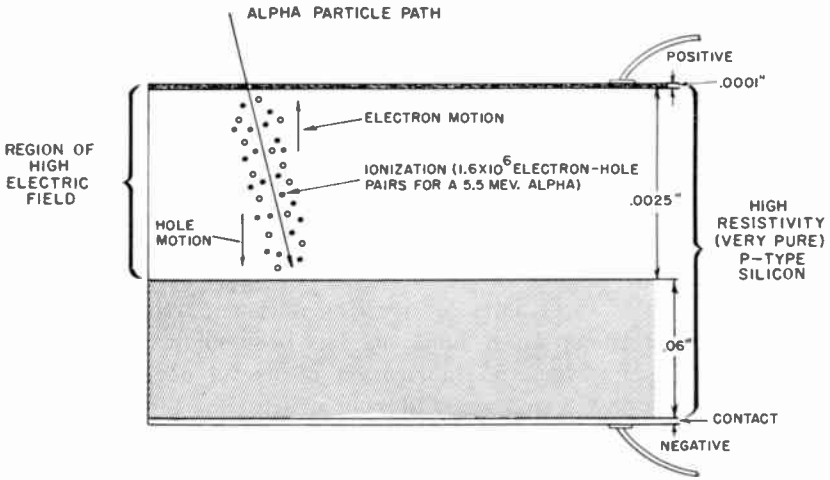

Fig. 1—Schematic diagram of diode operation.

Depletion-Layer Thickness—Linearly Detectable Energy

The most significant equation for the discussion of detector properties is the equation for the thickness of the diode depletion layer,

$$W = \left[k \frac{(V_d + V)}{2\pi q N_a} \right]^{1/2}. \qquad (1)$$

In this expression W is the width of the junction depletion layer, V the applied bias voltage, V_d the diffusion voltage (approximately 0.5 volt), k the dielectric constant, N_a the density of uncompensated impurities of the semiconductor, and q the electronic charge. Values of W (for silicon) as a function of V and N_a (or resistivity) can be found from the nomograph of Figure 2.

The depletion layer is the sensitive portion of the diode detector and, provided the range of a nuclear particle is shorter than the width

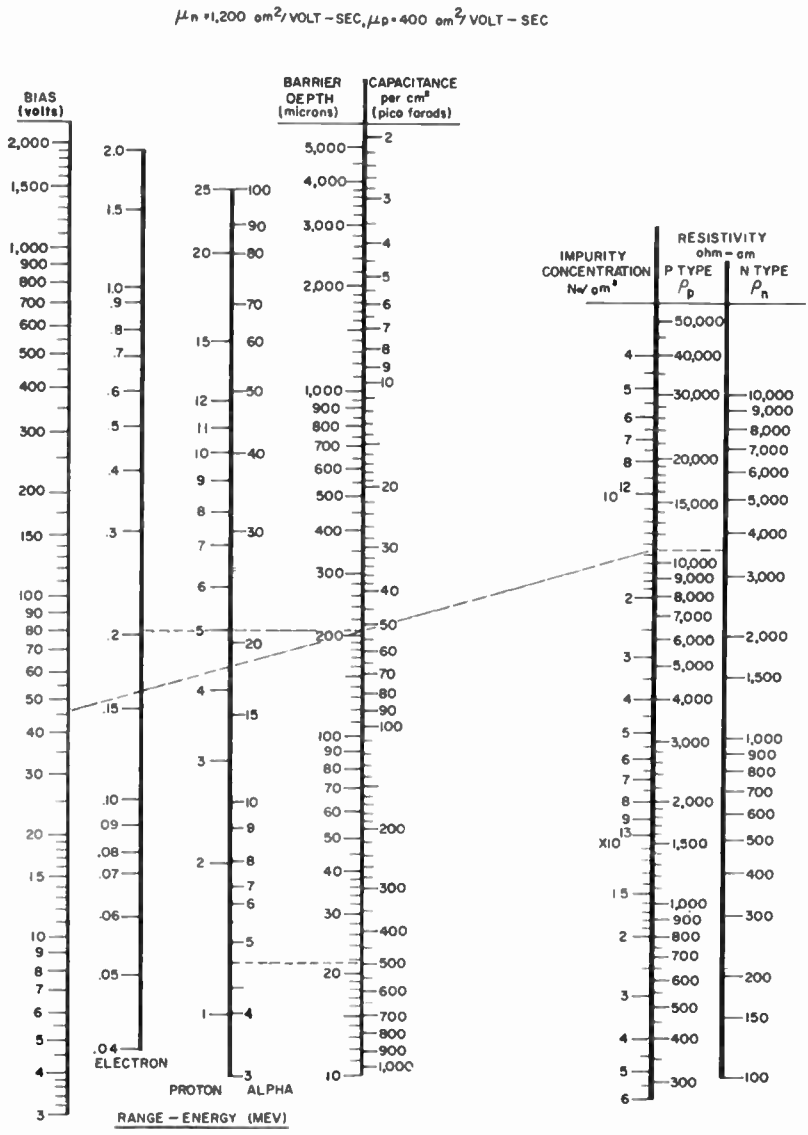

Fig. 2—Silicon diode nomograph. Depletion-layer thickness can be deduced from detector bias and silicon resistivity. The range of alpha particles, protons and electrons is given for silicon. (This is an extension of the nomograph of J. L. Blankenship and C. J. Borkowski, "Silicon Surface Barrier Nuclear Particle Detectors," *Trans. I.R.E. PGNS*, Vol. NS-7, p. 190, June-Sept., 1960.)

of the depletion layer, the particle is detected with 100 per cent efficiency and in a linear mode. The width of the depletion layer and hence the particles that can be detected in this manner can be deduced from a knowledge of the silicon resistivity and the applied bias voltage. However, as small resistivity changes normally occur during processing, a reliable value of W cannot always be obtained from the value of the starting resistivity. A more accurate W can be obtained by capacitance measurements, from which the limit of linearly detectable energy can be determined quite reliably.

Detector Configuration

Since junction surfaces are usually sensitive to air ambients, it has been found necessary to provide some junction protection. How-

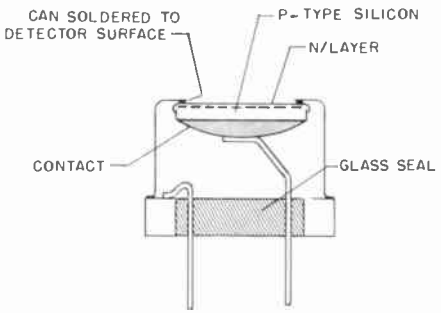

Fig. 3—Encapsulation details of a silicon-junction nuclear-particle detector.

ever, most of the nuclear particles of interest must pass directly into the front surface of the silicon, since most or all of the particle energy would be lost passing through a sealing layer or can. A consideration of these two points led to the detector form shown in Figure 3. The diffused surface of the pellet is bonded to the top side of a transistor can, the aperture of the can determining the sensitive area. Devices of this form have been made having sensitive areas of 5, 20, 50, 100, and 200 square millimeters.

Alpha-Particle Energy Resolution

The most spectacular feature of silicon-diode detectors is their performance when used for high-resolution spectroscopy. For 5 Mev alpha particles, the best room-temperature results for resolution

are 15 to 17 kev (f.w.h.m.) or 0.3 per cent (Brookhaven,[4] Oak Ridge,[5] and Atomic Energy of Canada, Limited[6]).

A resolution curve obtained from one of our best units is shown in Figure 4. The detector was made from 10^4 ohm-centimeter silicon with a 5-square-millimeter aperture in the encapsulating case. The detector, which was biased to 75 volts, has partially resolved the two alpha lines of americium 241 which are 43 kev apart; the resolution of the 5.48-Mev line is 20 kev.

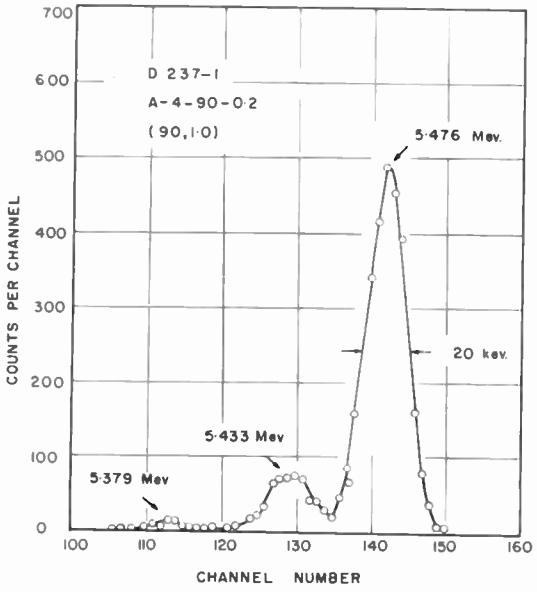

Fig. 4—Resolution measurement of Am-241 alpha particles. The designation A—4—90—0.2 indicates that the detector aperture is 5 square millimeters, the resistivity of the silicon is 10,000 ohm-cm, the detector is rated at 90 volts and the diffusion depth is 0.2 micron. The numbers in brackets indicate the bias used in the measurement and the amplifier time constants.

Figure 5 is the resolution curve obtained from a 2-square-centimeter active area unit made from 3000 ohm-centimeter silicon and biased to 200 volts. The resolution of 70 kev is slightly greater than one per cent.

---

[4] G. L. Miller, Private Communication.

[5] J. L. Blankenship and C. J. Borkowski, "Performance of Silicon Surface Barrier Detectors with Charge Sensitive Amplifiers," *Trans. I.R.E. PGNS*, Vol. NS-8, p. 17, January 1961.

[6] J. M. McKenzie and J. B. S. Waugh, "Silicon Junctions as Particle Spectrometers," *Trans. I.R.E. PGNS*, Vol. NS-7, p. 195, June-September 1960.

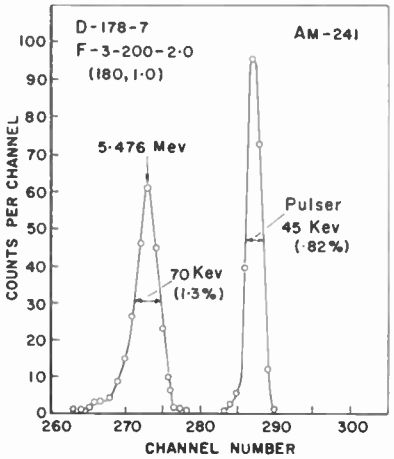

Fig. 5—Resolution measurement of Am-241 alpha particles using a 2-square centimeter area detector.

Resolution Versus Bias Characteristics

Figure 6 shows the average of the measured resolutions obtained for a number of detectors, plotted as a function of bias. All the units had a 2-micron-deep n-diffused layer on the front surface. In general the A and C size detectors can be grouped by the two resistivities of silicon used, 10^3 and 10^4 ohm-centimeter; while the F size units have

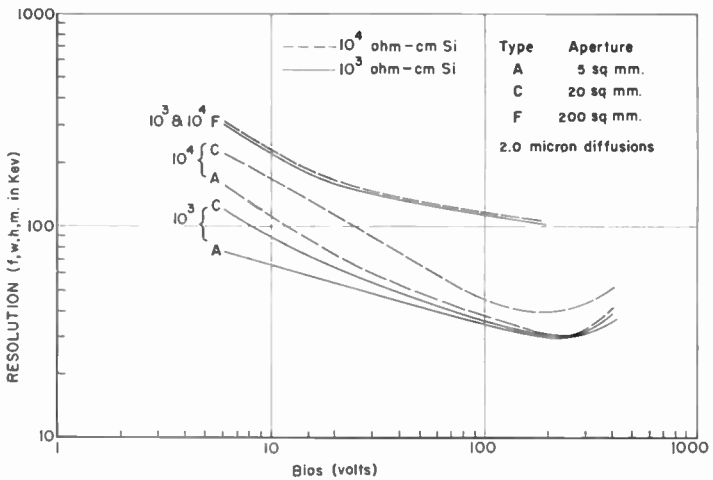

Fig. 6—Typical resolution-versus-bias curves for various 2-micron diffusion units. Curves terminating below 400 volts indicate the present maximum rating of the detector types.

only slightly different characteristics for the different material. The resolutions all improve as bias increases, most having their best values near 200 to 300 volts. At high biases, the values for the A and C units are nearly identical, since, in both cases, the capacitance of the two detector types is reduced to a value smaller than the system stray capacitance.

For the 2-square-centimeter units, their capacitances always dominate system capacitance. Thus resolutions should improve if the detector bias could be increased beyond the present 200-volt limit. (The termination of the curve on the diagram indicates this limit.)

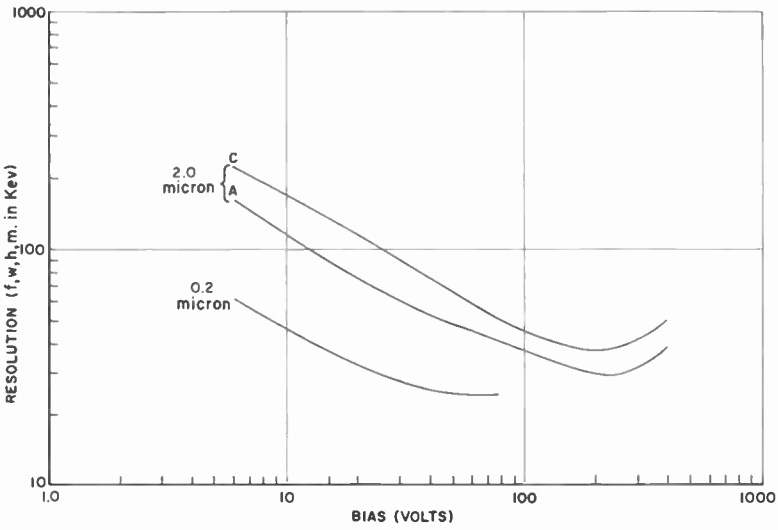

Fig. 7—The effect of the diffusion depth on resolution. The effect, shown for 10,000 ohm-cm diodes, is much smaller for 1000 ohm-cm units.

All the units shown on the graph have small losses in resolution as the bias reaches 400 volts. These losses are a manifestation of the increased leakage current, occurring at this bias, which increases the total system noise.

At 400 volts, a unit made from 10,000 ohm-centimeter silicon has a linear energy response for alpha particles up to 36 Mev.[7] The corresponding figure for protons is 9 Mev.

The graph of Figure 7 illustrates a feature of the small but still present dead layer of these detectors. For high-resolution alpha par-

[7] I. Naqib, University of Washington, Seattle. Private communication.

ticle work, the resolution realized depends on resistivity and diffusion depth chosen. For the 2-micron-diffusion-depth units, effects are present at low bias in high-resistivity diodes which result in poorer resolutions. However, since these effects disappear when the detectors have been biased from 30 to 50 volts, they are, in general, of little importance. On the other hand, to obtain the best resolution (e.g., Figure 4) for alpha particles it is necessary to use the smaller diffusion depth of 0.2 micron. The poorer resolution obtained with the thicker surface layer is associated with variations in the recombination of the freed carriers in the diffused layer. As can be seen, thin diffusion units have better characteristics at all biases, but particularly at low values.

Table I—Comparison of Values of Dead-Layer Depth Using Various Angles of Incidence of 5.5 Mev Alpha Particles and a Spectral-Response Method.

	Dead-Layer Depth (microns)	
	(10^3 ohm-cm Si)	(10^4 ohm-cm Si)
2.0 Micron Diffusion Depth		
Various angles of incidence	1.0	——
Optical	1.0	1.0
Variation with bias	None	None
0.2 Micron Diffusion Depth		
Optical	0.15	0.15

Dead Layer

Measurements of dead-layer thickness are tabulated in Table I. Two methods have been employed, one using different angles of incidence of alpha particles, and the other optical. In the first method the reduction in amplitude of the peak in the pulse-height spectrum as the alpha particle angle of incidence is reduced from 90° can be related to the dead-layer thickness. In the second method the silicon junction is used as a photodiode, and a dead layer is calculated from the shape of the spectral response.

The identical values of 1.0 micron appearing in the table do not signify highly accurate agreement but only indicate that a significant

difference cannot be detected between the two methods and the best value for dead layer is near 1.0 micron to an accuracy of 20 per cent. The dead layer is not significantly affected by bias.

For 0.2-micron-diffusion units the dead layer is 0.15 micron, very nearly the diffusion depth.

For a 5.5-Mev alpha particle, the rate of energy loss is 0.58 Mev/milligram/cm^2. Thus, the energy loss in a 1.0-micron path layer is 140 kev. An 18 per cent irregularity in the thickness of the layer would give a pulse spread of 25 kev. Such a variation in thickness would account for the fact that resolutions under 25 kev are rarely obtained with 2.0-micron units.

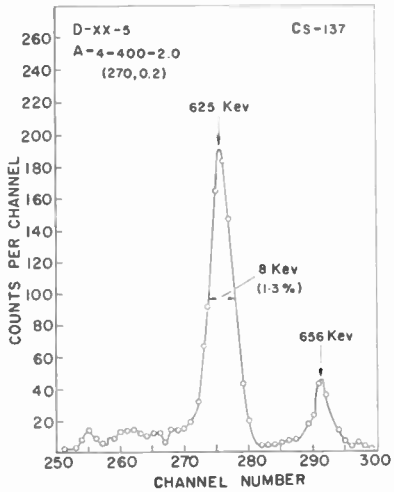

Fig. 8—Resolution measurement of Cs-137 beta particles. The resolution is limited only by amplifier noise.

Beta-Particle Measurements[8]

The dead layer is not as significant for lighter particles, as their energy loss in the layer is smaller. For electrons, the resolutions obtained are usually equal to those calculated from electrical noise considerations. Figure 8 indicates this point. The spectrum shows the *K* and *L* internal conversion lines of the 660 kev Cs-137 gamma ray. The unit was made from 10^4 ohm-centimeter silicon and is capable of 400-volt operation. The spectrum shown was taken at 250 volts bias

[8] For detailed discussion of beta particle detection see J. M. McKenzie and G. T. Ewan, "Semiconductor Electron Detectors," *Trans. I.R.E. PGNS*, Vol. NS-8, p. 50, January 1961.

and the peaks are resolved, showing spreads corresponding to about 8 kev of noise. This was essentially system noise. This is in contrast to alpha-particle resolution measurements, for which the resolution has usually been a factor of 2 poorer than predicted on the basis of system noise.

Figure 9 is the measurements of the spectrum of Co-57 taken with a thin-dead-layer 10^4 ohm-centimeters unit. The resolution is 12 kev, or about the value limited by electrical noise. The range of the 125-kev electron is sufficiently short that dead-layer effects can be observed if a 2.0-micron unit is used.

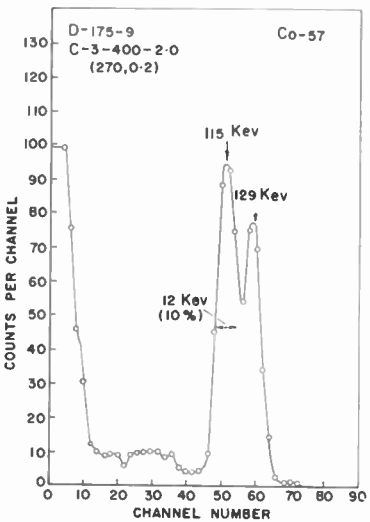

Fig. 9—Resolution measurement of Co-57 beta particles. The range of the beta particles is sufficiently short that dead-layer effects are beginning to limit the resolution attained.

Speed of Response

Predicted Values

The usefulness of a silicon junction detector for fast coincidence measurements is determined by the response time of the unit. It is of interest, then, to measure response times of diode detectors and to compare these to theoretical values. If resistance–capacitance effects are absent, response times are limited by the drift velocity, v, of the liberated electrons and holes in the field of the depletion layer.

The response times discussed are 10-90 per cent pulse rise times. This time can be calculated using the simple form

$$t = \int_{x_1}^{x_2} \frac{dx}{v}, \tag{2}$$

with x_1 and x_2 being the position of charge in the depletion layer corresponding to the pulse amplitude having risen 10 per cent and 90 per cent of its final value. To simplify the calculation, it will be assumed that the nuclear particle releases a small cluster of charge whose dimensions are small compared to the other depletion-layer dimensions.

Brown[9] has shown that the quantity ΔQ of the total charge Q is collected when the released charge has traversed the fraction $\Delta V/V$ of the voltage of the depletion layer. Thus for the 10 to 90 per cent response time, the quantities x_1 and x_2 correspond to the positions in the depletion layer where the voltage is 0.1 and 0.9 of the total voltage, V_b. For abrupt-junction diodes the voltage is parabolic, i.e.,

$$V(x) = V_b \left(\frac{x}{w}\right)^2. \tag{3}$$

The values of x_1 ($V = 0.1V_b$) and x_2 ($V = 0.9V_b$) occur for $x/W = .33$ and $x/W = .95$.

The drift velocity of holes, v_p, in an electric field E, having a mobility μ_p is $v_p = \mu_p E$. The electric field of the depletion layer is $dV(x)/dx = 2V_b x/W^2$. Using these expressions in Equation (2), the collection time of holes is

$$t_p = \frac{W^2}{2\mu_p V_b} \ln \frac{x_2}{x_1}. \tag{4}$$

Using Equation (1) relating W and V_b, a value of 400 for μ_p and the values of x_1 and x_2 given above, Equation (4) takes on the simple form

$$t_p = 1.07 \times 10^{-12}\rho, \tag{5}$$

where $\rho = 1/(q\mu_p N_a)$ = the resistivity of the silicon.

Normally, the response times of diodes are longer than this, suggesting that wafer and contact resistance along with diode capacitance determine the response time. To eliminate wafer resistance, a depleted-wafer structure has been fabricated. Referring to Figure 1, the diode

[9] W. L. Brown, *Trans. I.R.E. PGNS*, Vol. NS-8, p. 2, January 1961.

wafer is made sufficiently thin that the depletion layer extends completely through the wafer with 10 to 100 volts bias. With the wafer depleted there is no bulk resistance and, if contact resistance is kept low, sweep-out times should be observed. For voltages in excess of the depleting voltage, V_D, a uniform field component is added to the linear field so that

$$E(x) = \frac{2V_D}{W^2}x + \frac{V_D - V_b}{W}, \tag{6}$$

and

$$V(x) = \frac{V_D}{W^2}x^2 + \frac{V_D - V_b}{W}x. \tag{7}$$

For a depleted wafer the x_1/W and x_2/W values are no longer .33 and .95 as calculated from Equation (3). For large biases ($V \gg V_D$) the field becomes nearly uniform and x_1/W and x_2/W become approximately equal to 0.1 and 0.9, respectively. For intermediate biases, Equation (7) must be solved to determine x_1 and x_2 for each value of applied voltage.

At high electric fields ($10^4 - 10^5$ volts per centimeter) the velocities of electrons and holes saturate. Using the form $v_p = \mu_p E\,(1 + E/E_0)^{-1}$, Equation (2) can be resolved giving

$$t_p = \frac{(x_2 - x_1)W}{\mu_p E_0} + \frac{W^2}{2\mu_p V_D} \ln \left[\frac{1 + \dfrac{W(V_b - V_D)}{2x_2 V_D}}{\dfrac{x_1}{x_2} + \dfrac{W(V_b - V_D)}{2x_2 V_D}} \right]. \tag{8}$$

For very high biases, $V \gg V_D$, the limiting collecting time is the first term. This is governed by the saturation velocity of holes in silicon $\mu_p E_0$, which, using Prior's[10] data, is of the order of 2×10^7 centimeter per second.

Experimental Results

Response-time data taken on two wafers, 6×10^{-2} and 2×10^{-2} centimeter thick of 50,000 ohm-centimeter silicon are shown in Figure 10. At low biases, the response time is bias dependent, and the values

[10] A. C. Prior, "The Field-Dependence of Carrier Mobility in Silicon and Germanium," *Jour. Phys. Chem. Solids*, Vol. 12, p. 175, Pergamon Press, London 1959/60.

vary with the same power of the bias voltage as do the capacitances of the diodes. The capacitance data for the diodes are given on the graph. The diode wafers are depleted when the capacitance becomes independent of voltage. Combining the values of V_D with the depleted wafer capacitances, and wafer areas of 1/4 square centimeter, resistivity values of about 50,000 ohm-centimeters are calculated.

Using the equivalent circuit discussed by Ramo and Mayer,[11] the

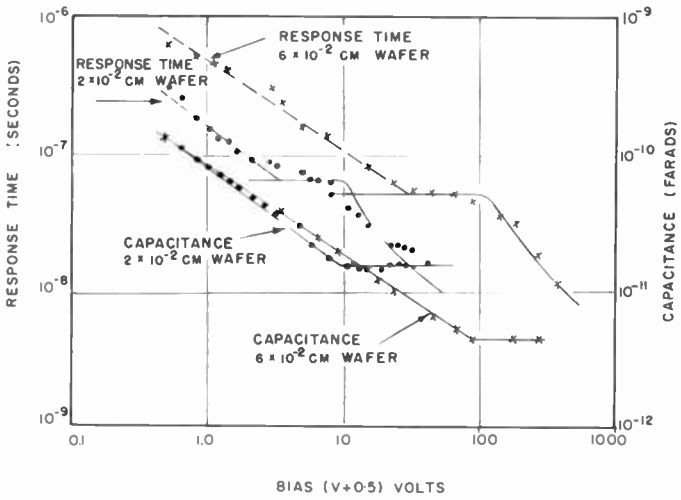

Fig. 10—Response times and capacitances of depleted-wafer diodes. The low-bias response times have the same bias dependence as does the diode capacitance. The response-time plateau is a charge collection time and the reduction of response times at the highest bias results from the change of field form when the wafer depletes.

response time should be dependent on the diode capacitance, C_d, the circuit stray capacitance, C_s, and the combined resistance, R_d, arising from the undepleted portion of the diode pellet and contacts. However, the response-time expression

$$t = R_d \frac{C_s C_d}{C_s + C_d} \tag{9}$$

does not agree in form with the observed data. Stray capacitance has been measured to be 10 picofarads, and at low biases C_d is of the order

[11] C. T. Raymo and J. W. Mayer, "Transient Response of P-N Junction Detectors," *Trans. I.R.E. PGNS*, Vol. NS-8, p. 157, January 1961; H. M. Mann, J. W. Haslett, and G. P. Lietz, "Pulse Rise Time for Charged Particles in p-n Junctions," ibid, p. 151.

of 100 picofarads. Equation (9) predicts that at these low biases response times should be essentially independent of C_d.

For bias values between $V_D/2$ and V_D, the response times of the units do not vary appreciably and have values close to those calculated. The two solid-line response-time curves were obtained using Equation (8) and the following data: for the 6×10^{-2}-centimeter wafer, $V_D = 115$ volts and resistivity = 50,000 ohm-centimeter; for the thinner unit, $V_D = 10$ volts and resistivity = 60,000 ohm-centimeter. Although there is some disagreement between theory and experiment near V_D, the general agreement is sufficiently good that Equation (8) can be used with confidence to calculate sweep-out response times.

To obtain high speeds of response it would appear that it is only necessary to use thin wafers, so that V_D is small, and to apply a bias many times V_D. Accordingly, diodes were fabricated on wafers as thin as 2 to 3 $\times$ 10^{-2} centimeter, but little success has been realized in obtaining high enough bias ratings to accomplish sweep-out times less than 10 nanoseconds.

The fastest response times observed to date were obtained with a 100 ohm-centimeter silicon diode; even at low biases, a 6-nanosecond system rise time was obtained. Unfortunately, the high capacitance, and resulting small signals, limits the usefulness of such units.

Charge Amplifiers

To obtain optimum results from nuclear particle detectors of this type, the design of suitable amplifiers must be given careful consideration. The principal defect of diode detectors is that their leakage or saturation currents are strong functions of temperature. As the units are used with a load resistance of 10 megohms or greater, small leakage-current changes alter the bias. Since the unit's capacitance varies inversely as the square root of bias, and since the signal is proportional to the reciprocal of detector capacitance, temperature variations result in signal drift. The circuit shown in Figure 11 does much to eliminate such variations.

For a charge amplifier, as this configuration is called, the output signal has been found to be given by the expression

$$V_{out} = \frac{Q}{C_d} G \frac{C_d}{C_d + (1+G)C_f} = \frac{Q}{C_f} \frac{1}{1 + \frac{1}{G} + \frac{C_d}{C_f G}}.$$

In this expression C_d is the detector capacitance, C_f the feedback capacitance, G the open-loop gain of the amplifier, and Q the charge liberated by the nuclear particle in the depletion layer of the detector diode. If the open-loop gain and the feedback are sufficiently large, then the output is given by the approximate form

$$V_{out} \approx \frac{Q}{C_f}\left[1 - \frac{C_d}{C_f G}\right].$$

For $G = 1000$, $C_f = 5$ picofarads and $C_d = 50$ picofarads, the factor

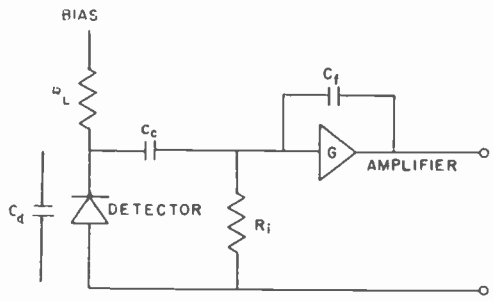

Fig. 11—Charge amplifier configuration for maximum stability.

$C_d/C_f G$ has a value of 100. Thus a stability of 10 per cent or better in C_d results in a stability of 0.1 per cent in the detecting system. The measurements described previously were made using such an amplifier. It has 7 kev of noise when operated with the detector removed.

Detailed discussion of such circuits can be found in References (5), (12), and (13).

Typical Design Considerations

In the case of beta-particle detection, signal-to-noise ratios become all important in determining feasibility of detection. Figure 12 includes much of the data necessary for considering such a problem. One of the curves is the noise width obtained for a type 7586 nuvistor charge amplifier as a function of input capacitance.

---

[12] E. Fairstein, "Considerations in the Design of Pulse Amplifiers for Use with Solid State Radiation Detectors," *Trans. I.R.E. PGNS*, Vol. NS-8, p. 129, January 1961.

[13] R. L. Chase, W. A. Higinbotham, and G. L. Miller, "Amplifiers for Use with P-N Junction Radiation Detectors," *Trans. I.R.E. PGNS*, Vol. NS-8, p. 147, January 1961.

For these measurements a pulser was used in place of a source, and various capacitances were added to the detector mount. The second curve is the shot-noise equation plotted in terms of noise width. The diode shot-noise contribution does not depend on detector capacitance.

Consider as an example the detection of Co-57 beta particles, with the design problem being to construct the largest-area detector that

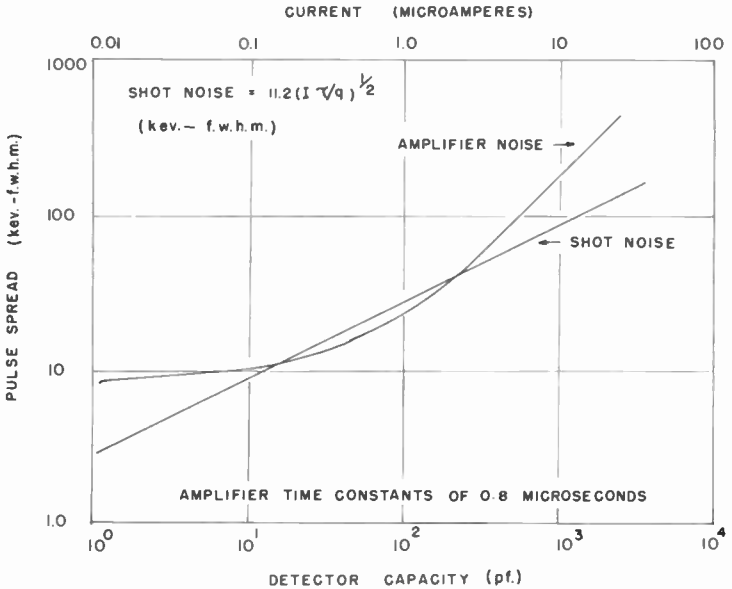

Fig. 12—Noise contribution from diode currents and amplifiers. The amplifier data is for a type 7586 nuvistor charge amplifier.

can provide a signal-to-noise ratio (full width at half maximum) of 4 to 1. A bias supply of 25 volts is available. From Figure 8, the energy of Co-57 betas is about 130 kev. Referring to the nomograph, Figure 2, 90 microns of depletion layer are required. Again using the nomograph, silicon of 4000 ohm-centimeter or greater will ensure complete detection.

For the signal-to-noise ratio required, noise cannot be greater than 33 kev; thus, using Figure 12, the capacitance must be less than 150 picofarads. For 10,000 ohm-centimeter silicon and 25 volts, a junction area of 2 square centimeters can be used.

The area must be sufficiently small that leakage current does not contribute significantly to the total noise. For a leakage current I and a bandwidth Δf, the mean square noise current is given by

$$\overline{i^2} = 2qI\Delta f.$$

This expression has been found applicable to diodes when the leakage current is not rising faster than $V^{1/2}$. The shot-noise contribution to pulse spread has been plotted in Figure 12. In order that the diode shot noise be less than 10 per cent of the noise spread due to amplifiers, the leakage current must be less than 1/4 microampere. Because of fabrication difficulties, it may be necessary to reduce the area so as to meet this requirement.

Future Prospects

With the 400-volt 10,000 ohm-centimeter units, protons can be detected linearly with energies up to 9 Mev. To increase this energy range, wider depletion layers are required. One approach is to attempt to design diodes which will stand off thousands of volts, but this, in addition to being technically difficult, has the disadvantage of requiring very-high-voltage bias supplies. An alternative method is far more attractive.

Pell[14] has demonstrated that ionized lithium impurity atoms can be drifted by the electric field of a reverse-biased junction. Such a drifting process proceeds in such a way that it compensates the existing crystal impurities. Elliott[15] has reported diodes made this way with 3.38 millimeters of depletion layer, operating with only 80 volts bias.

The difficulty encountered with this type of structure is that it slowly diffuses back to its original or predrifted condition. Storing units with a bias may prevent their degradation with time. A more serious difficulty may occur as a consequence of recombination in the high density of freed charge produced by an ionizing particle. The best detecting capabilities are expected for the highest quality, i.e., highest purity crystals. Although lithium-compensated material appears very pure on the basis of electrical measurements, it contains the added lithium as well as the original impurities, and therefore may have a short carrier lifetime.

The use of conductivity modulation of a large block of semiconductor material of very high resistivity (10^{12} to 10^{15} ohm-centimeter) appears still far in the future. Recently Harding *et alii*[16] used the conductivity modulation of a block of gallium arsenide to detect gamma

[14] E. M. Pell, "Ion Drift in an n-p Junction," *Jour. Appl. Phys.*, Vol. 31, p. 291, February 1960.

[15] J. H. Elliott, "Thick Junction Radiation Detectors Made by Ion Drift," *Nuclear Inst. and Methods*, Vol. 12, p. 60, June 1961.

rays, but the resolution does not appear to be comparable to that of good silicon diodes. Conductivity modulation of gold-doped silicon at 77°K has been used for detection of nuclear particles,[17] but because of the cooling requirement, this method has received very little attention.

In view of the success of the lithium drifting technique and the lack of evidence for an immediately available conductivity counter, the former will probably be actively pursued for long-range particles.

ACKNOWLEDGMENT

Most of the resolution measurements were performed at the Laboratories of the Atomic Energy of Canada Limited, Chalk River. The authors are indebted to A.E.C.L. and in particular to Mr. I. L. Fowler for providing the facilities.

[16] W. R. Harding, C. Hilsum, M. E. Moncaster, D. C. Northrop, and O. Simpson, "Gallium Arsenide for Gamma-Ray Spectroscopy," *Nature*, Vol. 187, p. 405, July 30, 1960.

[17] J. D. van Putten and J. C. Vander Velde, "Homogeneous Solid State Ionization Detector," *Trans. I.R.E. PGNS*, Vol. NS-8, p. 124, January 1961.

DERIVATION OF IDEAL ELECTRODE SHAPES FOR ELECTROSTATIC BEAM FOCUSING*

BY

W. W. SIEKANOWICZ

RCA Electron Tube Division,
Princeton, N. J.

Summary—This paper presents a derivation of ideal electrode shapes for electrostatic focusing of parallel, laminar, ribbon, hollow, and cylindrical electron beams. The shapes of the electrodes are derived by a method similar to that employed for designing Pierce-type electron guns. This method is based on the solution of the Laplace equation outside the boundary of the electron beam and satisfaction of certain conditions at that boundary. An approximate expression for the voltage distribution at the beam boundary, differing from the exact distribution by less than 3 per cent, provides simple solutions for the voltages outside the regions of electron flow. Equipotential plots that can be used for the design of the focusing electrodes are given for ribbon, hollow, and cylindrical beams for several voltage ratios.

INTRODUCTION

THE IDEAL MODEL for an electrostatically focused laminar electron beam having constant cross-sectional current density and no variations in the transverse dimensions has been described previously.[1] The model discussed in this paper differs from previous analyses[2-6] because it applies to beams having simultaneously large current densities and large voltage variations in the regions of electron flow.

* Manuscript received 20 December 1961.

[1] W. W. Siekanowicz and F. E. Vaccaro, "Periodic Electrostatic Focusing of Laminar Parallel-Flow Electron Beams," *Proc. I.R.E.*, Vol. 47, p. 451, March, 1959.

[2] A. M. Clogston and H. Heffner, "Focusing of an Electron Beam by Periodic Fields," *Jour. Appl. Phys.*, Vol. 25, p. 436, April, 1954.

[3] P. K. Tien, "Focusing of a Long Cylindrical Electron Stream by Means of Periodic Electrostatic Fields," *Jour. Appl. Phys.*, Vol. 25, p. 1281, October, 1954.

[4] K. K. N. Chang, "Confined Electron Flow in Periodic Electrostatic Fields of Very Short Periods," *Proc. I.R.E.*, Vol. 45, p. 66, January, 1957.

[5] K. K. N. Chang, "Biperiodic Electrostatic Focusing for High-Density Electron Beams," *Proc. I.R.E.*, Vol. 45, p. 1522, November, 1957.

[6] J. R. Pierce, *Theory and Design of Electron Beams*, p. 194, D. Van Nostrand Co., Inc., New York, N. Y., 1954.

The ideal model,[1] which is applicable to axially symmetric electron beams, is derived as follows. Figure 1 shows a series of equally spaced parallel grids having infinite dimensions perpendicular to the x coordinate. Alternate electrodes are connected together in a manner such that one set of grids is maintained at a low d-c voltage, V_L, and the other at a high d-c voltage, V_H. In the absence of space charge, the potential distribution between the grids is linear, as shown by curve A in Figure 1. When a beam having infinite transverse dimensions, uniform current density, and electron trajectory parallel to the x axis is injected at plane OL, the resultant space charge depresses the poten-

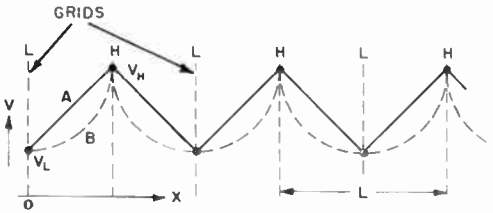

Fig. 1—Schematic diagram of the grid arrangement and voltage distributions used for derivation of the ideal model for the electrostatically focused electron beam.

tial between the grids. As the amount of injected current is increased, a condition is reached at which the potential variation shown by curve B exists. This curve has the property

$$\left.\frac{\partial V(x)}{\partial x}\right|_{x=0} = 0. \tag{1}$$

Under this condition, the potential variation in any region LH can be derived from the following equation:[7]

$$\frac{x}{x_0} = \left(\left[\frac{V(x)}{V_L}\right]^{1/2} + 2\right)\left(\left[\frac{V(x)}{V_L}\right]^{1/2} - 1\right)^{1/2}, \tag{2}$$

where

$$x_0 = \frac{aV_L^{3/4}}{J^{1/2}}. \tag{3}$$

[7] K. R. Spangenberg, *Vacuum Tubes*, p. 256, Eq. (10.39), McGraw-Hill Book Co., Inc., New York, N. Y., 1948.

In the preceding expression, J is the current density in amperes per square meter and a^2 is 2.335×10^{-6} amperes per volt$^{3/2}$.

Figure 2 shows a plot of the normalized voltage $V(x)/V_L$ calculated from Equation (2) as a function of the normalized distance x/x_0. This plot is a more accurate representation of the dashed curve in the LH intervals shown in Figure 1. The dashed potential distribution in the HL regions is a mirror image of the curve in the LH intervals. Because the quantities do not vary in the transverse dimensions, the

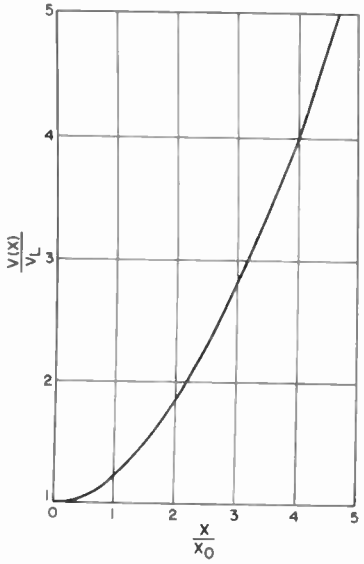

Fig. 2—Plot of the ideal normalized beam voltage $V(x)/V_L$ as a function of the normalized distance x/x_0.

variation of d-c potential in the transverse direction r is zero. Therefore,

$$\frac{\partial V}{\partial r} = 0. \tag{4}$$

The voltage variation shown by curve B in Figure 1 and a zero transverse voltage gradient are the conditions at the beam boundary that permit electrostatic focusing of maximum constant cross-sectional current density in a laminar parallel electron beam by two focusing electrodes per half-period LH or HL. This current density, in amperes per square meter, is given by the following expression based on Figure 1 and Equation (2):

$$J = \frac{9.340}{L^2}\left[1 + 2\left(\frac{V_L}{V_H}\right)^{1/2}\right]^2\left[1 - \left(\frac{V_L}{V_H}\right)^{1/2}\right] V_H^{3/2} \times 10^{-6}, \tag{5}$$

where L, expressed in meters, is the period of the focusing structure. The variation of the current density J with the voltage ratio V_L/V_H has been described previously.* This density reaches the maximum value J_m, in amperes per square meter, when the voltage ratio V_L/V_H in the region of electron flow is 0.25. Therefore,

$$J_m = \frac{18.68\, V_H^{3/2} \times 10^{-6}}{L^2}. \tag{6}$$

The current I, in amperes, within an ideal electrostatically focused cylindrical electron beam having a diameter of d meters is given by

$$I = 7.336\left[1 + 2\left(\frac{V_L}{V_H}\right)^{1/2}\right]^2\left[1 - \left(\frac{V_L}{V_H}\right)^{1/2}\right] V_H^{3/2}\left(\frac{d}{L}\right)^2 \times 10^{-6}. \tag{7}$$

Similarly, the current within a ribbon beam having thickness t and width w, in meters, is given by

$$I = 9.340\left[1 + 2\left(\frac{V_L}{V_H}\right)^{1/2}\right]^2\left[1 - \left(\frac{V_L}{V_H}\right)^{1/2}\right] V_H^{3/2}\frac{wt}{L^2} \times 10^{-6}. \tag{8}$$

The current carried by a hollow electron beam having a mean diameter D considerably greater than the thickness t can be obtained by substituting πD for w in Equation (8):

$$I = 29.34\left[1 + 2\left(\frac{V_L}{V_H}\right)^{1/2}\right]^2\left[1 - \left(\frac{V_L}{V_H}\right)^{1/2}\right] V_H^{3/2}\frac{Dt}{L^2} \times 10^{-6}. \tag{9}$$

The values given by Equations (5) through (9) can be used as figures of merit in evaluating the practical performances of electrostatically focused cylindrical, ribbon, and hollow electron beams.

---

* See Reference 1. This variation has the same form shown in Figure 3.

The procedure used in designing a cylindrical, ribbon, or hollow electron beam having finite transverse dimensions and satisfying the boundary conditions of Equations (1) and (2) is similar to that used for designing Pierce-type electron guns.[8] In this procedure, it is necessary to determine the shapes of the focusing electrodes that establish the same conditions at the boundary between the electron beam having the current density given by Equation (5) and the space-charge-free region as those which exist when the beam is extended to infinity in the transverse direction.

The shapes of the focusing electrodes can be computed from theory or obtained from electrolytic tank measurements. The present paper concerns the theoretical determination of these shapes.

Theoretically the shape of the focusing electrodes may be determined by solving the Laplace equation[9] in the space-charge-free region, subject to the previously mentioned boundary conditions. Figure 1 shows that, for the problem considered, the solution to Laplace's equation must be symmetrical with respect to planes L and H. Approximate shapes for the focusing electrodes were derived by Hechtel[10] from a solution of the Laplace equation that approximately satisfied the voltage distribution at the beam boundary, but did not possess the symmetry about the high-voltage planes H necessary for periodic focusing. The solution discussed here also satisfies the voltage distribution at the beam boundary approximately, but, in addition, it possesses the necessary symmetry about low- and high-voltage planes.

For the space-charge-free region outside the boundary of the ideal electrostatically focused electron beam, attempts at exact solutions by separation of variables and satisfaction of the previously mentioned boundary conditions by evaluation of Fourier coefficients lead to an infinite divergent series for both ribbon and cylindrical electron beams. This limitation is overcome when a simple approximation, which is sufficiently accurate for practical applications, is made to the ideal potential distribution.

Approximation to the Ideal Voltage Distribution at the Beam Boundary

The following approximate expression may be used to describe the voltage variation at the boundary of the electron beam:

---

[8] See Reference (6), p. 175, and J. R. Pierce, "Rectilinear Electron Flow in Beams," *Jour. Appl. Phys.*, p. 548, Vol. 11, August, 1940.

[9] L. A. Pipes, *Applied Mathematics for Engineers and Physicists*, Chap. XVII, McGraw-Hill Book Co., Inc., New York, N. Y., 1946.

[10] J. R. Hechtel, "Electrostatic Focusing of Microwave Tubes," *Microwave Jour.*, Vol. 3, pp. 82-83, Figs. 18 and 19, December, 1960.

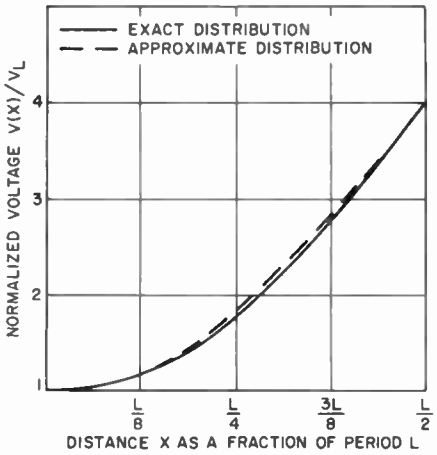

Fig. 3—Comparison between exact and approximate voltage distributions at the beam boundary.

$$V(x,0) = V_H - (V_H - V_L) \cos \frac{\pi x}{L}. \qquad (10)$$

This equation satisfies the condition of Equation (1) and gives the correct values of V_L and V_H at x equal to zero and $L/2$ respectively. In Table I and Figure 3 the actual and approximate values of voltages (Equations (2) and (10), respectively) are compared within a half-period LH for a low-to-high voltage ratio of 0.25, which, as mentioned previously, provides maximum current. Table I shows that, for this ratio, the accuracy of the approximate function (Equation (10)) is greater than 97 per cent. The differences between the actual and

Table I—Comparison Between Exact and Approximate Values of the Voltage at the Beam Boundary for a Low-To-High Voltage Ratio $V_L/V_H = 0.25$.

$\frac{2x}{L}$	$\frac{V(x)}{V_L}$		Per cent difference
	Exact (Equation (2))	Approximate (Equation (10))	
1	4.000	4.000	0
0.8520	3.250	3.309	1.815
0.6825	2.500	2.565	2.600
0.4721	1.750	1.788	2.171

approximate expressions at other voltage ratios are comparable to those shown in Table I.

Derivation of Optimum Focusing Electrodes for Ribbon and Hollow Electron Beams

The approximate equation for the voltage distribution outside the boundary of a ribbon electron beam is

$$V(x,y) = V_H - (V_H - V_L) \cos \frac{\pi x}{L} \cosh \frac{\pi y}{L}, \tag{11}$$

where y is the transverse coordinate measured from the beam boundary. This expression satisfies the following two-dimensional Laplace equation in Cartesian coordinates:

$$\frac{\partial^2 V(x,y)}{\partial x^2} + \frac{\partial^2 V(x,y)}{\partial y^2} = 0. \tag{12}$$

Equation (11) also satisfies the previously mentioned condition of zero radial electric field at the beam boundary, i.e.,

$$\left.\frac{\partial V(x,y)}{\partial y}\right|_{y=0} = 0. \tag{13}$$

At the beam boundary ($y = 0$), the potential is described by Equation (10). The degree of accuracy approaches the ideal voltage variation at the beam boundary as previously described. Equation (10) is symmetrical with respect to the plane $x = 0$. At $x = L/2$, there exists an equipotential plane V_H extending in the positive transverse direction (y) from the beam boundary to infinity. Therefore, in the interval $0 \leq x \leq L/2$, the potential distribution, Equation (11), possesses the properties necessary to generate the desired periodic field pattern. In this interval, $V(x,y)$ represents the voltage in the space-charge-free region in an LH interval shown in Figure 1. As mentioned previously, the distribution in an HL interval is the mirror image of that in an LH interval.

Figures 4(a) through (c) show the equipotential lines within a half-period LH expressed in terms of the low voltage V_L at the beam boundary for several values of low-to-high voltage ratios. The symbol R denotes the ratio between the voltage of a given equipotential surface and the low voltage, V_L. These figures show that the zero equipotential

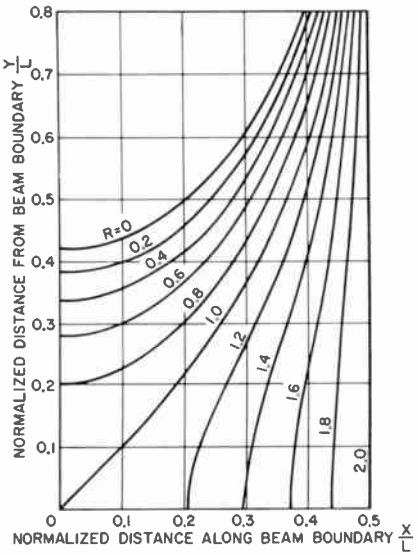

(a)

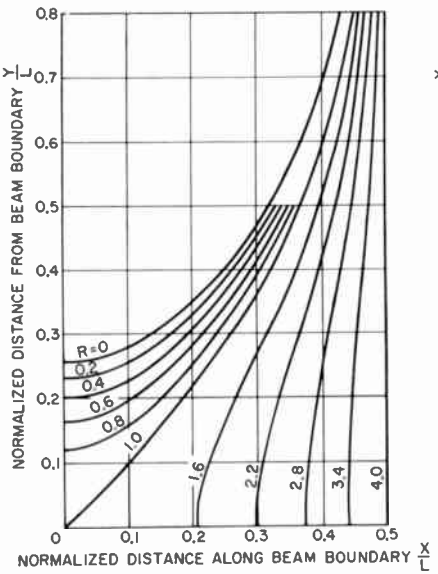

(b)

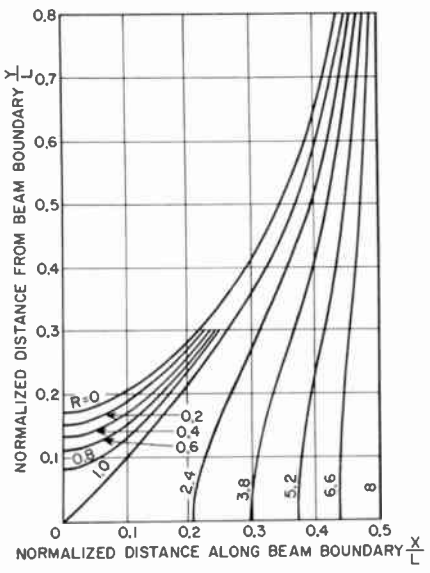

(c)

Fig. 4—Voltage distribution outside the planar beam boundary for (a) 2:1 voltage ratio at that boundary, (b) 4:1 voltage ratio at that boundary, and (c) 8:1 voltage ratio at that boundary.

moves closer to the beam boundary as the ratio V_L/V_H decreases. Ideally, the optimum electrodes for periodic electrostatic focusing of ribbon electron beams are infinitely thin high-voltage elements extending from the beam boundary for a relatively long distance and alternated with low-voltage electrodes operating at a potential equal to or lower than the voltage V_L.

The shape of the low-voltage focusing electrodes is determined by the value of R chosen in the range $0 \leq R \leq 1$ (see Figures 4(a) through (c)). The electrode shape chosen depends upon the desired application.

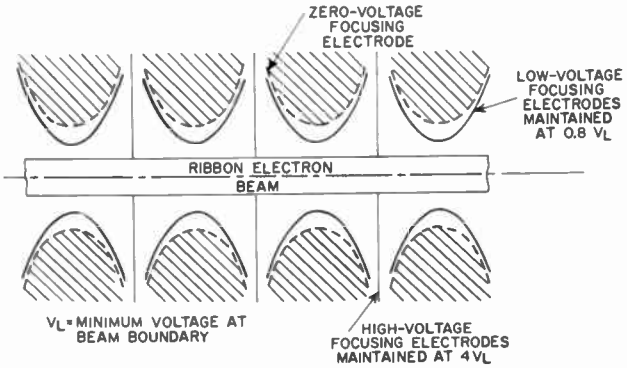

Fig. 5—Periodic electrodes for electrostatic focusing of a long, ribbon electron beam.

For example, the solid lines in Figure 5 show the optimum electrode shapes for focusing a ribbon beam by a low-to-high voltage ratio of 0.25 at beam boundary and with low-voltage electrodes maintained at the potential 0.8 V_L. The dashed lines show the shapes of zero-voltage electrodes which, in conjunction with the infinitely thin high-voltage elements, also produce a low-to-high voltage ratio of 0.25 at the boundary of the electron beam. This technique permits electrostatic beam focusing by a single supply voltage.

The curves shown in Figure 5 can also be used to design electrodes for focusing a hollow electron beam having a thickness t considerably smaller than the beam diameter D. The shape of these electrodes can be obtained by revolving the curves shown in Figure 5 about the center of the hollow electron beam.

Derivation of Optimum Focusing Electrodes for Cylindrical Electron Beam

The approximate equation for the potential distribution outside the boundary of a cylindrical axially symmetric electron beam is

$$V(x,r) = V_H - (V_H - V_L)\frac{\pi b}{L}\left[I_1\left(\frac{\pi b}{L}\right)K_0\left(\frac{\pi r}{L}\right) + K_1\left(\frac{\pi b}{L}\right)I_0\left(\frac{\pi r}{L}\right)\right]\cos\frac{\pi x}{L} \tag{14}$$

where r is the radial coordinate measured from the center of the beam and b is the radius of the beam. I_0 and I_1, the modified Bessel functions of the first kind are of zeroth and first orders, respectively; K_0

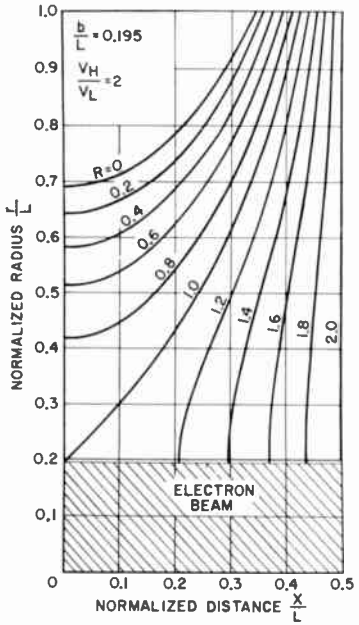

Fig. 6—Voltage distribution outside the cylindrical beam boundary for a beam radius-to-period ratio of 0.195 and a 2:1 voltage ratio at that boundary.

and K_1 are the Bessel functions of the second kind.[11] Equation (14) satisfies the following Laplace equation in cylindrical coordinates:

$$\frac{1}{r}\frac{\partial}{\partial r}\left(r\frac{\partial V}{\partial r}\right) + \frac{\partial^2 V}{\partial x^2} = 0. \tag{15}$$

It can be shown by use of a well-known relationship[12] for modified

[11] N. W. McLachlan, *Bessel Functions for Engineers*, pp. 102-103, Eqs. (3) and (6), Oxford Clarendon Press, 1934.

[12] J. R. Pierce, *Traveling-Wave Tubes*, D. Van Nostrand Co., Inc., New York, N. Y., 1950. Substitute zero for ν in Eq. (12), p. 224.

Bessel functions that Equation (14) is reduced to Equation (10) at the beam boundary, i.e., when r is equal to b. Another well-known relationship* for modified Bessel functions can be used to show that the radial electric field at beam boundary is zero (Equation (4)).

Equation (14) possesses the properties necessary for the formation of the periodic field pattern (discussed in connection with the design of electrodes for ribbon electron beams).

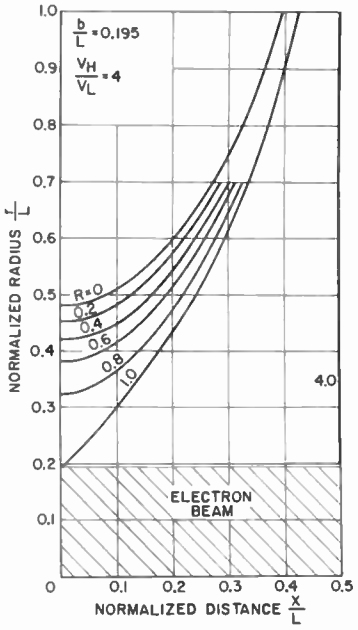

Fig. 7—Voltage distribution outside the cylindrical beam boundary for a beam radius-to-period ratio of 0.195 and a 4:1 voltage ratio at that boundary.

Figures 6 through 8 show the equipotentials outside the beam boundary for a beam radius-to-period ratio of 0.195 and for several voltage ratios at the beam boundary. The beam radius-to-period ratio used is a typical value for electrostatically focused traveling-wave-tube applications. The shape and distance from the cylindrical beam boundary of equipotentials for beam radius-to-period ratios in the range $0.15 \leq b/L \leq 0.245$ (typical for most practical applications) are essentially the same as those shown in Figures 6 through 8. These figures can be used to determine the shape of the periodic focusing electrodes in a manner similar to that discussed in connection with Figure 5. For

* See Reference (12), p. 224, Eq. (7).

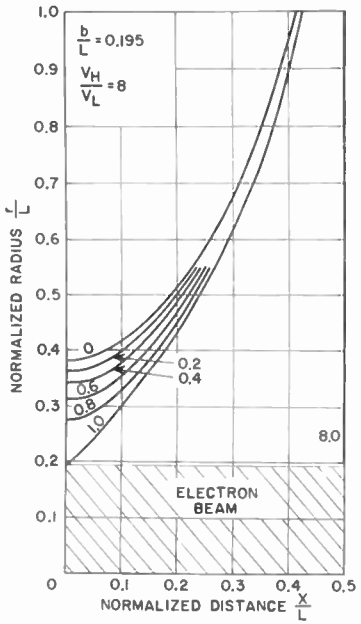

Fig. 8—Voltage distribution outside the cylindrical beam boundary for a beam radius-to-period ratio of 0.195 and an 8:1 voltage ratio at that boundary.

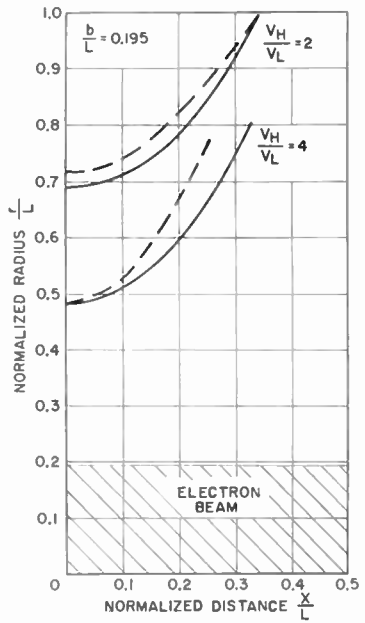

Fig. 9—Comparison between zero-voltage electrodes given by Hechtel[12] (dashed lines) and those presented in this paper (solid lines).

beam radius-to-period ratios in the previously mentioned range the approximate shape of the low-voltage electrodes can be derived by selecting the desired low-voltage equipotential from Figures 6 through 8 and revolving it about the beam axis in such a manner that the distance between the beam boundary and the given equipotential is the same as that for the beam radius-to-period ratio of 0.195. This procedure is sufficiently accurate for practical applications. For voltage ratios other than those shown in Figures 6 through 8, the shapes of the low-voltage electrodes must be computed from Equation (14).

Figure 9 shows a comparison between the electrode shapes obtained by Hechtel[10] (dashed lines) and those derived from the results presented in this paper (solid lines).

CHARACTER RECOGNITION BY DIGITAL FEATURE DETECTION*

By

I. H. Sublette and J. Tults

RCA Laboratories,
Princeton, N. J.

Summary—*Some logical design techniques are proposed which may be useful in the development of a multi-font reading machine. Characters are recognized by detecting the presence of certain combinations of geometric features which tend to be independent of changes in style and imperfections in printing. The effectiveness of these techniques has been tested by simulating them on a general-purpose computer. In the simulation program, the detection of 56 features is required to recognize 29 alpha-numeric characters. A recognition accuracy of about 75 per cent is obtained with characters that are badly distorted but still recognizable by human beings. Samples of distorted characters are produced by a computer program which simulates common types of printing imperfections.*

Introduction

MANY DATA-PROCESSING SYSTEMS require that information handled by digital computers be derived from documents printed in alphabetical and numerical characters. Reading machines which can recognize printed characters and convert them to computer codes are therefore important to the further development of the computing art. Machines capable of reading printed characters of a specially designed font are in commercial use today, but the problem of designing an economical machine capable of reading many different fonts has not been solved completely. The solution of this problem will be an essential contribution to the fields of language translation and information retrieval.

This paper proposes logical design techniques which may be useful in the development of a multi-font reading machine. Recognition is accomplished by detecting the presence of certain combinations of geometric features which can be used to identify characters regardless of differences in style and imperfections in printing. Similar ap-

* Manuscript received December 26, 1961.

proaches have been taken by Unger,[1] Bomba,[2] Grimsdale,[3] and others. A special purpose digital computer capable of reading machine-printed characters is proposed and tests of its performance by simulation on a general purpose computer are discussed. The logical design of the proposed machine and the results of the simulation program are presented.

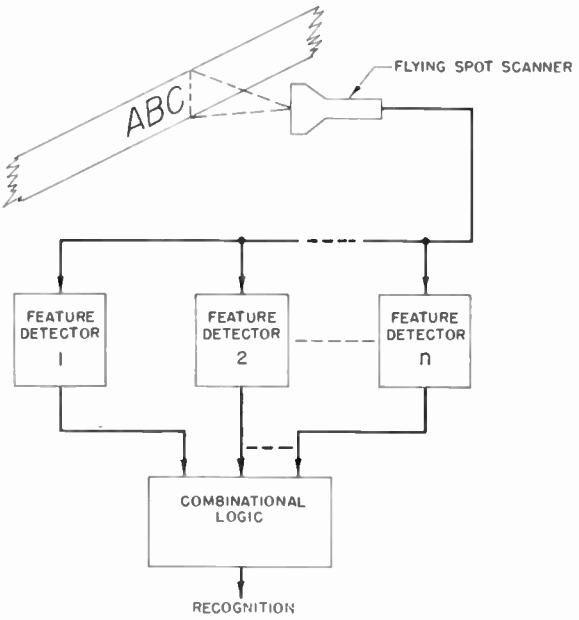

Fig. 1—General organization of proposed reading machine.

Principles of the Proposed Reading Machine

The logical organization of the proposed machine is outlined in Figure 1. A character is scanned by a series of vertical sweeps which progress across the character from left to right as shown in Figure 2. After being quantized into black and white levels, the video signal is

---

[1] S. H. Unger, "Pattern Detection and Recognition," *Proc. I.R.E.*, Vol. 47, p. 1737, October, 1959.

[2] J. S. Bomba, "Alpha-Numeric Character Recognition Using Local Operations," *Proc. Eastern Joint Computer Conf.*, p. 218, 1959.

[3] R. L. Grimsdale, F. H. Sumner, C. J. Tunis, and T. Kilburn, "A System for the Automatic Recognition of Patterns," *Proc. I.E.E.*, Vol. 106, Part B, p. 210, March, 1959.

sent to an array of feature detectors. Each feature detector is a small digital computer which detects the presence of some significant feature of the character while it is being scanned once with the raster of Figure 2. To obtain a high reading rate, the feature detectors are required to operate simultaneously. It is also required that the scanning rate be independent of the number of feature detectors employed.

This procedure, in which the elements of a character are examined sequentially and features are detected simultaneously, is not the only way of obtaining a high reading rate. Unger,[1] for example, has proposed a character recognition system in which all elements of the

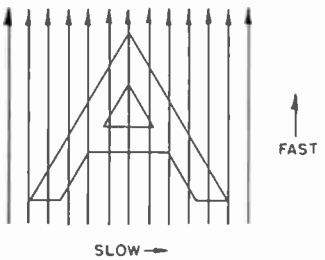

Fig. 2—Scanning pattern.

character are examined simultaneously and features are detected sequentially. The logical organization proposed here was chosen for several reasons. First, a sequential, rather than a simultaneous, examination of the character image simplifies the pick-up device without necessarily sacrificing reading speed. In any system in which the point of attention moves continuously from character to character, it is not likely that much time will be wasted in the scanning movement across each character. Also, the independence of the reading speed and the number of features detected may be an important advantage.

Second, the use of vertical scanning lines simplifies the problems caused by variations in character position. Ordinarily, the white spaces between lines of print are large enough to permit positioning the raster so that each vertical scanning line contains information from only one character. With horizontal scanning lines and characters which are closely-spaced within a line of print, it is likely that many scanning lines would contain information from more than one character. Spiral, circular, and diagonal scans also have been rejected because they tend to require accurate *a priori* knowledge of the character position.

A third advantage of the proposed scanning pattern is that its

cyclic nature allows the repetitive use of simple algorithms. In the simulation program,* it is only necessary to provide a single subroutine for all vertical scans. The results obtained from the subroutine during one scan are fed back to become part of the input data for the succeeding scan. Recursive procedures of this type generally have been required to obtain efficiency in the execution of complex logical tasks.

Table I—Simplified Chart of Combinational Logic for Recognizing a Sans-Serif, Upper-Case "A"

Feature	*Type of A's* 1	2	3	4	5	6
1. Long Flat Top Edge	No	No	No	No	No	No
2. Long left-hand vertical stroke	No	No	No	No	No	No
3. Long right-hand vertical stroke	No	No	No	No	No	No
4. Concave top edge	No	No	No	No	No	No
5. Enclosed white region	Yes	Yes				
6. Positive slope in top edge at left			Yes	Yes		
7. Negative slope in top edge at right					Yes	Yes
8. Indentation in bottom edge at left	Yes		Yes		Yes	
9. Indentation in bottom edge at right		Yes		Yes		Yes

In the simulation program, each character is isolated from other characters and is located within a raster consisting of twenty vertical scans. The subroutine which simulates the network of combinational logic is entered after the completion of the twentieth scan. This subroutine recognizes an alphabet of 29 alpha-numeric characters by detecting the presence of various combinations of 56 different features. Table I presents a simplified version of the logic used to recognize an upper-case, sans-serif "A". To allow for distortions due to printing imperfections, six different types of A's are allowed. Each of the first

* In this paper, the recognition system frequently will be described in the language of programming, rather than logical design, because the terminology is more convenient.

four features listed in Table I is assumed to give overwhelming evidence that the character being examined is not an "A". The remaining five features are assumed to present evidence in favor of an "A", but at least two of these features must be present, and no single feature is required for recognition.

Detailed Description of Feature Detection

Edge Tracers and Edge Labels

Most of the features detected are properties of the inside and outside edges of a character, such as flat segments, sloping segments, and

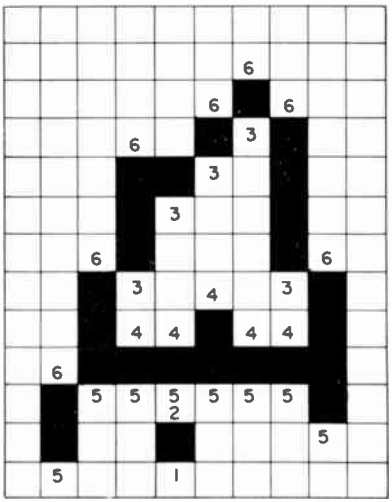

Fig. 3—Typical labelling of edges in a character.

segments with various types of curvature. These properties are detected by a group of "edge tracers." The present simulation program contains six edge tracers, three of which trace "top edges," and three of which trace "bottom edges." A top edge is an edge that causes a black-to-white transition as the scanning spot travels from the bottom of a character to the top. A bottom edge is an edge that causes a white-to-black transition. In Figure 3, the edges labeled 1, 3, and 5 are bottom edges, and the edges labeled 2, 4, and 6 are top edges. In general, the labels for bottom and top edges are drawn from the sets (1, 3, 5) and (2, 4, 6), respectively. No two edges are ever assigned the same label. If more than six transitions are encountered in one

vertical scan, at least one pair of edges must be ignored, since only six edge tracers are provided.*

The label for a given edge also identifies the tracer which is assigned to it. The function of edge tracer n is to compute certain properties of the function $y_n(x)$, where x is the number of vertical scans which have been performed (including the present scan) and y_n is the distance from the lower boundary of the raster to edge n in the present vertical scan. Since the scanning raster consists of 20 vertical scans, each of which is divided into 24 cells, x and y_n take on integral values in the domains $(1 \leq x \leq 20)$ and $(1 \leq y_n \leq 24)$. Since all edge tracers are essentially identical, the subscript n usually will be omitted.

When fewer than six transitions are detected in a vertical scan, at least one pair of edge tracers will not be performing computations and will be said to be "inactive." All tracers performing computations will be said to be "active." The operations of "starting" and "retiring" an edge tracer consist of sending an edge tracer into the active and inactive states, respectively.

Edge-Tracing Computations

Edge-tracing operations are performed when a white-to-black or a black-to-white transition is detected during a scan† and at the end of each scan. For each transition detected during a scan, the corresponding value of y is recorded in the memory of the appropriate edge tracer. The value of y recorded for a white-to-black transition is the coordinate of the black cell; the value recorded for a black-to-white transition is the coordinate of the white cell. The execution of algorithms for edge-tracing is ordinarily postponed to the end of each scan, where the relative positions of the edges can be determined most easily. An exception to this procedure occurs when two edges are terminated during a scan. Then the edge-tracing computations for that pair of edges are performed immediately so that the edge tracers may be retired and made available for assignment to new edges which may appear as the scanning proceeds. In Figure 3, for example, edge tracers 3 and 4 are retired during the ninth scan.

Tables II and III describe algorithms for computing flatness and positive slope in an edge, respectively. These algorithms are entered once every scan. The constant x_0 denotes the number of the scan in

* The use of only six edge tracers is a compromise between complexity and performance. There is no logical difficulty in providing more tracers.

† For the sake of brevity, a vertical scanning line will be referred to simply as a "scan."

Table II—Algorithm for Computing Flatness $f(x)$

1.	$d(x_0) = 0$	
2.	$d(x) = y(x) - y(x-1)$	$x > x_0$
3.	$e(x) = 0$	$x \leq x_0 + 1$
4.	$e(x) = y(x) - y(x-2)$	$x > x_0 + 1$
5.	$f(x_0) = 1$	
6.	$f(x) = 1$ if $\lvert d(x)\rvert > 1$ or $\lvert c(x)\rvert > 1$	$x > x_0$
7.	$f(x) = f(x-1) + 1$ if $\lvert d(x)\rvert \leq 1$ and $\lvert e(x)\rvert \leq 1$	$x > x_0$

which edge-tracing computations were started. For any function $z(x)$ computed by an edge tracer, it is understood that $z(x) = 0$ for $x < x_0$. Since the detailed procedures for computing functions such as flatness and slope are not crucial, a complete discussion of these and other edge-tracing algorithms contained in the simulation program will be omitted.

Addressing Edge Tracers

The edge labels shown in Figure 3 cannot serve as direct addresses of data in the corresponding edge tracers because there is no predictable relationship between the labels and the transitions detected by the scanner. Edge tracer 6, for example, may acquire a y-coordinate from the second, fourth, or sixth transition. In the simulation program, the first level of addressing is performed by selecting one of six index registers I_1 through I_6. Index register I_m is identified with the m^{th} transition from the bottom of the present scan. The number stored in index register I_m is the label of the edge which currently corresponds to the m^{th} transition. Corresponding items of data for the six edge tracers are stored in six consecutive memory locations

Table III—Algorithm for Computing Positive Slope $s(x)$

1.	$c(x) = 0$	$x \leq x_0 + 1$
2.	$c(x) = y(x-1) - y(x-2)$	$x > x_0 + 1$
3.	$s(x_0) = 0$	
4.	$s(x) = 0$ if $d(x) > 4$ or $d(x) < 0$	$x > x_0$
5.	$s(x) = 0$ if $c(x) = 0$ and $d(x) = 0$	$x > x_0$
6.	$s(x) = s(x-1)$ if $c(x) \neq 0$ and $d(x) = 0$	$x > x_0$
7.	$s(x) = s(x-1) + 1$ if $0 < d(x) \leq 4$	$x > x_0$

such that if item z_1 in edge tracer 1 is stored at address $A + 1$, item z_n for edge tracer n is stored at address $A + n$. The address of item z for the edge which is currently the m^{th} transition from the bottom is thus equal to $A + (I_m)$, where (I_m) denotes the contents of index register I_m.

When edge tracers are started or retired, it is usually necessary to shift the contents of the index registers to maintain the correct

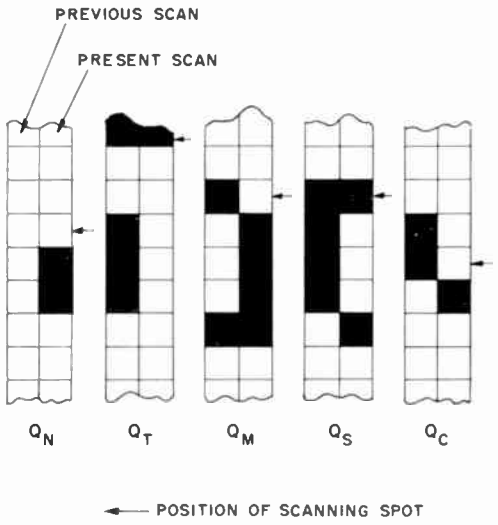

Fig. 4—Examples of patterns corresponding to edge control states.

mapping between the set of edge labels $\{n\}$ and the set of transition numbers $\{m\}$. Tests for conditions requiring such shifts are performed whenever a transition is detected and result in the generation of any one of five "edge-control states." Examples of patterns which correspond to edge-control states are shown in Figure 4. State Q_N indicates that two edge tracers must be started because of the presence of a new black region. State Q_T indicates that two edge tracers must be retired because of the termination of an old black region. State Q_M indicates that two edge tracers must be retired because of the merging of two black regions into one. State Q_S indicates that two edge tracers must be started because a single black region has split into two black regions. State Q_C indicates that a black region has continued into the present scan without splitting, and thus indicates that no shifting of index-register data is required.

The generation of an edge-control state depends upon two variables

which have not been defined previously. The first of these is k, which denotes the number of transitions detected since the beginning of the present scan, including the transition at which the scanning spot is currently resting. The second is Y, the present vertical coordinate of the scanning spot. The domains of these variables are $(0 \leq k \leq 6)$ and $(1 \leq Y \leq 24)$. An edge-control state is generated as a result of certain tests performed on data stored in an edge tracer which is indirectly specified by k. These tests are defined in Table IV. In the

Table IV—Rules for Generating Edge Control States

Edge Control State to be Generated	*Type of Transition*	*Index Register For Addressing Edge Tracer*	*Conditions on Edge Tracer*
Q_N	black-to-white	I_{k-1}	Edge tracer inactive or edge tracer active and $Y-y(x-1) < 0$
Q_T	white-to-black or end of scan	I_{k+1}	Edge tracer active and $Y-y(x-1) > 0$
Q_M	black-to-white	I_{k+1}	Edge tracer active and $Y-y(x-1) \geq 0$
Q_S	white-to-black	I_{k-1}	Edge tracer active and $Y-y(x-1) \leq 0$
Q_C	black-to-white	I_{k-1}	Edge tracer active and $Y-y(x-1) \geq 0$ and not Q_M

rules for generating state Q_T, or for specifying operations to be performed in this state, the end-of-scan position is counted as a transition in computing the value of k.

Table V specifies the conditions under which certain shifts of index-register data must be performed. An expression such as $(I_1) \rightarrow I_3$ denotes that the number previously stored in I_1 is to be stored in I_3. Scanning of a character must begin with an initial assignment of index values. The sequence of edge labels shown in Figure 3 is obtained with the initial assignment $(I_m) = m$. Table V also specifies the conditions under which edge tracers are started and retired. The starting, S, and retiring, R, of an edge tracer whose label was previously stored in index register I_m are denoted by the expressions $S \rightarrow [I_m]$ and $R \rightarrow [I_m]$, respectively.

All possible sequences of edge-control states are shown in Figure 5. In state Q_A (not previously defined), the scanning spot is advancing to the next transition and no computing operations are being performed. Upon the detection of a transition, a shift from state Q_A to one of the five states defined by Table IV may occur.* The operations performed in states Q_N, Q_T, Q_M, and Q_S have been summarized in Table

Table V—Conditions Requiring Shifting of Index Register Data And the Starting and Retiring of Edge Tracers

Operation	Q_N			Q_T			Q_M		Q_S	
		k			k			k		k
	2	4	6	1	3	5	2	4	3	5
$(I_1) \rightarrow I_3$	X									
$(I_1) \rightarrow I_6$				X						
$(I_2) \rightarrow I_4$	X								X	
$(I_2) \rightarrow I_6$				X			X			
$(I_3) \rightarrow I_5$	X	X			X		X		X	
$(I_4) \rightarrow I_6$	X	X			X			X	X	X
$(I_3) \rightarrow I_1$				X						
$(I_4) \rightarrow I_2$				X			X			
$(I_5) \rightarrow I_3$		X		X	X		X		X	
$(I_5) \rightarrow I_1$	X									
$(I_6) \rightarrow I_4$		X		X	X		X	X		X
$(I_6) \rightarrow I_2$	X								X	
$S \rightarrow [I_5]$	X	X	X						X	X
$S \rightarrow [I_6]$	X	X	X						X	X
$R \rightarrow [I_1]$				X						
$R \rightarrow [I_2]$				X			X			
$R \rightarrow [I_3]$					X		X			
$R \rightarrow [I_4]$					X			X		
$R \rightarrow [I_5]$						X		X		
$R \rightarrow [I_6]$						X				

V. The sequences $Q_T \rightarrow Q_T$ and $Q_M \rightarrow Q_M$ are possible because it may be necessary to retire more than one pair of edge tracers upon the detection of a single transition. Figure 6 shows examples of patterns for which two pairs of edge tracers must be retired for a single position of the scanning spot.

* For a black-to-white transition, a jump to one of the three states Q_N, Q_M, or Q_C will always occur. For a white-to-black transition, a jump to state Q_T or Q_S is possible but not necessary. If neither Q_T nor Q_S is entered, the scanner advances to the next transition after the Y-coordinate for the present white-to-black transition has been recorded.

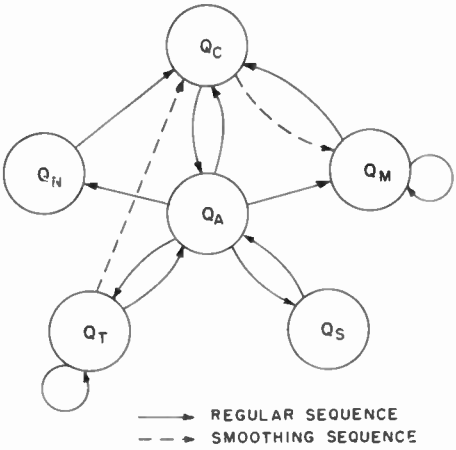

Fig. 5—Sequence diagram for edge control states.

When a black-to-white transition is detected, the value of Y corresponding to the present transition and the previous white-to-black transition are stored as the new values of $y(x)$ in the appropriate pair of edge tracers. This storing operation is performed only in state Q_C. Since states Q_N and Q_M also occur with a black-to-white transition, both of these states are immediately followed by state Q_C. When all operations required for a transition have been completed, state Q_A is entered and the scanning spot advances to the next transition.

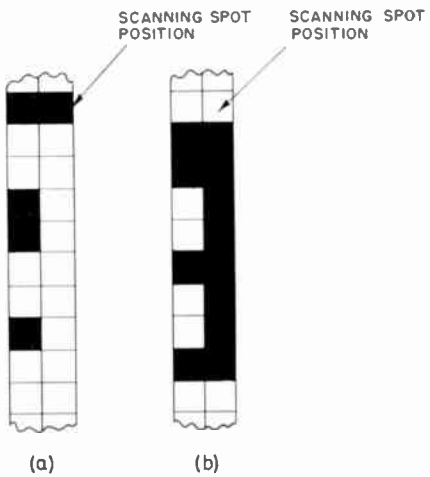

Fig. 6—Examples of patterns requiring the retirement of two pairs of edge tracers for a single position of the scanning spot: (a) pattern causing the sequence $Q_T \rightarrow Q_T$; (b) pattern causing the sequence $Q_M \rightarrow Q_M$.

White Regions

In principle, all of the information in a character is contained in its edges. For increased efficiency, however, the proposed machine stores and manipulates redundant information which describes directly the white regions formed by the inside boundaries of a character. In Figure 3, items of data would be stored for the white region bounded by edges 3 and 4 and for the much smaller region bounded by edges 2 and 5. In general, the white region bounded by the top edge p and the bottom edge q is denoted by W_{pq} and the corresponding data is stored as data belonging to edge tracer p.

One item of data stored for white region W_{pq} is the maximum vertical separation between edges p and q. Typical uses of this quantity are to measure the height of the region in the character "O" and to measure the height of the right-hand concave region in the "C". Another item stored for a white region indicates whether the region is open or closed on left. In the character "S", for example, the top white region is usually closed on the left and the bottom region is usually open on the left. The decision as to whether a particular white region is open or closed on the left is continuously re-examined as additional features of the character are detected during the scanning period.

Smoothing Operations

Smoothing operations which eliminate small imperfections in patterns or cause them to be ignored generally simplify feature detection. Small, isolated specks tend to be ignored automatically by edge tracers because the associated edges are too short to have significant properties. For longer edges it is helpful to invoke special procedures for smoothing ragged edges and joining broken edge segments.

One method of smoothing ragged edges is to make certain exceptions to the rules of Table V for retiring edge tracers in states Q_T and Q_M. In both examples shown in Figure 7, edge tracer 2 ordinarily would be retired. However, edge tracer 4 is retired instead because the indentation detected in the present and previous scans is shallow compared to the length of edge 2. Thus the continuity of operation in edge tracer 2 remains uninterrupted.

A vertical gap between two black regions can be closed as shown in Figure 8. When state Q_C exists and at least two white-to-black transitions have already been detected in the present scan, a test is made to determine whether the preceding vertical gap should be closed. One such test is to compare the length of the gap L with the maximum height H of the white region to the left; if the ratio L/H is small, the

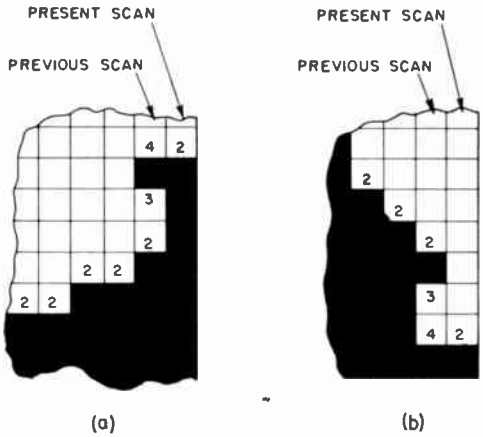

Fig. 7—Edge smoothing by exceptions to rules for shifting index register data (a) in state Q_M and (b) in state Q_T.

gap is closed. If the decision to close is made, the gap is eliminated by entering state Q_M, in which edges 1 and 2 will be retired. This smoothing operation is indicated in Figure 5 by the broken arrow directed from Q_C to Q_M. Edges 1 and 2 are now available for assignment to any new edges which may appear as the scanning proceeds.

Black regions also may be extended to the right by modifying the operations performed in state Q_T (see Figure 4). Instead of performing the operations specified by Table V, an immediate transfer is made to state Q_C in which new values of $y(x)$ are stored for the pair of edges which ordinarily would have been retired in state Q_T. In effect, the black region bounded by these edges is extended artificially into

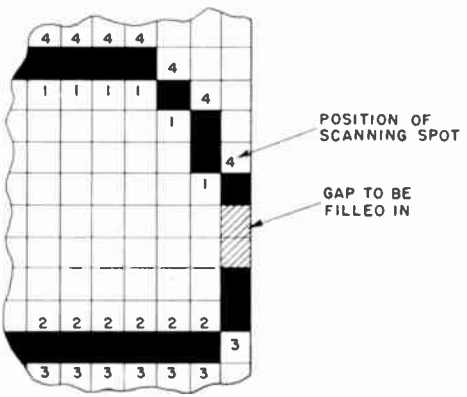

Fig. 8—Closing of a vertical gap by means of the sequence $Q_C \rightarrow Q_M$.

the present scan. This smoothing operation is indicated in Figure 5 by the broken arrow directed from state Q_T to Q_C. The data stored for each edge includes a count of the number of times it has been extended to the right. In the simulation program, an edge that is only one cell wide is never extended, and no edge is ever extended for more than three scans.

Examples of Features Detected

Of the 56 features detected in the simulation program, 5 indicate the presence of various kinds of vertical strokes, 32 describe the properties of edges, 13 describe the properties of white regions, and 6 lie

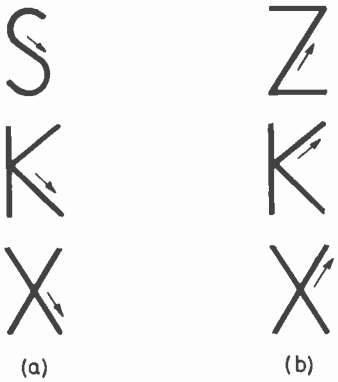

Fig. 9—Two features using slope data and the relative positions of edges: (a) negative slope on inside top edge and (b) positive slope on inside bottom edge.

in a miscellaneous category. The typical feature is specified with a precision of about 2 bits. Vertical strokes, for example, are classified as short, medium, and long.

The length of a vertical stroke can be computed in state Q_C by subtracting the Y-coordinate of the previous white-to-black transition from the Y-coordinate of the present black-to-white transition. Vertical strokes, in addition to being classified according to length, are classified according to their horizontal position.

Examples of two features which specify the relative positions of edges as well as the properties of individual edges are shown in Figure 9. One of these features indicates the presence of a negative slope in a top edge which is the second top edge from the top of a character. The other feature indicates the presence of a positive slope in a bottom edge which is the second bottom edge from the bottom of a character. These features are used to provide positive evidence in favor of the

characters shown in Figure 9 and in certain cases may inhibit the recognition of other characters, including the letter "A" (see Table I). A method for computing the slope of an edge has been presented in Table III. The position of an edge relative to other edges can be determined easily during the edge-tracing computations because the label of an edge which currently corresponds to the m^{th} transition is known to be stored in index register I_m.

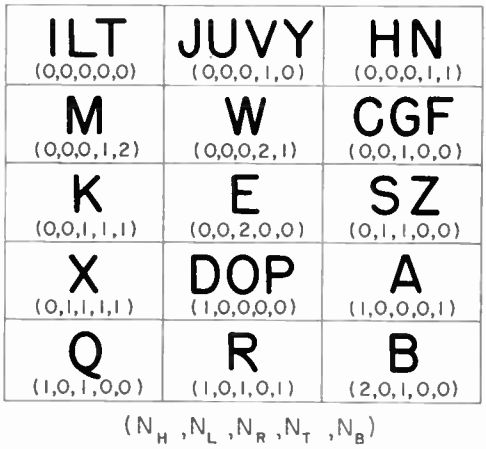

Fig. 10—Hole-and-cavity description of characters.

The features extracted from white regions are "holes" and "cavities," which were applied in a reading machine proposed by Rochester.[4] A hole is a white region surrounded by black; a cavity is a concave region along the boundary of a character. Figure 10 shows how a typical set of ideal, sans-serif capital letters is partitioned on the basis of the 5-tuple (N_H, N_L, N_R, N_T, N_B), in which the five symbols refer to the number of holes, left cavities, right cavities, top cavities and bottom cavities. Holes are always detected in state Q_M. In Figure 3, for example, a hole will be detected when edges 3 and 4 are retired in state Q_M. Data from edge tracers 3 and 4 are used to determine the width of the hole and any significant properties of the inside boundary of the hole. Data associated with white region W_{43} are used to determine the height of the hole and to determine that W_{43} is closed to the left. Left cavities are detected in a similar manner, except that the white region must be open on the left. At the end of each scan, a

[4] N. Rochester, *et al.*, U. S. Patent 2,889,535.

white region which is closed on the left is tentatively identified as a right cavity. The later detection of a right closure in state Q_M may cause a right-cavity feature to be changed to a hole. Top and bottom cavities are detected by edge-tracing algorithms.

Estimation of the Recognition Speed

An estimation of the recognition speed of the proposed system can be based on the assumption that almost all of the time required for recognizing a character will be spent in the computations required when the scanning spot strikes a transition or an end-of-scan position. The time consumed by the scanning spot in moving between transitions and in retracing from one scan to the next can be neglected.

It would be possible to design a special-purpose machine in which a computing cycle is entered a maximum of seven times in one scan—six times upon the detection of transitions, and once at the end of the scan. If it is assumed that the average character is 15 scans wide, the average number of computing cycles required for one character would be less than 100. If all edge tracers were operating simultaneously, and if many operations within each edge tracer were performed in parallel, an average of ten clock pulses probably would be sufficient for one computing cycle. Thus a one-megacycle clock rate would produce a reading rate faster than 1000 characters per second.

Computer Simulation Program

The effectiveness of this system of character recognition has been tested by simulating it on a large-scale general-purpose computer. The present version of the simulation program recognizes an alphabet of 29 alpha-numeric characters. This alphabet consists of the set of 36 upper-case letters and numerals from which the letters Q and V and the numerals 0, 1, 2, 5, and 8 have been omitted.* Experiments have been performed with a sans-serif font used in a line printer at RCA Laboratories. Attention has been limited to this simple case to concentrate on the problem of overcoming imperfections in printing. The simulation program contains about 1800 instructions and recognizes characters at the rate of one per second.

Samples of characters have been obtained from a computer program

* The numerals 0, 1, 2, 5, and 8 have been removed because of their similarity to the letters O, I, Z, S, and B, respectively. The letters Q and V have been removed because of their similarity to the O and Y, respectively. All of these characters can be distinguished, but there seems to be little point in attempting to do so until the specified fonts to be read have been determined.

which generates synthetic characters of low quality. It has been necessary to use synthetic characters because the frequency of deteriorated characters in actual samples of printing tends to be very low. With samples of real characters, perhaps only one out of 1000 characters would be distorted severely enough to be interesting. Since the simulation program requires about one second to recognize a single character, too much computing time would be required to obtain significant results. With synthetic characters, the frequency of interesting cases can be increased to about ten percent.

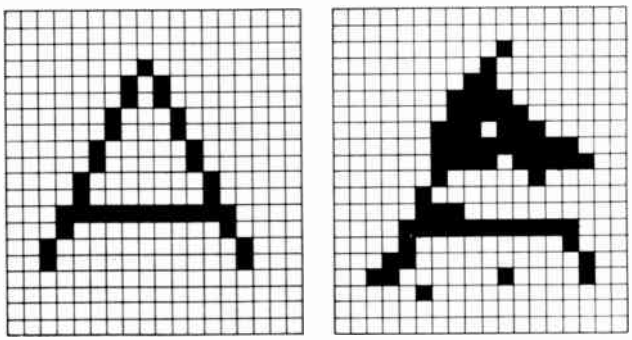

Fig. 11—Typical result obtained from character distortion program: (a) ideal character supplied to input; (b) sample of distorted character produced by the program.

The method of producing distorted characters is similar to that proposed by Greanias and Hill.[5] An ideal, thin-line sample of the font under study is the input to the computer. The program distorts an input character to simulate variations in ink density and non-parallel alignment between the type slug and the paper. Each input sample is subjected to eight types of distortion. In four of these, the density of printing is greater than normal, and in the other four the density is less than normal. Within both groups of four, parameters are adjusted to produce one sample each of characters which are relatively weak on the left side, right side, top, and bottom. Figure 11 shows an ideal, thin-line character supplied to the computer and a sample of a corresponding distorted character. The program for generating synthetic characters produces samples at a rate of about one per second.

[5] E. C. Greanias and Y. M. Hill, "Considerations in the Design of Character Recognition Devices," *I.R.E. Convention Record, Part 4, Automatic Control*, p. 119, 1957.

Since the main purpose of the simulation studies has been to suggest improved recognition methods, the logic of recognition has been revised many times as a result of experience. Changes usually have been made after testing a system on only a few hundred characters. Consequently, information on error rates which is quantitatively significant is not available. A qualitative understanding of the performance of this recognition method can be obtained from Figures 12 and 13 which show samples of synthetic characters supplied to the simu-

Fig. 12—Synthetic characters recognized correctly by the simulation program.

lation program and the results obtained. When a character is supplied to the simulation program, three results are possible: (a) correct identification of the character; (b) incorrect identification; (c) rejection of the character due to the inability of the program to make a decision. In a typical run with a debugged program, 75 per cent of the characters are recognized correctly. With actual samples of printing, a much higher accuracy would be obtained. No tests have been made to determine the accuracy with which human beings would read

the synthetic characters, but it is estimated that the average human reader would read more than 95 per cent of them correctly.

Conclusions

Logical rules for recognizing printed characters have been devised and their effectiveness has been tested by simulation on a computer. More than 50 features are employed to recognize a simple 29-character

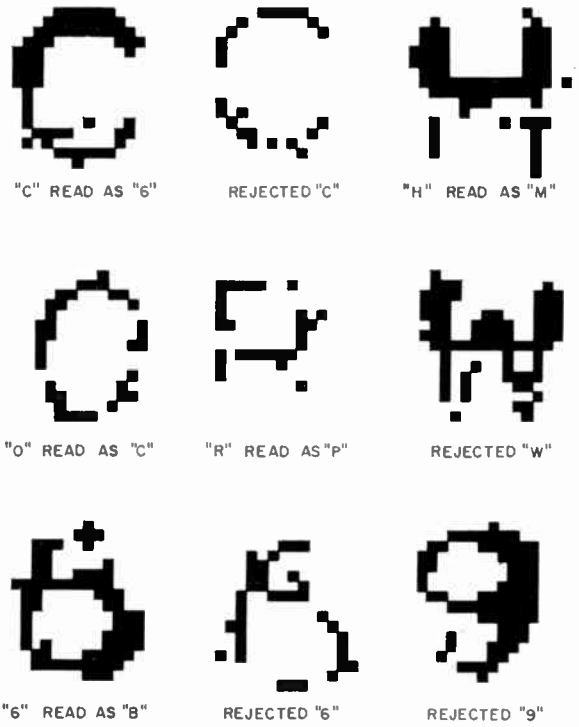

Fig. 13—Synthetic characters read incorrectly or rejected by simulation program.

alphabet. Although the recognition accuracy is probably good enough for certain commercial applications, it is significantly poorer than the accuracy of human reading. Still more complexity will be required to handle a wide variety of fonts, to recognize contiguous characters, and to locate lines of print interspersed with graphical material.

The reading rate of one character per second obtained with the simulation program is too slow for any practical application. A special-purpose machine capable of a usefully high speed could be designed

without increasing the speed of the basic circuit elements by providing simultaneous execution of many computing operations. It may be premature, however, to decide on a machine in which operations are performed more in parallel than in series. Experiments with the simulation program have produced a strong feeling that it will be desirable to be able to modify the logic of a reading machine even after it has been placed into service. Such changes could be made most easily if the machine were equipped with a stored-program type of control unit, and a sequential machine with only one computing organ could be provided with a stored program without incurring too much expense. In a parallel machine, the use of a separate stored program for each computing organ may be too expensive, and the use of only one stored program for controlling all computing organs may be too inflexible.

ACKNOWLEDGMENT

The authors would like to express their appreciation to Edward Helpert for his valuable assistance in the writing of a recent version of the simulation program.

PULSED RADAR MEASUREMENT OF BACKSCATTERING FROM SPHERES*†

By

SIMPSON B. ADLER

RCA Defense Electronic Products
Moorsetown, N. J.

Summary—This paper presents data on the performance of a pulsed radar as an instrument for the measurement of target cross section. Measurements made at 5518, 5600 and 5800 megacycles on 120 dielectric and aluminum spheres in the resonance region .74 ≤ $2\pi r/\lambda$ ≤ 4.6 show that a pulsed radar can obtain good agreement with Mie's theory in the critical size region.

New plots of radar cross section are given which were obtained from digital-computer solutions of the Mie scattering coefficients for Teflon,‡ Lucite,‡ Bakelite,‡ and aluminum spheres.

INTRODUCTION

PULSED RADAR is presently being used as an instrument for the measurement of target cross section. A determination of the accuracy of the radar in this application is therefore desirable. The approach described in this paper is to determine the ability of the radar to verify Mie's[1] theory for the case of backscattering from metal and dielectric spheres in the resonant region. This is the region where the size of the sphere is of the order of the incident wavelength. The resonant region was chosen for a number of reasons: radar is used to track objects in this critical size region, and perturbing small particle influences are usually present during tracking due to atmospherics, rain, fog, and the like. Also, scattering from spheres in the resonant region is of general interest in the fields of astronomy, chemistry, meteorology, and physics and there is great interest in determining the mechanism which causes resonance.

A great deal of theoretical and experimental work has been done in the field of electromagnetic scattering and it would be expected that

---

* This work is based on a thesis submitted to the Temple University Graduate Council in partial fulfillment of the requirements for the Ph.D. degree.

† Manuscript received 17 October 1961.

‡ Trade mark.

[1] G. Mie, *Ann. Physik*, Vol. 25, p. 377, 1908.

exhaustive measurements would have been made on such a simple and basic shape as the sphere. On the contrary, however, there is a scarcity of experimental data on spheres in contrast to the great deal of data on other shapes such as cylinders and cones. In particular, there seems to be a lack of data on the measurement of spheres by the use of tracking radar. Furthermore, those measurements that have been made give cross-section values for relatively large increments of sphere size, and experimental verification of theory in the resonant region is incomplete. A summary of experimental work on sphere scattering discovered from a search of the literature is shown in Table I. The list shows the parameters used for each experiment, namely, the refractive index, wavelength, scattering angle, and size. This does not include the extensive light-scattering experiments performed in the field of chemistry. Such experiments are made primarily to measure the properties of various chemical samples; the results are dependent on theory and are not performed to verify theory. Of the six experiments listed in Table I, three used scattering materials where large numbers of particles participated in the scattering. The assumption is made that the particles are sufficiently separated from one another that independent scattering occurs. These experiments were performed on fog, film, and powders in the visible and infrared regions of the spectrum. At these wavelengths there is, of course, considerable difficulty in obtaining scattering data on an individual sphere. Of the other three experiments performed in the microwave region, one used the standing-wave method to measure water and metal spheres, the second a synchronous detector to measure dielectric coated spheres, and the third a doppler measurement of conducting spheres. All of these measurements employed techniques to minimize background noise and to obtain, in effect, free-space isolation of the spheres. It may be seen, therefore, that measurements made on spheres thus far are by no means exhaustive. Data is available for only limited values of refractive index, scattering angle, wavelength, and size.

In the present investigation, a pulsed tracking radar was used to make radar cross-section measurements ($\theta = 180°$, backscattering) of 120 dielectric and metal spheres at 5518, 5600, and 5800 megacycles in the region $.74 \leq 2\pi r/\lambda \leq 4.6$, where r is the radius of the sphere and λ is the wavelength. The experiments were run on aluminum, Teflon, Lucite, and Bakelite spheres varying in radius by increments of 0.025 inch with the spheres machined to 0.001 inch. The measurements therefore serve the purpose of adding data to the verification of theory as well as determining how good the radar is as an instrument for measuring cross section.

Table I

Experiment	*Refractive Index*	*Wavelength*	*Angle*	*Size or size parameter*	*Remarks*
A. L. Aden J. Appl. Phys. V. 22, p. 601, 1951	Water & metal	16.23 cm	180° backscattering	0.74 to 5.90 $2\pi r/\lambda$	Water and 18 metal spheres. Standing-wave method (image technique)
E. L. Cleveland and R. C. Raymond J. Opt. Soc. V. 42, p. 183, 1952	Copper, carbonyl iron, and silver chloride	1.45 to 15 microns	0°	2-20 microns	Large random distribution on Pliofilm.* Number of spheres $\sim 10^5$.
D. Sinclair J. Opt. Soc. V. 37, p. 475, 1947	Stearic Acid Fog n = 1.43	.524 micron	3° to 175°	$2\pi r/\lambda = 2\text{-}8$	
A. H. Pfund J. Opt. Soc. V. 24, p. 143, 1934	Zinc Oxide and MgO pigment	Infra-red .4 to 2.7 microns	0°	.09 to 0.4 microns	Verified Rayleigh's law for small particles.
H. Scharfman J. Appl. Phys. V. 25, p. 1352, 1954	Several dielectric coated spheres	Microwave	180°	0.4 λ	Scattering in region of first resonance.
J. S. Hey et al. Proc. Phys. Soc. V. 69, p. 1038, 1956	Conducting spheres	3.22 cm.	Backscattering	.17 λ to 2.0 λ	Only twelve data points are given.

* Trade mark.

THEORY

A description of the scattering of a plane wave by a sphere was first presented by G. Mie in 1908.[1] The solution of this boundary-value problem for backscattering is given by[2]

$$\frac{\sigma}{\pi r^2} = \frac{1}{\rho^2} \left| \sum_{n=1}^{\infty} (-1)^n (2n+1) (a_n - b_n) \right|^2$$

where the scattering coefficients are given by

$$a_n = - \frac{j_n(\rho) [N\rho\, j_n(N\rho)]' - j_n(N\rho) [\rho\, j_n(\rho)]'}{h_n^{(2)}(\rho) [N\rho\, j_n(N\rho)]' - j_n(N\rho) [\rho\, h_n^{(2)}(\rho)]'}$$

$$b_n = - \frac{N^2 j_n(N\rho) [\rho\, j_n(\rho)]' - j_n(\rho) [N\rho\, j_n(N\rho)]'}{N^2 j_n(N\rho) [\rho\, h_n^{(2)}(\rho)]' - h_n^{(2)}(\rho) [N\rho\, j_n(N\rho)]'}$$

and σ is the radar cross section,

r is the radius of the sphere,

n is an integer,

$\rho = k_2 r = 2\pi r/\lambda$ (free space),

$N = k_1/k_2$ is the refractive index, with k_1 and k_2 the propagation constants within the sphere and the surrounding medium, respectively,

λ is the wavelength,

$j_n(\rho)$ and $h_n^{(2)}(\rho)$ are the spherical Bessel and Hankel functions, and the prime denotes differentiation with respect to the argument.

A number of workers in this field have called attention to the difficulty of reducing the solution to numerical results. This difficulty results from the lack of tables for the spherical functions of complex argument and the slow convergence of the series. In the present investigation, recursion relations were used to put the equations into a form that could be programmed on a digital computer. Solutions were computed to 5 places for values of $0.4 \leq \rho \leq 10$ in increments of 0.01 for metals, and for values $0.1 \leq \rho \leq 5$ in increments of 0.01 for the following dielectric materials: Teflon, $N = 1.45957 - 0.01897i$; Lucite, $N = 1.628 - 0.01953i$; Bakelite, $N = 1.98511 - 0.02481i$. A check

[2] D. E. Kerr (editor), *Propagation of Short Radio Waves*, Vol. 13, p. 451, McGraw-Hill Book Co., Inc., New York, 1951.

program was also run for water, $N = 8.18 - 1.96i$ at $\lambda = 3.0$ centimeters. These solutions for metal and dielectric spheres were used for comparison with experimental data, and are shown graphically in Figures 3 through 13 (solid lines).

The measurement of cross section using a pulsed radar is based on the classical radar equation[3]

$$\frac{S}{N} = \frac{P G^2 \lambda^2 \sigma}{(4\pi)^3 R^4 k T B NF L}$$

where S/N is the received-signal-to-noise ratio,

P is the peak transmitter power,

G is the antenna gain,

λ is the wavelength,

σ is the radar cross section,

R is the target range,

k is the Boltzmann constant,

T is the ambient temperature,

B is the receiver bandwidth,

L is the system loss factor, and

NF is the noise figure

A pulsed radar equipped with an automatic-gain-control (a-g-c) system can be calibrated so that the a-g-c voltage, V_{agc}, is a function of the signal-to-noise ratio. The radar equation then becomes simply $\sigma = CR^4 f(V_{agc})$ where the other parameters are lumped together as the constant C. C may be considered as a constant for the present work, since all the measurements were made relative to a metal reference sphere larger than any of the experimental spheres. Thus the measurement of radar cross section was simplified to a measurement of a-g-c voltage and range, with the radar automatically tracking the target. Avoidance, by this comparison method, of absolute measurement of the parameters contained in C was of practical importance in simplifying the experimental procedure. The size of the metal refer-

[3] L. N. Ridenour (editor), *Radar System Engineering*, Vol. 1, p. 21, McGraw-Hill Book Co., Inc., New York, 1947.

ence sphere is of minor importance if the reference-sphere cross section is taken to be on the theoretical curve. However, the larger the reference sphere, the closer it approaches the geometric cross section πr^2. The reference may therefore be considered to be beyond the resonance region, thus avoiding a possible bias in the reduced data.

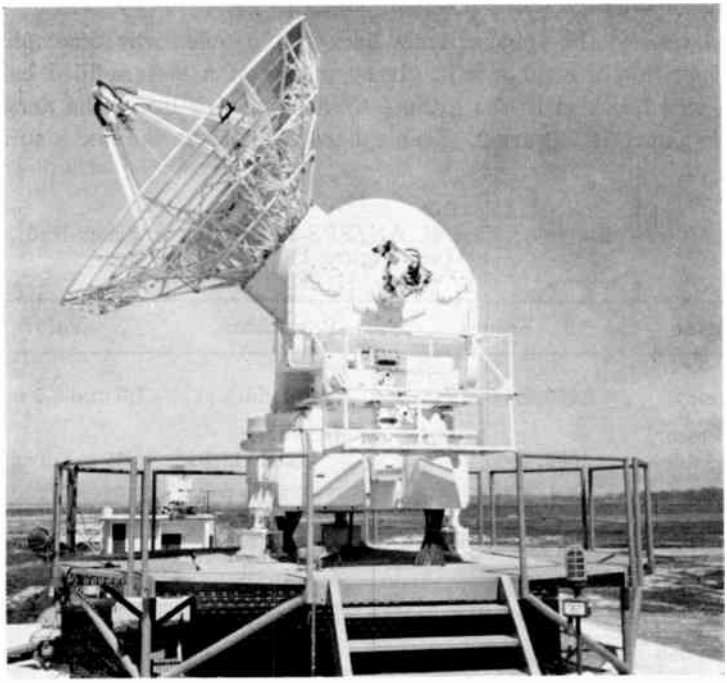

Fig. 1—AN/FPS-16 radar antenna pedestal.

Experimental Procedure

The radar used for these experiments is the AN/FPS-16 instrumentation radar, shown in Figure 1. It is a high-precision monopulse tracking radar originally designed for missile tracking. Its basic characteristics are given in Table II.

Since the radar cross section was computed from measured values of a-g-c voltage, it was necessary to obtain a calibration of a-g-c as a function of signal-to-noise ratio. Two methods were employed. First, the radar was locked on a signal from a horn located at the radar calibration tower and small increments of attenuation were introduced with a precision attenuator. An alternative and somewhat more convenient method is to feed the input signal directly to the waveguide

at the antenna. In the latter method, the signal generator and precision attenuator are located at the radar console. The radar was calibrated over a range of 80 decibels in signal-to-noise ratio, although only about 45 decibels was needed for the sphere measurements. Calibration was checked twice daily, both before and after each experiment, although this proved to be unnecessary as the calibration remained sufficiently stable even for much longer periods.

Isolation of the spheres from background noise was accomplished by suspending the spheres in air by means of a helium-filled balloon which was tethered to the ground by a nylon fish line. The arrangement is shown in Figure 2. Each sphere was tied to the line a suitable

Table II—Characteristics of AN/FPS-16 Instrumentation Radar (see Figure 1)

Parameter	Values	Parameter	Values
Frequency	5400 to 5900 mc	Bandwidth	1.6 and 8.0 mc
Peak Power (variable)	3000, 1000, 250 kw	Servo Bandwidth	0.25 to 6.0 cps
Pulse Width	0.25, 0.5, 1.0 μsec	Tracking Rate (Max.)	10,000 yds/sec
Repetition Rate	285 to 1707 pps	Tracking Rate (Max.)	700 mils/sec
Antenna Size	12 feet	Accuracy:	
Antenna Gain	44.5 db	range	5.0 yards
Polarization	vertical	angle	0.1 mil
Beamwidth	20 mils	Precision:	
Receiver Noise Figure	10 db	range	0.5 yard
		angle	0.02 mil

distance below the balloon so that there would be no significant return from the balloon. Furthermore, there were no significant returns from ground reflections or from the line. A six-inch-diameter metal sphere was used as a reference and left aloft continuously on a separate line. The reference sphere was located far enough away so that there would be no mutual interference with the measurements on the individual spheres. Measurements were made beyond the radar "near zone" at a range of about 1000 yards. At this short range, it was necessary to reduce the transmitter power through the use of a power programmer which is an integral part of the radar. In the operating region of

these experiments, this caused a small variation in the reference measurement. In order to reduce this source of error, data was taken on the reference sphere immediately before and after each individual sphere, and the average of these readings was used when reducing data. All data results were normalized to the same range.

The dielectric constant and loss tangent of the dielectric materials were measured using a method described by Roberts and von Hippel.[4]

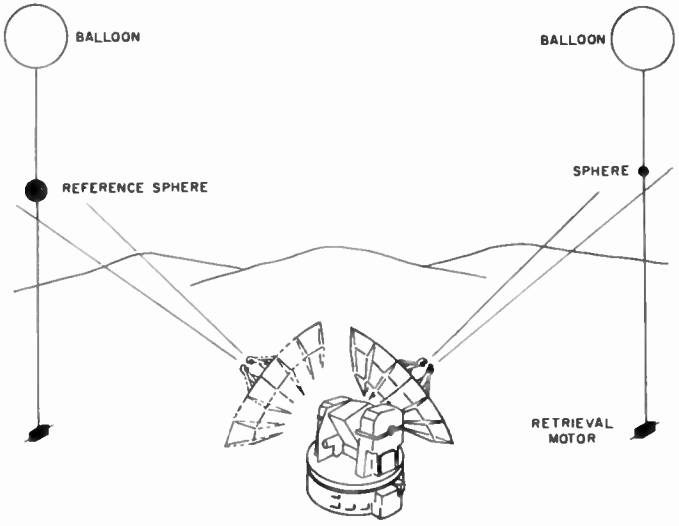

Fig. 2—Experimental arrangement.

RESULTS

Measurements were made in the size region $0.74 \leq 2\pi r/\lambda \leq 4.6$ on fifty-three aluminum, forty Teflon, twelve Lucite, and twelve Bakelite spheres. The radii of the spheres ranged from 0.25 inch to 1.5 inch in increments of 0.025 inch. The spheres were machined to a tolerance of .001 inch. The results for the aluminum spheres are shown in Figures 3, 4, and 5. Figures 3 and 4 are plots of cross section as a function of sphere radius at 5600 and 5800 megacycles, respectively. The data in Figure 3 are actually composites of five separate runs taken during the period December 1959 to October 1960. These data, together with two runs shown in Figure 4, comprise the composite

[4] S. Roberts and A. von Hippel, "A New Method for Measuring Dielectric Constant and Loss in the Range of Centimeter Waves," *Jour. Appl. Phys.*, Vol. 17, p. 610, July, 1946.

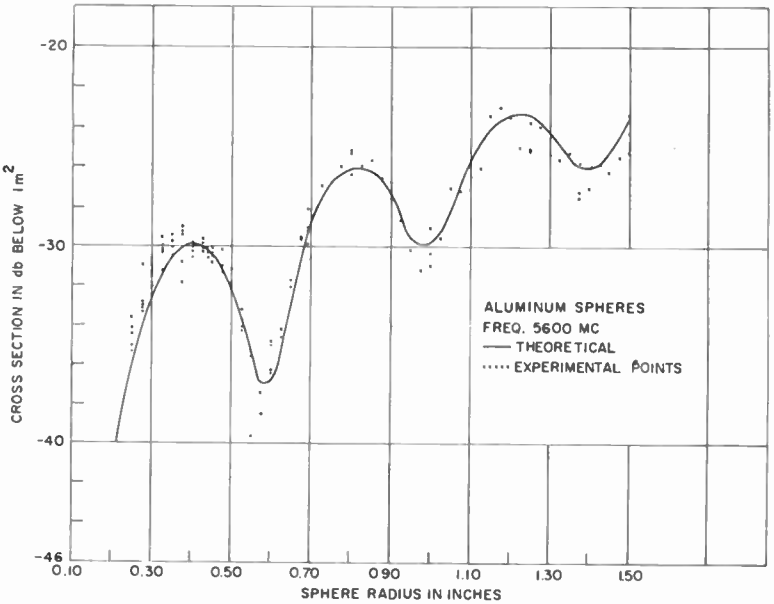

Fig. 3—Radar cross section, aluminum spheres. (Composite of five separate runs during the period Dec. '59 to Oct. '60.)

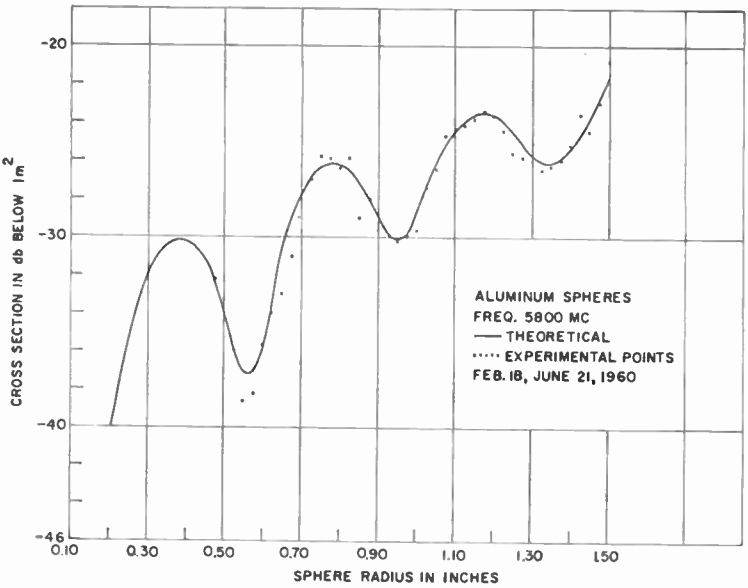

Fig. 4—Radar cross section, aluminum spheres.

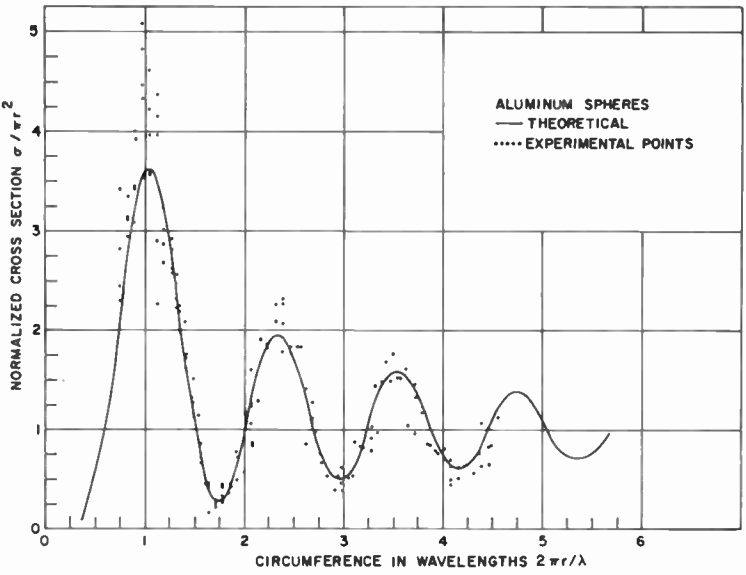

Fig. 5—Normalized radar cross section, aluminum spheres. (Composite of data in Figs. 3 and 4.)

Table III—Statistical Comparison of Experimental and Theoretical Cross-Section Results and Theoretical Normalized Cross-Section Results for Aluminum Spheres

Run	Mean Error (db)	Mean-Squared Error	R-M-S Error	Variance	Standard Deviation
Dec. 23, 1959	0.120	0.705	.840	.691	.831
Jan. 14, 1960	.113	.355	.595	.342	.585
Jan. 14, 1960	.161	.610	.780	.584	.764
Feb. 17, 1960	.077	.793	.891	.787	.887
Feb. 18, 1960	.148	.261	.511	.220	.469
June 21, 1960	.478	.121	1.10	.982	.991
Oct. 17, 1960	.022	1.80	1.34	1.80	1.34
(Normalized Results)					
Dec. 23, 1959	.130	.151	.388	.141	.376
Jan. 14, 1960	.006	.123	.351	.124	.351
Jan. 14, 1960	.096	.103	.321	.094	.306
Feb. 17, 1960	.138	.283	.532	.264	.514
Feb. 18, 1960	.009	.0196	.140	.0195	.140
June 21, 1960	.071	.062	.250	.057	.239
Oct. 17, 1960	.225	.244	.494	.193	.440

shown in Figure 5, which is a plot of normalized cross section $\sigma/\pi r^2$ as a function of size parameter $2\pi r/\lambda$. A statistical comparison of experimental and theoretical results for these seven runs is given in Table III, which shows the mean error, mean-squared error, r-m-s error, variance, and standard deviation. The mean and r-m-s errors were computed with respect to theoretical values (shown as a solid curve in the figures). The data on the Teflon, Lucite, and Bakelite spheres are given in Figures 6 through 13. The corresponding statistical summaries for these dielectric spheres is shown in Tables IV, V, and VI.

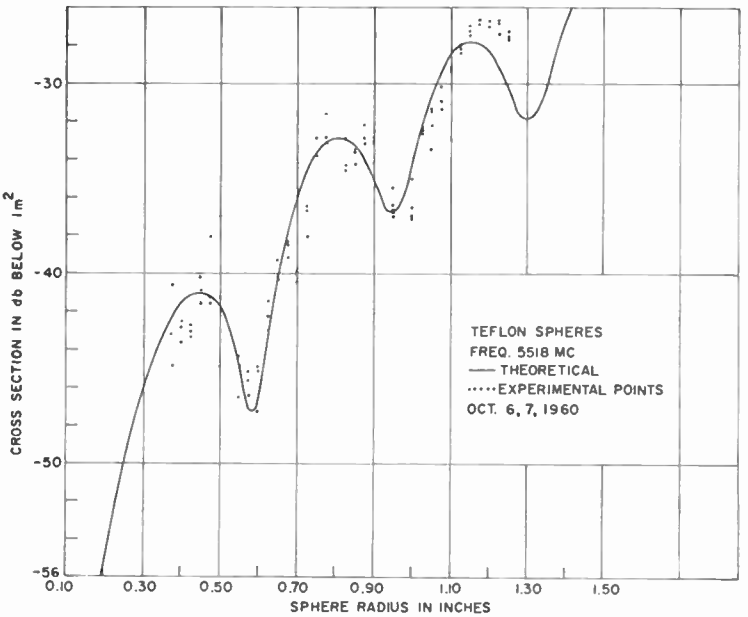

Fig. 6—Radar cross section, Teflon spheres.

A few remarks may be appropriate regarding the character of the data. The first impressions given by the normalized (linear) and unnormalized (log-versus-linear) plots are quite different. As one observes the measured points in the normalized figures, it is clear that the deviation of the measured points from the theoretical curve tends to increase as the size of the sphere decreases. This is to be expected since, for a given absolute error, the percentage error goes up as the size of the sphere goes down. This will explain what might otherwise be interpreted to be poor agreement, for example, near the first resonance peak in Figure 5.

Table IV—Statistical Comparison of Experimental and Theoretical Cross-Section Results and Theoretical Normalized Cross-Section Results for Teflon Spheres

Run	Mean Error (db)	Mean-Squared Error	R-M-S Error	Variance	Standard Deviation
Oct. 6, 7, 1960	.127	2.539	1.594	2.575	1.605
Oct. 17, 1960	.155	1.585	1.259	1.561	1.249
(Normalized Results)					
Oct. 6, 7, 1960	.0237	.0103	.102	.00985	.0993
Oct. 17, 1960	.012	.00284	.0533	.00269	.0519

In view of the possible sources of error and the generally recognized difficulty of employing pulse techniques for scattering-cross-section measurements under field conditions, the agreement between experiment and theory can be considered good. It should be noted that the radar used in the present investigation was designed for precision missile tracking and had not been intended for use in cross-section measurements. It is now evident that such a pulse radar can be used with good results in this application, and with still better results on larger size targets.

ACKNOWLEDGMENTS

The author is grateful to Professor J. L. Bohn for his guidance and encouragement of this work. Thanks are due the U.S. Army Signal Corps for making available the AN/FPS-16 radars; and the people who assisted in conducting the experiments.

Table V—Statistical Comparison of Experimental and Theoretical Cross-Section Results and Theoretical Normalized Cross-Section Results for Lucite Spheres

Run	Mean Error (db)	Mean-Squared Error	R-M-S Error	Variance	Standard Deviation
July 26, 1960	.892	3.941	1.985	3.146	1.774
(Normalized Results)					
July 26, 1960	.0209	.0179	.134	.0177	.133

Table VI—Statistical Comparison of Experimental and Theoretical Cross-Section Results and Theoretical Normalized Cross-Section Results for Bakelite Spheres

Run	Mean Error (db)	Mean-Squared Error	R-M-S Error	Variance	Standard Deviation
July 21, 26, 1960	2.23	16.987	4.123	11.999	3.464
(Normalized Results)					
July 21, 26, 1960	.115	.0258	.161	.0125	.112

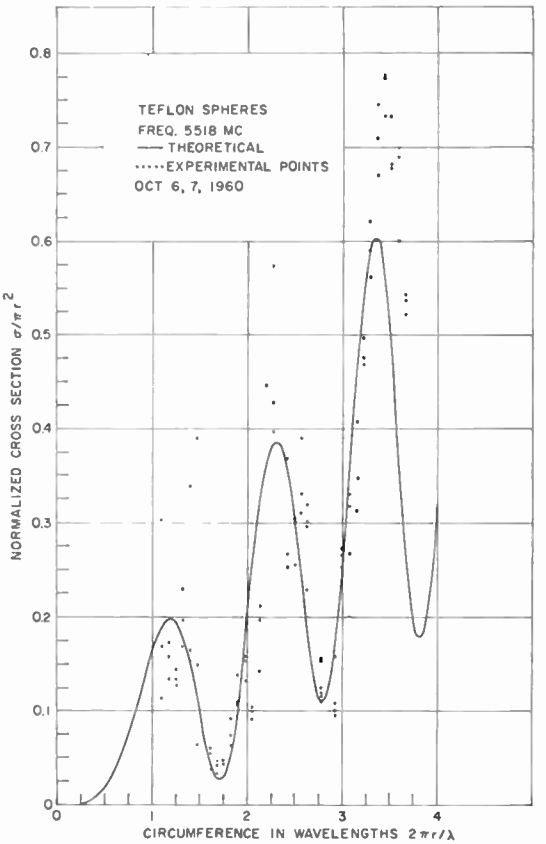

Fig. 7—Normalized radar cross section, Teflon spheres.

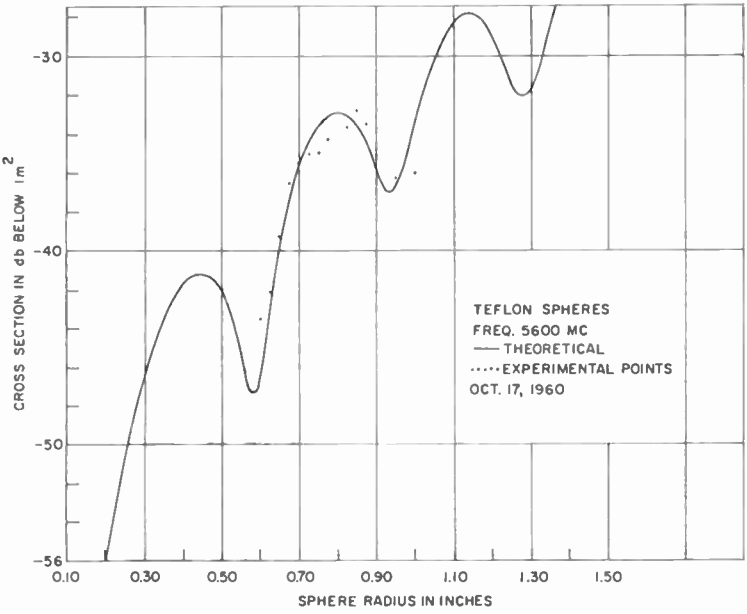

Fig. 8—Radar cross section, Teflon spheres.

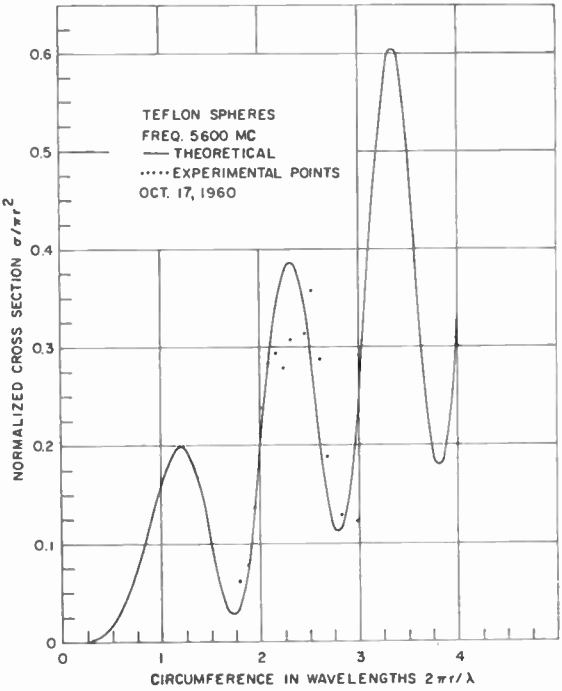

Fig. 9—Normalized radar cross section, Teflon spheres.

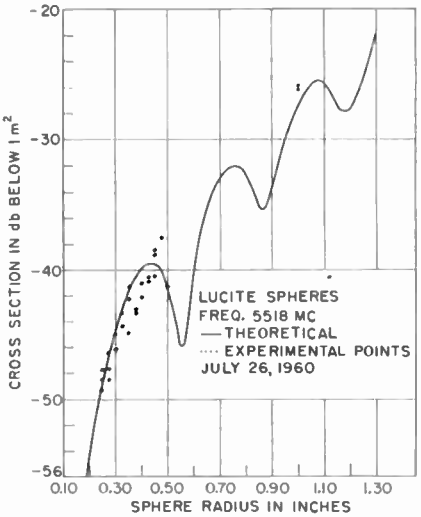

Fig. 10—Radar cross section, Lucite spheres.

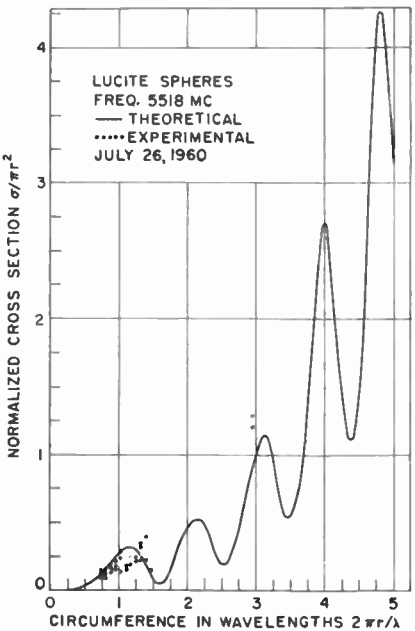

Fig. 11—Normalized radar cross section, Lucite spheres.

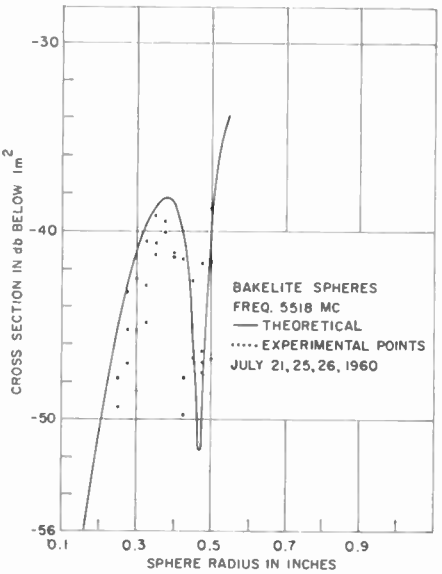

Fig. 12—Radar cross section, Bakelite spheres.

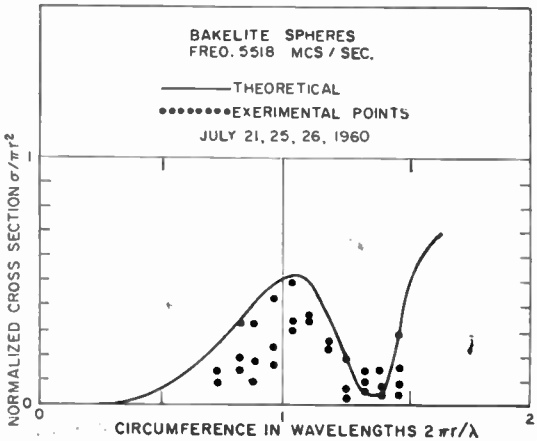

Fig. 13—Normalized radar cross section, Bakelite spheres.

A SPECTROPHOTOMETRIC INVESTIGATION OF DYE-SENSITIZED PHOTOCONDUCTIVE ZINC-OXIDE–RESIN LAYERS USED IN THE ELECTROFAX† PROCESS*

By

E. C. Giaimo

RCA Laboratories,
Princeton N. J.

Summary—Spectral characteristics are presented for several of the dyes currently being used as Electrofax sensitizers, namely, rose bengal, fluorescein, brilliant green, thioflavin, and acridine orange. Several dyed layers were studied; spectral characteristics were revealed which had n· been previously observed. These include ultraviolet sensitization at low concentrations, a shift of the visible response maxima with increasing · concentration, and modification of "effective dye concentration" with · posure. Irreversible effects due to past light history are also describe· These effects strongly influence the spectral response and processing tec· niques for Electrofax color reproduction.

The paper also describes an apparatus and a method for obtaining · spectral characteristics of zinc-oxide–resin layers. The method provides means for rapidly determining the photoconductivity of dye-sensit· layers as a function of light wavelength.

Introduction

SOME TIME AGO H. G. Greig demonstrated that sensitivity the zinc-oxide–resin layer used in Electrofax papers could b increased by increasing the spectral response of the materia through dye sensitization.[1] The spectral response of the undyed layer is very sharply peaked around 3850 Å. With the proper selection of organic dyes, however, the response can be made to extend through the visible spectrum. Furthermore, a large variety of spectral-respons characteristics can easily be achieved. Unlike the dyes used to sensitize ordinary photographic materials, the dyes used in the zinc-oxide layer need not be of high purity. For example, certain biological stains which are effective sensitizers for the Electrofax layers are unsuited for silver-halide layers.

† A trade mark of RCA.

* Manuscript received December 16, 1961.

[1] C. J. Young and H. G. Greig, "Electrofax—Direct Electrophotographic Printing on Paper," *RCA Review*, Vol. XV, No. 4, p. 475, Dec. 1954.

The ability to adjust and control the spectral response of the Electrofax layer through dye sensitization has greatly increased the uses of the process. For example, the spectral response can be made to match the spectral output of sources such as phosphors, which normally emit strongly at discrete wavelengths. Under such conditions, the dye-sensitized layers are far more sensitive than the undyed material. By combining several dyes having different absorption maxima, a panchromatic material can be produced. Such a material responds to all wavelengths in the visible spectrum. The panchromatic layer provides a means of producing colored Electrofax prints. Such a layer possesses color-printing properties not possessed by other known color-reproducing media.

This paper describes a method for obtaining the photoconductive response of the dyed layers as a function of wavelength. The method consists of measuring the photoconductivity of a small portion of the layer which lies between two metallic electrodes which are pressed into the surface. Continuous response measurements between 3700 and 7000 Å may be rapidly obtained. Using the data obtained by this method, good correlation has been obtained between the predicted behavior and actual print tests with corona charging. However, certain characteristics have been discovered which have not heretofore been observed in the print tests.

Experimental Apparatus

The essential components of the experimental apparatus, shown in figures 1 and 2, are a specimen holder, a direct-current source, a motor-driven monochromator, a cathode-ray-tube display, and a camera for photographing the trace. When the specimen is subjected to a light source of continuously varying wavelength, a plot of photocurrent versus wavelength is displayed on the oscilloscope as a continuous curve.

The specimen holder is composed of two knife-edge electrodes carried on insulating Lucite* supports. The mechanical arrangement is such that the electrodes can be adjusted independently to obtain parallel alignment and equal contact of each to the surface of the sample under observation. The method for accomplishing alignment can be seen in Figure 1. Each electrode is inclined approximately 10° to the normal to form a Vee. Light can be directed to fill the unobstructed inter-electrode area. The electrodes press with a constant force against a rigid platen upon which the sample sheet is laid. A force of approximately 10 pounds was used for the tests described here. The electrodes are 1 centimeter long and spaced ¼ millimeter apart

* Trade mark.

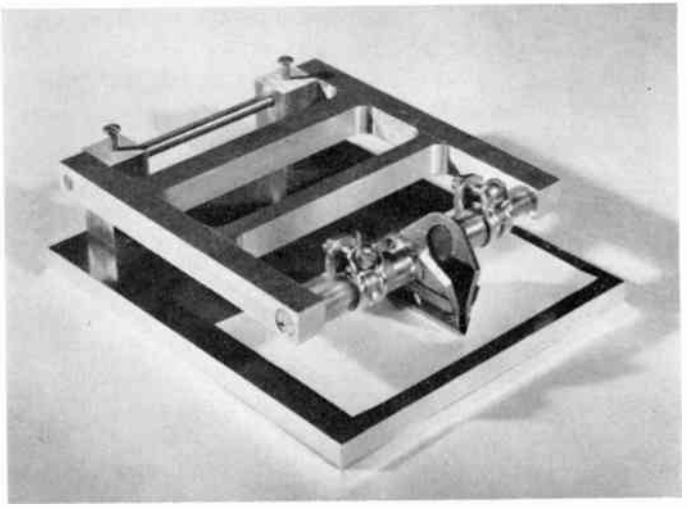

Fig. 1—Specimen holder.

at the surface of the layer. These values were maintained for all the measurements.

Light of variable wavelength directed between the electrodes is obtained from a 250-millimeter-focal-length grating monochromator having a quartz lens system. The light input to the monochromator is obtained from a tungsten lamp heated to approximately 3000°K which provides a continuous spectrum over the region of interest. The entrance and exit slit widths of the instrument are 5 millimeters.

The monochromator is driven by a synchronous motor through a 3-speed mechanical transmission (shown in Figure 2). Scanning rates

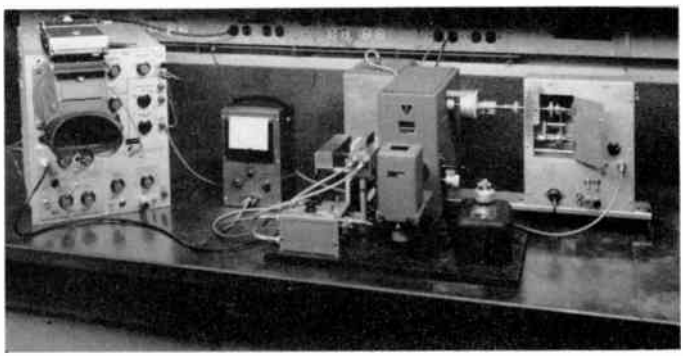

Fig. 2—Experimental setup.

of 300, 1000, and 3000 Å per minute are available. A scanning speed of 1000 Å per minute was used for all measurements. Tests indicated that some distortion in the spectral curves resulted at high scanning rates due to lags in the photocurrent. At the 300 and 1000 Å per minute rates, the changes in the response curves were negligible.

The sweep voltage proportional to wavelength is obtained from a bridge circuit. One leg of the bridge contains a manually operated multiturn potentiometer for zero setting; the other leg contains a multiturn potentiometer which is mechanically coupled to the motor drive system. The unbalance of the bridge provides a voltage proportional to wavelength. This voltage is connected to the horizontal amplifier of an oscilloscope. The horizontal input gain of the oscilloscope and the magnitude of the voltage obtained from the sweep generator provide a means for adjusting the amplitude of a given spectral region on the display.

Damage to the sweep-generator potentiometers and the monochromator is prevented by limit switches. Automatic repeat scanning is also obtainable for examining the effects of past light history and distortion in the spectral curves due to scanning direction.

The electrodes, which press against the specimen, are connected to a potential divider through a one-megohm series resistor. The potential divider provides a variable d-c voltage from a series of batteries. The voltage developed across the series resistor is proportional to photocurrent, and is connected to the vertical d-c input of the oscilloscope. The current sensitivity of the system gives a lower limit on the photocurrent of the order of 5×10^{-8} ampere. The potential across the electrodes was 200 volts for all the data taken. A shielded battery enclosure and complete shielding of all leads is used throughout to prevent stray noise from obliterating the signal at low levels. A schematic of the circuit used is shown in Figure 3.

PROCEDURE

Preliminary observations indicated that if the scanning is done from the ultraviolet toward the red, part of the dye response cannot be observed due to the slow decay of the photocurrent that results when the scan passes through the 3850 Å peak. The scanning direction used for all samples, therefore, was from the red toward the ultraviolet.

For comparison with dye-sensitized layers, an undyed layer was measured. The results are shown in Figure 4. No correction has been made for the monochromator tungsten lamp emission at 3000°K. The

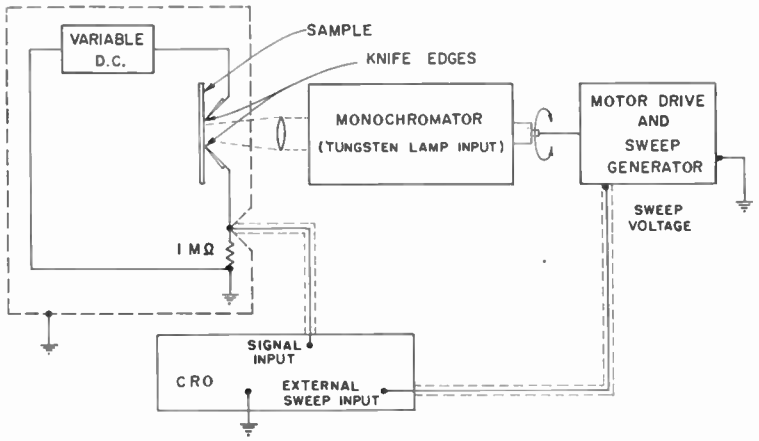

Fig. 3—Setup of experimental apparatus.

curve in Figure 4 indicates that the absorption peak is steeper on its long-wavelength side. In order to determine whether scanning was responsible for the asymmetry of the curve, point-by-point data was obtained by exposure at various light wavelengths for fixed time intervals. Between exposures, the photocurrent was allowed to decay

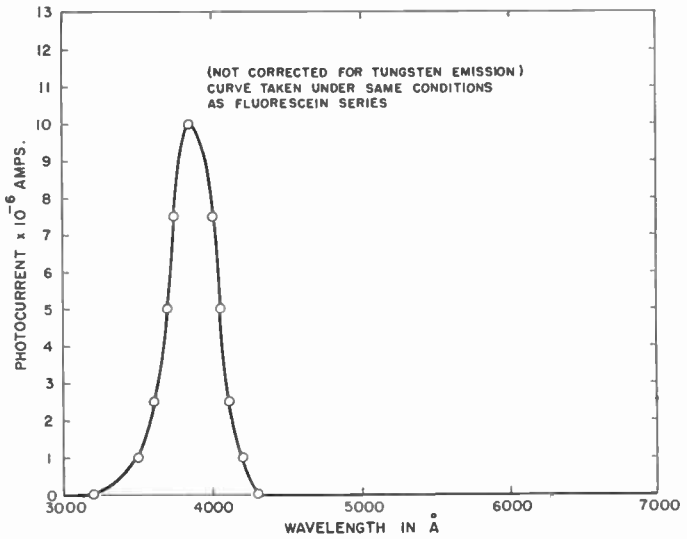

Fig. 4—Standard Electrofax zinc oxide-resin layer with no dye sensitization (not corrected for tungsten emission curve taken under same conditions as fluorescein series).

to the lower limit of sensitivity of the system before the next exposure was made. Essentially the same curve was obtained as with scanning.

During the measurements on the undyed layer, it was found that several exposures caused the maximum photocurrent to decrease. A series of measurements was made by repeatedly scanning the sample between 3000 and 5000 Å. The curve of Figure 5 shows the decrease in maximum photocurrent at 3850 Å with time. The sensitivity could be restored by corona charging of the sample or storage in the dark for several hours.

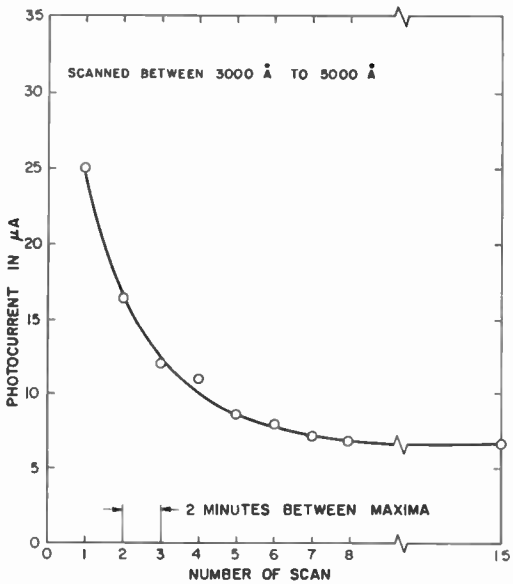

Fig. 5—Loss of photoconductivity of undyed layer with repeated exposure (scanned between 3000 and 5000 Å).

Because of the above effects, all samples tested were stored in the dark immediately after coating. Samples that had been exposed to light were not tested until they had been in the dark for at least two days.

Results

As stated, the change in photoconductivity with exposure at the absorption maximum is only temporary for the undyed layer. On the other hand, the dye-sensitized layers showed a permanent change in photosensitivity with exposure. A change in sensitivity is normally accompanied by a loss in color. This has been observed with rose

bengal and fluorescein dye-sensitized layers. Samples sensitized with these materials are bleached almost white with extended exposure to daylight. The heating during the fusing step of the Electrofax printing process also causes a loss of color with an accompanying drop in sensitivity especially at low dye concentrations.

The loss in sensitivity is an integral effect; i.e., the total area under the photocurrent versus wavelength curve can be changed by exposure to light of selected wavelengths. For instance, it was observed that the ultraviolet maximum could be modified by exposing a rose bengal layer or a fluorescein layer at the visible maxima, 5500 Å and 5100 Å, respectively. In each case, the ultraviolet peak increased. This effect might be explained on the basis of a change in the "effective dye concentration" with exposure. In effect, the exposure may lower the dye concentration by a photodestructive process and the ultraviolet response increases as it does when one lowers the dye concentration from a high to low level. It is possible then to adjust both the spectral response and sensitivity of certain dyed layers by exposure to the proper radiation. It must also be pointed out that care should be exercised during spectral measurements since the shape of the response curve can be changed dramatically by improper handling.

The samples tested were stored in the dark immediately after coating. Care was taken to prevent unnecessary exposure prior to testing. In addition, a new area on the sheet was selected for each run. The curves shown are representative of the average in each case.

H. G. Greig, in his experiments with dye sensitization, has shown that there is an optimum dye concentration at which maximum sensitivity is obtained. In order to determine the effect of various dye concentrations more precisely, a dye-concentration series was run for the several dyes currently being used.

Several striking effects are observed. First, at very low dye concentrations it appears that the ultraviolet response of the layer is increased as compared to undyed material. The effect can be seen by comparing the .01 curve of the fluorescein series, Figure 6, with the curve in Figure 4.

Second, as the dye concentration is increased beyond a critical value, the 3850 Å peak begins to decrease while the peak around 5100 Å continues to increase. The maximum value of the 3850 Å peak occurs at a lower dye concentration (between 0 and .03) than the 5100 Å peak (between .01 and .05).

Third, as the dye concentration is increased further, as shown in Figure 7, both the 3850 Å and 5100 Å peaks decrease. At 0.3 gram of dye per 120 grams zinc oxide, the response has dropped in the ultra-

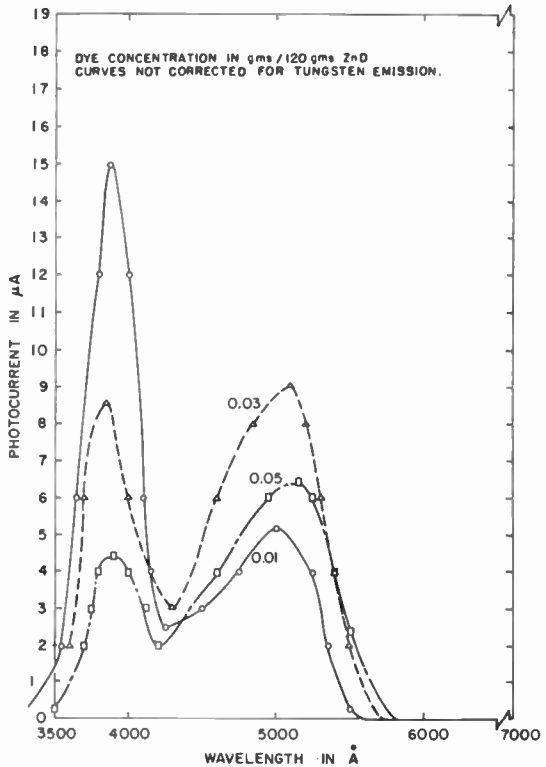

Fig. 6—Response of dye sensitized Electrofax layers with dye concentrations of 0.01, 0.03, and 0.05 grams of fluorescein per 120 grams of ZnO.

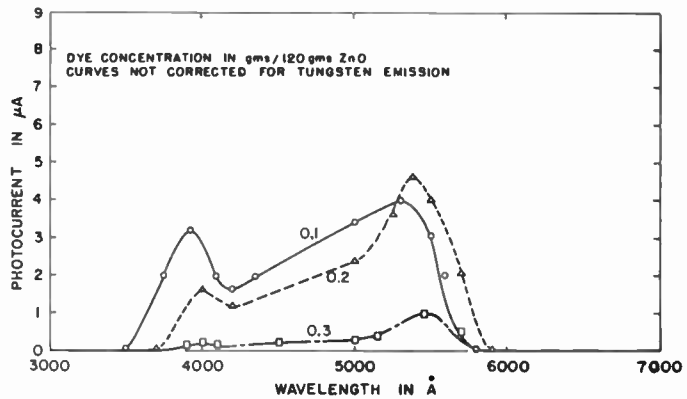

Fig. 7—Response of dye sensitized Electrofax layers with dye concentrations of 0.1, 0.2, and 0.3 grams of fluorescein per 120 grams of ZnO.

violet to about 1/100 of the value it had at .01. At 5000 Å on the other hand it is about 1/20 of the value it had at .01. In the dye concentration range between .03 and .01, the area under the curve appears to remain fairly constant. The loss in sensitivity at 3850 Å is accompanied by a gain around the 5000 Å peak.

Another interesting characteristic can be seen in Figures 6 and 7;

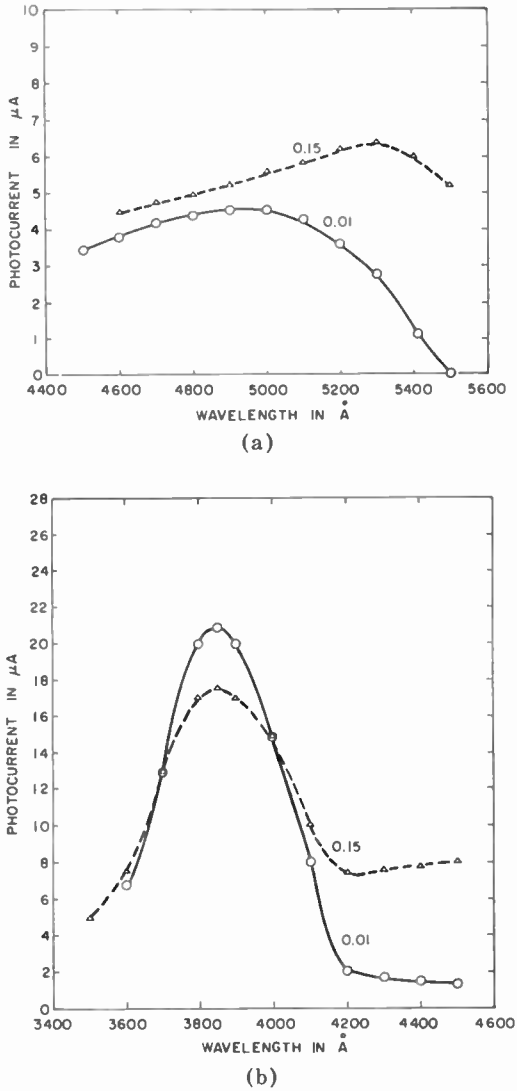

Fig. 8—Effect of increase in fluorescein dye concentration on peak response (a) in visible region and (b) in ultraviolet region.

as the dye concentration is increased from .01 to 0.15 gram per 120 grams of ZnO, the spectral response in the visible shifts toward the red. In order to observe this effect in more detail, the resolution of the system was increased to obtain the results plotted in Figure 8a. The "red shift" in the upper curve is shown to be about 300 Å as the dye concentration is increased from .01 to 0.15. There appears to be no accompanying shift in the ultraviolet peak (3850 Å) over the same concentration range, Figure 8b. By comparing the data in Figures 6 and 7, a 500 Å "red shift" for the fluorescein-dyed samples is observed over the concentration range .01 to 0.3. Figure 9 shows a plot of the

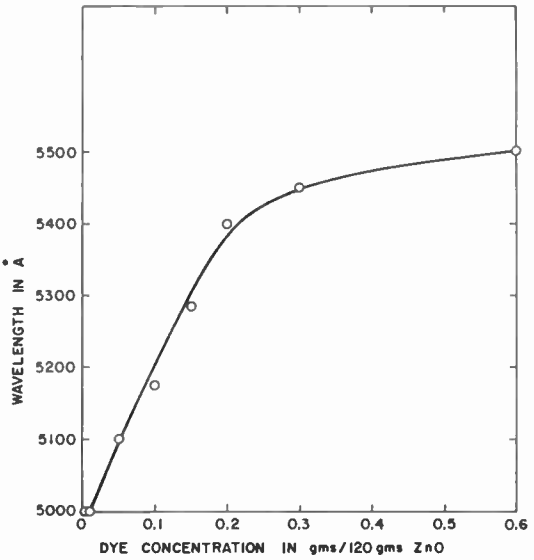

Fig. 9—Shift of response maximum in visible region with increase in fluorescein dye concentration.

red shift over the concentration range 0 to 0.6. Figure 10 shows the dye concentrations versus photoresponse at three different wavelengths. The curves clearly demonstrate that to obtain a maximum response for monochromatic light of a given wavelength, a specific dye concentration is required.

A similar dye concentration series was taken of rose bengal dyed layers. As in the fluorescein-sample tests, both the 3850 Å and visible peaks reach maximum values at different dye concentrations. The curves are shown in Figures 11 and 12.

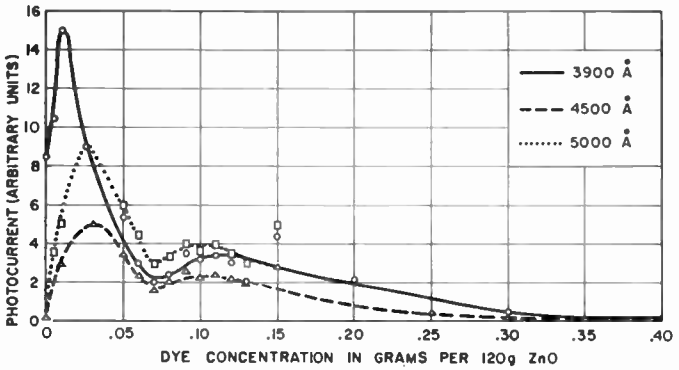

Fig. 10—Fluorescein dye concentration versus photoconductivity at three different wavelengths (uncorrected for tungsten light).

The dye concentrations which yield the maximum area under the curves for both fluorescein and rose bengal correlate very well with the concentrations Greig has found which yield maximum sensitivity to tungsten light during Electrofax print tests.

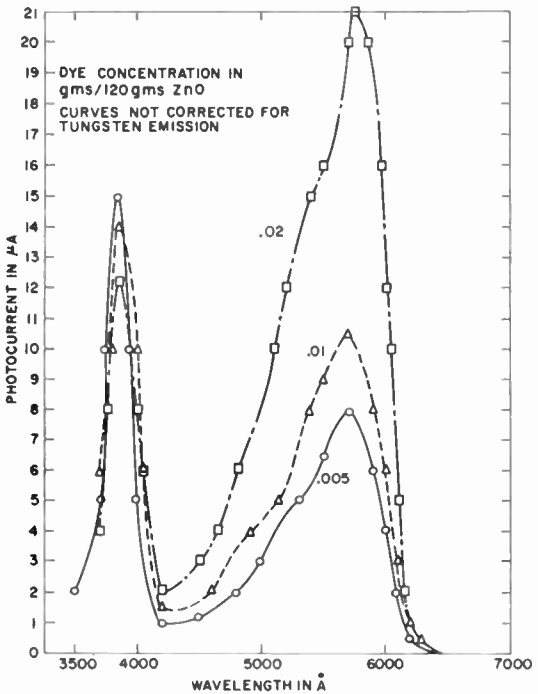

Fig. 11—Response of rose bengal dye sensitized Electrofax layers for dye concentrations of 0.005, 0.01, and 0.02 grams per 120 grams ZnO.

Several other dyes were also investigated. These showed the same general trends as fluorescein. The curves of thioflavin, acradine orange, and brilliant green are shown in Figures 13, 14, and 15, respectively. These three dyes show the loss in ultraviolet sensitivity with increasing dye concentration. The series for each was not carried far enough to determine whether the visible response peaks go through a maximum value when various dye concentrations are used. The "red shift" appears to be present over the limited range studied for each.

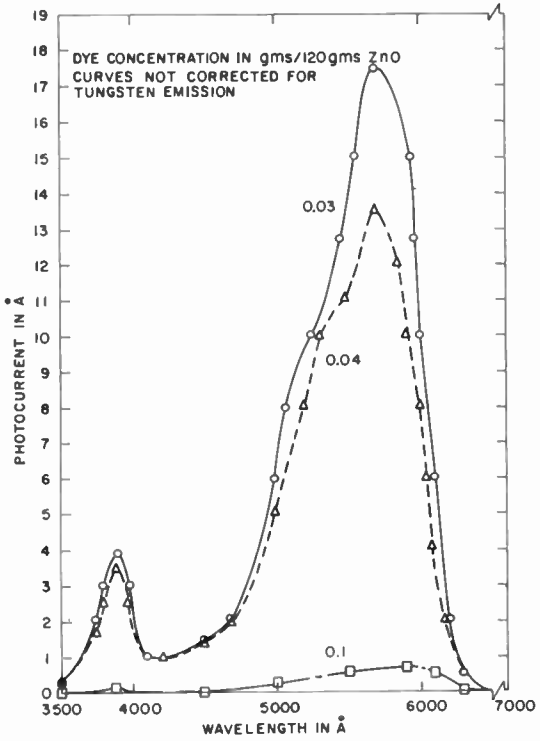

Fig. 12—Response of rose bengal dye sensitized Electrofax layers for dye concentrations of 0.03, 0.04, and 0.1 grams per 120 grams ZnO.

The combination of several dyes yields a layer which is sensitive over the spectrum. Such a layer might be called panchromatic. The photoconductive response curve of a layer containing fluorescein, rose bengal, and brilliant green is shown in Figure 16. This layer is suitable for making Electrofax color reproductions using various techniques currently under investigation.

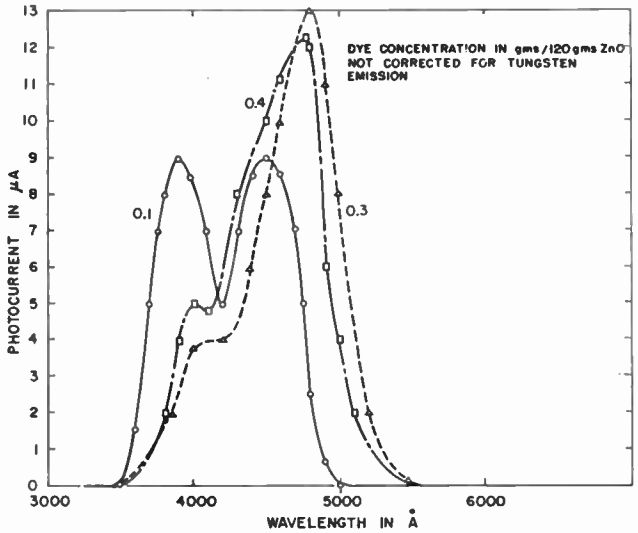

Fig. 13—Response of thioflavine dye sensitized layers for various dye concentrations in grams per 120 grams ZnO.

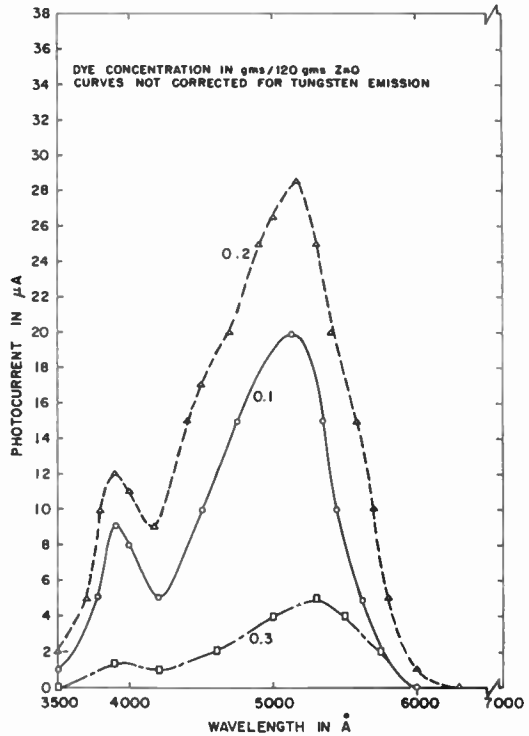

Fig. 14—Response of acridine orange dye sensitized Electrofax layers for various dye concentrations in grams per 120 grams ZnO.

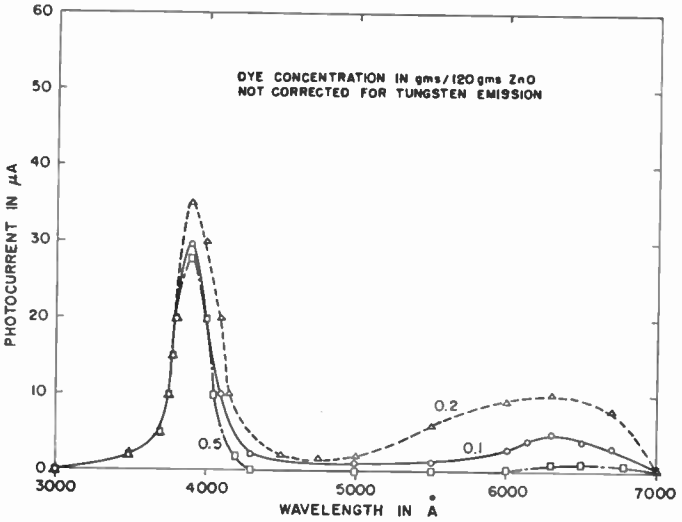

Fig. 15—Response of brilliant green CI662 dye sensitized Electrofax layers for various dye concentrations in grams per 120 grams ZnO.

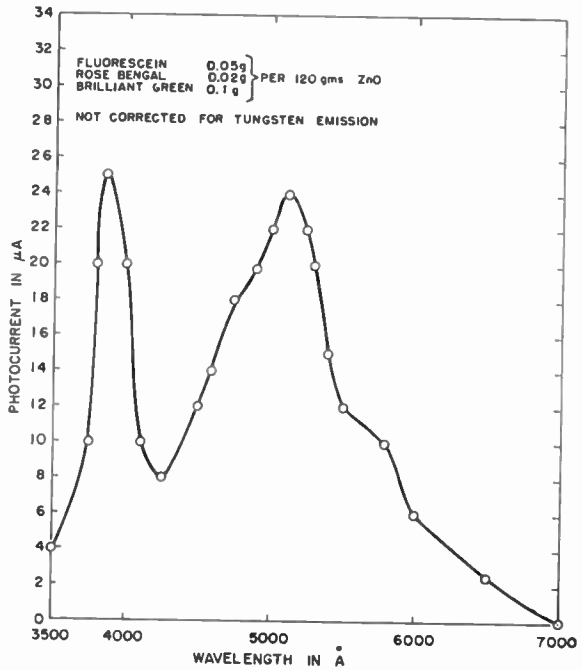

Fig. 16—Response of panchromatic dye sensitized Electrofax layers with the following concentration per 120 grams ZnO: fluorescein, 0.05 grams; rose bengal, 0.02 grams; brilliant green, 0.1 gram.

Conclusion and Summary

There is a strong temptation to compare the relative sensitizing action of the various dyes studied; however, it must be pointed out that the relative dye strengths are not known. One can make comparisons of the sensitizing actions, but they will only hold for the particular dye batches used. In order to determine the relative effects of the various dyes, absolute quantities based on molecular weights and dye structure would have to be used. A detailed quantitative study of the relative sensitization of dyes by various classes and types is needed to obtain a better understanding of the sensitization mechanism and for the selection of dyes having the maximum sensitizing action for a given spectral response.

Several conclusions can be drawn from the data and observations made, and certain general properties of the dye sensitized layers can be enumerated.

1. The zinc-oxide absorption maximum can be enhanced or suppressed by the proper choice of dye and dye concentration. For example, as the concentration of fluorescein is raised, the 3850 Å peak can be made to pass through a maximum. The depression of the 3850 Å response with increasing dye concentration above a critical value is evident for all the dyes investigated.

2. The maximum 3850 Å response is at a lower dye concentration than the dye concentration needed to obtain a maximum at the dye's absorption peak.

3. The over-all spectral sensitivity to a continuous spectral source can be maximized by the proper dye concentration. This maximum is fairly broad in some cases. The area under the spectral curve changes slowly even though the over-all shape has changed dramatically as shown, for example, in Figure 6.

4. Irreversible changes occur in the spectral characteristics with exposure of the dyed layers. It is possible to change the spectral sensitivity of the layer permanently with exposure and thereby modify the "effective dye concentration." The over-all sensitivity to a source producing a continuous spectral output may either increase or decrease, depending on the initial dye concentration. Exposure at one wavelength will affect the sensitivity in other regions of the spectrum. For example, exposure of the fluorescein or rose bengal of high dye concentration for a given time at the visible maximum will increase the sensitivity at 3850 Å.

6. As the dye concentration is increased, there is a shift in the visible maximum toward the red end of the spectrum, but no shift can be seen around 3850 Å.

7. Past light history effects provide means for controlling the sensitivity and spectral response of the dyed layers. This is an important property which can be used to advantage for color reproduction.

8. When taking sensitometric and spectrometric data, past light history must be taken into account.

9. Certain dyes are more effective sensitizers than others.

ACKNOWLEDGMENT

The author wishes to thank H. G. Greig for providing the various dyed samples needed for this study and for his stimulating discussions during the investigation.

BASE-LAYER DESIGN FOR HIGH-FREQUENCY TRANSISTORS*

By

H. S. Veloric,† C. Fuselier,# and D. Rauscher†

Summary—This paper discusses some of the parameters which must be evaluated in the design of a high-frequency, double-diffused transistor. A Gaussian distribution, a complementary-error-function distribution, and a Gaussian impurity distribution modified by outdiffusion are considered for use in a base layer. Total impurity concentrations are calculated for several important cases. The "reach-through" voltage is calculated for a constant base width as a function of distribution and collector penetration.

For the distributions considered, it is shown that in order to maintain constant doping under the emitter as the collector penetration is increased, it is necessary to increase the base width. The maximum possible current gain is also presented as a function of the diffusion length of the minority carriers in the emitter for several cases of collector penetration and surface concentration.

Because the number of impurities and penetration can be predicted, boron deposition and redistribution is shown to be a suitable technique for the introduction of carefully controlled impurity layers in silicon. Except for the ratio of dielectric constants, the calculations involving reach-through voltage are applicable for all materials.

Comparison of Impurity Distributions

THE DESIGN OF TRANSISTORS, particularly in the case of silicon, has been strongly influenced by double-diffusion techniques. Unfortunately, the forms of the diffusion equation solutions do not lend themselves to easily derivable answers to many questions arising in practical situations. It is necessary to fix certain parameters and vary others so that their effects on device performance can be evaluated. In this paper the evaluated parameters are: (1) reach-through voltage, (2) doping under the emitter, and (3) maximum current gain. The diffusion parameters held constant are: (1) emitter surface concentration, (2) collector doping, and (3) base width. The design variables considered are: (1) type of impurity distribution in the base, (2) maximum concentration in the base, and

* Manuscript received 18 January 1962.

† RCA Semiconductor and Materials Division, Somerville, N. J.

RCA Electron Tube Division, Princeton, N. J.; formerly, RCA Semiconductor and Materials Division, Somerville, N. J.

(3) collector penetration. In addition, the base width is evaluated as a function of collector penetration for a constant base doping.

The solution to the diffusion equation depends upon the boundary conditions imposed. This solution determines the distribution of added impurities.[1] One easily obtained boundary condition is a surface concentration which is independent of time. This condition may be obtained by maintaining the maximum solid solubility of the diffusant at the surface. Surface concentrations less than the maximum solid solubility can be obtained in flow systems[2] or by use of appropriately doped source powders.[3] For the case of constant surface concentration, the concentration $C(x)$ as a function of distance is given by

$$C(x) = C_0 \operatorname{erfc} \frac{x}{2\sqrt{Dt}}, \tag{1}$$

where C_0 is the surface concentration, D is the diffusion constant, and t is the diffusion time.

Another boundary condition which is attainable is a planar source having an initial sheet density $\bar{N}_0$ in the solid at the surface. This boundary condition is approximately realized by diffusing a thin layer and redistributing the impurities in a subsequent diffusion. The solution of the diffusion equation for this case is the following Gaussian distribution:

$$C(x) = \frac{\bar{N}_0}{\sqrt{\pi Dt}} \exp\left(-\frac{x^2}{4Dt}\right). \tag{2}$$

The Gaussian distribution is frequently changed by outdiffusion of the diffusant during the redistribution step. The solution of the diffusion equation for this important case, which has been previously considered in the literature,[4] is given by

$$C(x) = \frac{\bar{N}_0}{\sqrt{\pi Dt}} \exp(-y^2)\,[1 - \sqrt{\pi}\, z \exp(y+z)^2 \operatorname{erfc}(y+z)].$$

---

[1] F. M. Smits, "Formation of Junction Structures by Solid-State Diffusion," *Proc. I.R.E.*, Vol. 46, p. 1049, June, 1958.

[2] C. J. Frosch, "Silicon Diffusion Technology," *Transistor Technology*, D. Van Nostrand Co., Inc., N. Y., N. Y., Vol. 3, p. 90, 1958.

[3] H. S. Veloric and W. Greig, "Evaluation and Control of Diffused Impurity Layers in Germanium," *RCA Rev.*, Vol. 21, p. 437, Sept., 1960.

[4] F. M. Smits and R. C. Miller, "Rate Limitation at the Surface for Impurity Diffusion in Semiconductors," *Phys. Rev.*, Vol. 104, p. 1242, Dec. 1, 1956.

This solution has the same form as the Gaussian, except for a multiplying term in the bracket where $z = K\sqrt{Dt}/D$, $y = x/(2\sqrt{Dt})$, and K is a constant which specifies the rate limiting properties of the surface. As z approaches 0, the expression within the brackets approaches unity. The Gaussian distribution itself is not considered further, since redistribution without out-diffusion has not been observed in silicon.

A comparison of these impurity distributions is useful for tran-

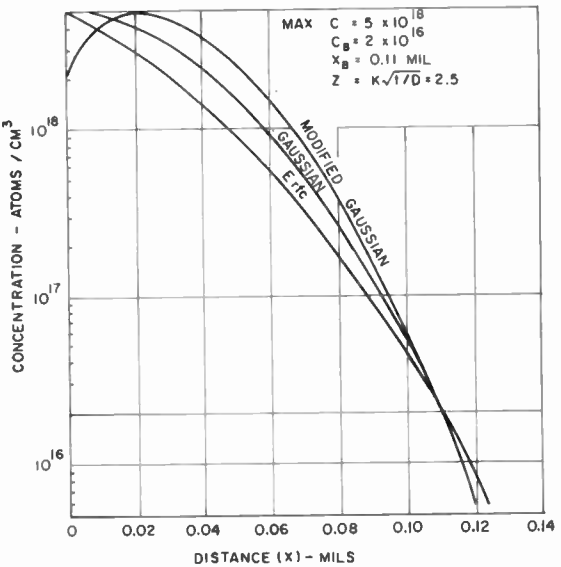

Fig. 1—Comparison between erfc, Gaussian, and out-diffused Gaussian distributions.

sistor base-layer design. Figure 1 shows concentration as a function of distance for the three impurity distributions. For this comparison, the maximum concentration is 5×10^{18} atoms per cubic centimeter; at a common point 0.11 mil from the surface, the concentration is 2×10^{16} atoms per cubic centimeter. A value of $z = 2.5$ is used as a typical value for the out-diffused Gaussian distribution.

The two particular cases of importance considered in this paper are: (1) the complementary-error function which is the case for the emitter or base when the surface concentration is independent of time, (2) the modified Gaussian distribution which is realized for the case of deposition and subsequent redistribution of impurities.

Typical Transistor Impurity Distributions

The use of the diffused-emitter, diffused-base approach to transistor design introduces several design parameters which are not available in single-diffused or alloy structures. Tanenbaum[5] has considered the general case for a double-diffused transistor with a complementary-error-function emitter and base distribution. He utilized a computer to solve the transcendental equations which define the net impurity distributions.

In the present paper, most of the parameters are evaluated by graphical solution of the net impurity profile for specific values of the diffusion variables. Some of the more important variables are the surface concentration of the diffusants, the collector penetration, the base width, the doping in the collector region, and the distribution of added impurities.

General design considerations determine the values for some of the process parameters. The surface concentration[6] of a phosphorus emitter is of the order of 2×10^{20} atoms per cubic centimeter. A background level of 2×10^{16} atoms per cubic centimeter is selected. A base width of 3×10^{-2} mil is used as an approximation to the optimum base width. The three diffusion variables which can then be varied are the surface concentration of the base, the type of impurity distribution in the base, and the base–collector crossover point.

Figure 2 shows the added impurities as a function of distance for a complementary-error-function distribution in the emitter and base layers. The surface concentration of the base is selected as 5×10^{18} atoms per cubic centimeter and the collector junction is chosen at 0.07 mil. The triangular area defined by the emitter, base, and collector distributions roughly corresponds to the net concentration between the emitter and collector. The curves of Figure 2 are the first step in the graphical evaluation of the net impurity distribution.

Figure 3 shows the added impurities as a function of distance for a complementary-error-function emitter distribution and an out-diffused Gaussian base distribution. The maximum concentration in the base distribution is selected as 5×10^{18} atoms per cubic centimeter. The parameter z, as defined by Smits and Miller,[4] is chosen to be 2.5. The principal difference between this case and that of Figure 2 is that the maximum concentration does not occur at the surface.

---

[5] M. Tanenbaum and D. Thomas, "Diffused Emitter and Base Transistors," *Bell Syst. Tech. Jour.*, Vol. 35, p. 1, Jan., 1956.

[6] G. Backenstoss, "Evaluation of Surface Concentration in Silicon," *Bell Syst. Tech. Jour.*, Vol. 37, p. 699, May, 1958.

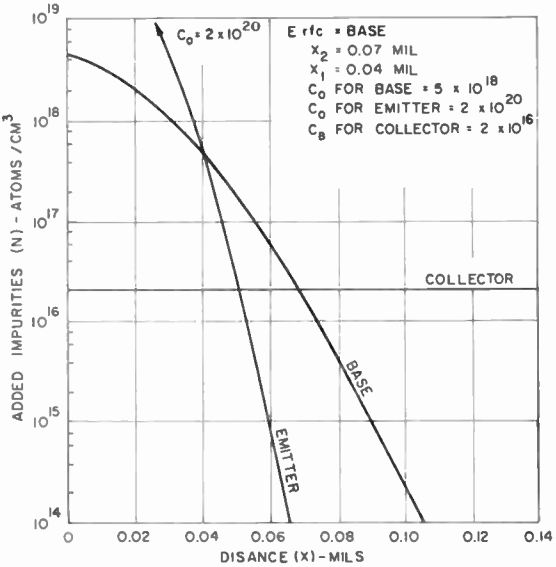

Fig. 2—Added impurities as a function of distance for an erfc emitter and erfc base distribution.

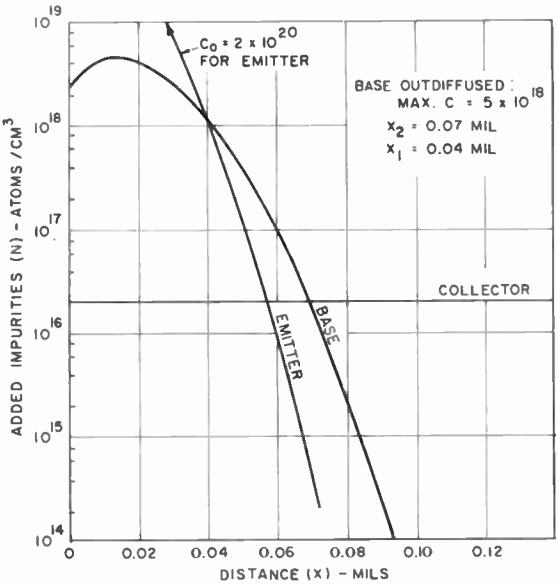

Fig. 3—The added impurities as a function of distance for an erfc emitter distribution and an out-diffused Gaussian base distribution.

It is possible to estimate the net impurity concentration at any point from the curves of Figures 2 and 3. Figure 4 shows the net impurity distribution for a complementary-error-function emitter and base distribution, as calculated from Figure 2. The emitter and collector junctions do not correspond exactly to the emitter and collector crossover points. The base width will be smaller than the difference

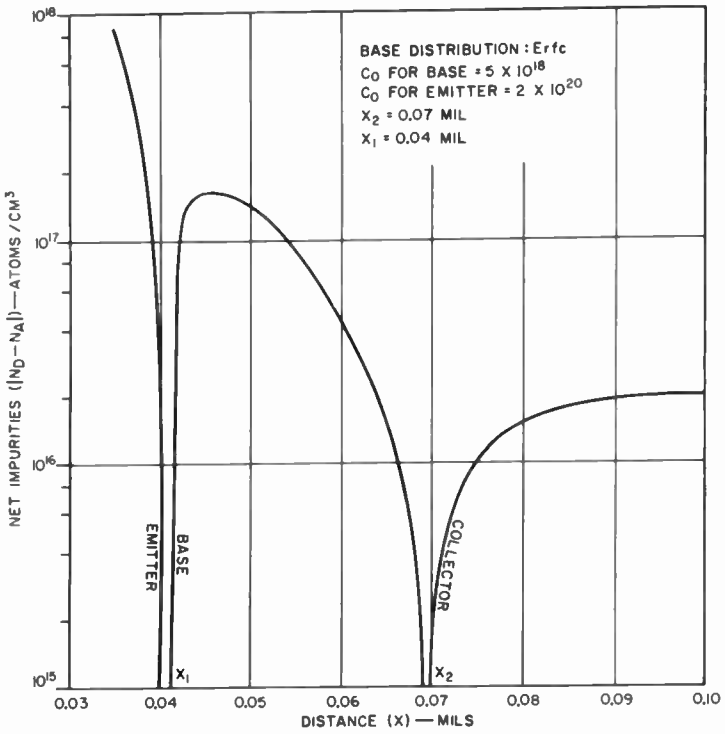

Fig. 4—The net impurity concentration as a function of distance for an erfc emitter and erfc base distribution.

between the two crossover points; this effect is more pronounced as the impurity gradient decreases. For the selected diffusion parameters, the maximum doping in the base is greater than that in the collector.

The net impurity concentration $|N_D - N_A|$ for an erfc base, erfc emitter structure is given by

$$N_D - N_A = C_1 \operatorname{erfc} \frac{x}{2\sqrt{D_1 t_1}} - C_2 \operatorname{erfc} \frac{x}{2\sqrt{D_2 t_2}} + C_3, \qquad (4)$$

where C_1 and C_2 are the surface concentrations of the emitter and base diffusants, respectively, and C_3 is the impurity level in the bulk material. The specific equation for Figure 4 can then be written as follows:

$$|N_D - N_A| = 2 \times 10^{20} \operatorname{erfc} \frac{x}{1.87 \times 10^{-2}} - 5 \times 10^{18} \operatorname{erfc} \frac{x}{3.44 \times 10^{-2}} + 2 \times 10^{16}. \quad (5)$$

This equation has two roots where $N_D - N_A = 0$, namely the emitter and collector junctions. A similar analytical expression for the outdiffused case would be considerably more complex.

The Doping Under the Emitter

Equation (5) can be solved graphically for the net doping under the emitter; this calculation was performed for several typical cases. Figure 5 shows the net doping under the emitter as a function of the base–collector crossover point. The difference between the crossover points is held constant at 0.03 mil. The plotted parameters are the outdiffused and erfc distributions with a maximum concentration of 5×10^{18} atoms per cubic centimeter. The calculation indicates that for a given collector penetration and a given base width, the doping under the emitter decreases with increasing collector penetration. It also shows that the doping under the emitter is insensitive to the impurity distribution.

Similar calculations were performed in which the surface concentration of the base layer was increased from 5×10^{18} to 10^{19} atoms per cubic centimeter. Although the surface concentration was increased by a factor of two, the doping under the emitter changed less than 10 per cent. For a given base width, the doping under the emitter is sensitive to the collector penetration and relatively insensitive to the surface concentration of the base or the type of distribution.

Electrical Reach-Through

One important parameter which can be calculated from curves such as those shown in Figures 4 and 5 and solutions of Poisson's equation[7] is an estimate of the voltage which can be applied before the collector depletion layer sweeps across the base to the emitter.

---

[7] H. Laurence and R. Warner, "Diffused Junction Depletion Layer Calculations," *Bell Syst. Tech. Jour.*, Vol. 39, p. 389, March, 1960.

Three steps are required in this calculation. First, the number of uncompensated impurities under the emitter must be evaluated, as follows:

$$B = \int_{x_1}^{x_2} (N_A - N_D)\, dx = \int_{x_1}^{x_2} \left(C_2 \operatorname{erfc} \frac{x}{2\sqrt{D_2 t_2}} - C_1 \operatorname{erfc} \frac{x}{2\sqrt{D_1 t_1}} - C_3 \right) dx, \tag{6}$$

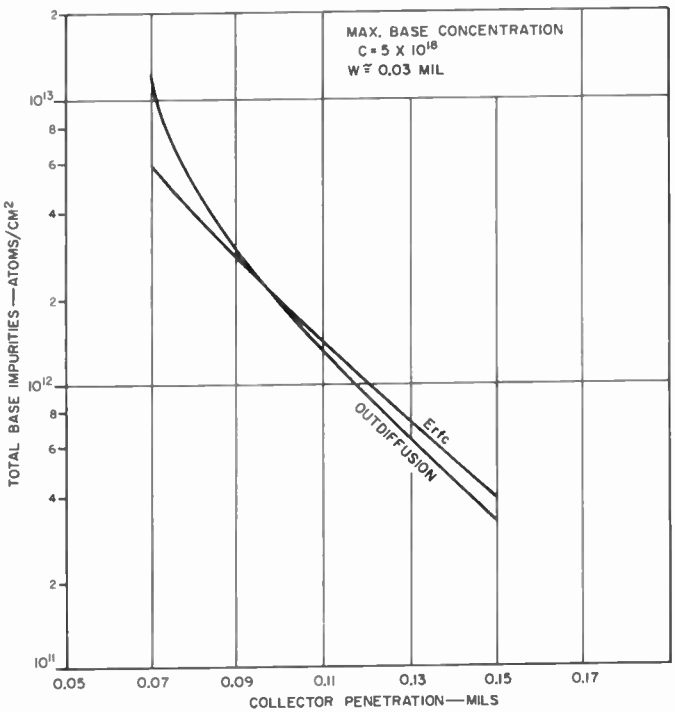

Fig. 5—The net doping under the emitter as a function of the base collector crossover point with the impurity distribution as the plotted parameter.

where x_1 and x_2 are the emitter and collector penetrations, respectively. B is the net doping under the emitter.

Second, to maintain space-charge neutrality, the space-charge layer will sweep out an equal number of impurities in the collector region. The spread of the space-charge layer into the collector region, x_{sc}, can be evaluated as follows:

$$B = \int_{x_1}^{x_2} (N_A - N_D)\, dx = \int_{x_2}^{x_{sc}} \left(C_2 \operatorname{erfc} \frac{x}{2\sqrt{D_2 t_2}} - C_3 \right) dx;\ x > x_2. \quad (7)$$

Finally, when x_{sc} is evaluated, it is possible to estimate from solutions of Poisson's equation[7] the value of the applied voltage which will cause the space-charge layer to sweep across the base to the emitter.

The results of these calculations for several important cases are shown in Figures 6 and 7. Figure 6 shows the reach-through voltage for silicon as a function of collector penetration for a constant cross-over point difference of 0.03 mil. The parameters plotted are the impurity distribution and two values of surface concentration. Because the reach-through voltage depends upon the doping under the emitter, it is insensitive to the surface concentration and type of impurity distribution. It is, however, very sensitive to collector penetration. To maintain the reach-through voltage in excess of 25 volts, the doping under the emitter must be greater than 2×10^{12} atoms per square centimeter.

Figure 6 indicates that the base width must be increased for deeper collector penetration to prevent electrical reach-through. For a constant doping under the emitter, the increase of base width with increasing collector penetration can be calculated from the following set of simultaneous, transcendental equations:

$$C_1 \operatorname{erfc} \frac{x_1}{2\sqrt{D_1 t_1}} - C_2 \operatorname{erfc} \frac{x_1}{2\sqrt{D_2 t_2}} + C_3 = 0, \quad (8)$$

$$C_1 \operatorname{erfc} \frac{x_2}{2\sqrt{D_1 t_1}} - C_2 \operatorname{erfc} \frac{x_2}{2\sqrt{D_2 t_2}} + C_3 = 0, \quad (9)$$

$$B - \int_{x_1}^{x_2} \left(C_1 \operatorname{erfc} \frac{x}{2\sqrt{D_1 t_1}} - C_2 \operatorname{erfc} \frac{x}{2\sqrt{D_2 t_2}} + C_3 \right) dx = 0. \quad (10)$$

Figure 7 shows the base width required to maintain the doping at 3×10^{12} atoms per square centimeter under the emitter as a function of collector penetration. The erfc case only was solved in order to derive the form of the base-width dependence upon collector depth; the results of the out-diffused case will not differ greatly. The surface concentration of the base layer is the parameter plotted. These curves were obtained from computer solutions of Equations (8), (9), and

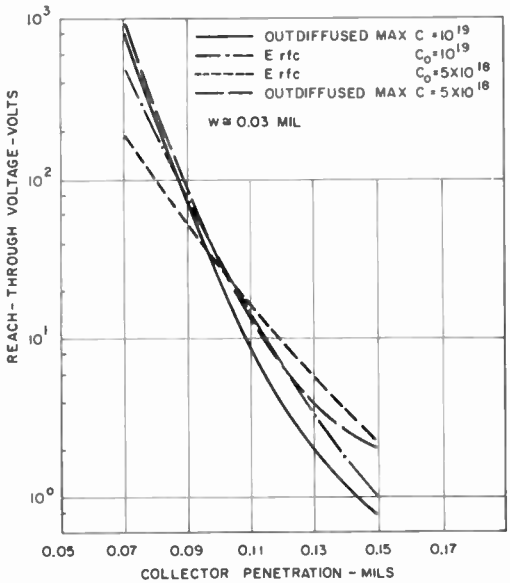

Fig. 6—The reach-through voltage as a function of collector penetration for silicon with a constant crossover point difference of .03 mil. The plotted parameter is the base impurity distribution and two values of surface concentration.

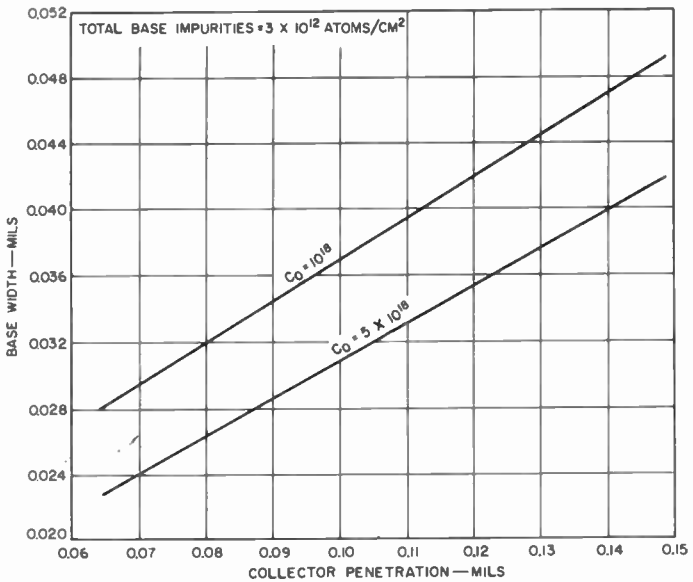

Fig. 7—Base width required to maintain a doping of 3×10^{12} under the emitter as a function of collector penetration with the surface concentration of the base layer as the plotted parameter for an erfc base distribution.

(10). The calculation indicates that the base width must be increased linearly with increasing collector penetration to prevent electrical reach-through. The base width must also be increased if the surface concentration is decreased.

Emitter Efficiency of Double-Diffused Transistors

One computation which can be obtained from the simultaneous solution of Equations (8), (9), and (10) is an estimate of the emitter efficiency for a double-diffused transistor structure. The emitter efficiency[8] is determined by the ratio of the doping in the emitter within a diffusion length of the emitter junction to the net doping[5] in the base. This ratio can be approximated as follows:

$$\beta = \frac{D_n \int_{\mu}^{x_1} (N_D - N_A)\, dx}{D_p \int_{x_1}^{x_2} (N_A - N_D)\, dx}. \qquad (11)$$

This ratio is equal to the transistor β (current gain) if there are no losses due to bulk or surface recombination; it can be considered to be the maximum obtainable β (when limited only by injection efficiency). For double-diffused transistors, Equation (11) can be rewritten as follows:

$$\beta = \frac{1}{B}\frac{D_n}{D_p}\int_{\mu}^{\tau_1}\left[C_1 \operatorname{erfc}\frac{x}{2\sqrt{D_1 t_1}} - C_2 \operatorname{erfc}\frac{x}{2\sqrt{D_2 t_2}} + C_3\right] dx, \qquad (12)$$

where B is the net doping in the base and μ is the diffusion length of minority carriers in the emitter. D_p/D_n, the diffusion constant ratio of the minority carriers, is approximately 1/12 for the silicon transistors considered here.

Figure 8 is a plot of the maximum common emitter current gain obtainable as a function of the diffusion length in the emitter for several values of the diffusion variables for the erfc impurity distribution. The deeper collector penetrations place a more severe re-

[8] W. Shockley, M. Sparks, and G. K. Teal, "P-N Junction Transistors," *Phys. Rev.*, Vol. 83, p. 151, July 1, 1951.

quirement on the diffusion length in the emitter. This effect is particularly important at high frequencies, where β may be limited by the transit time of minority carriers within a diffusion length of the emitter[9] rather than the lifetime.

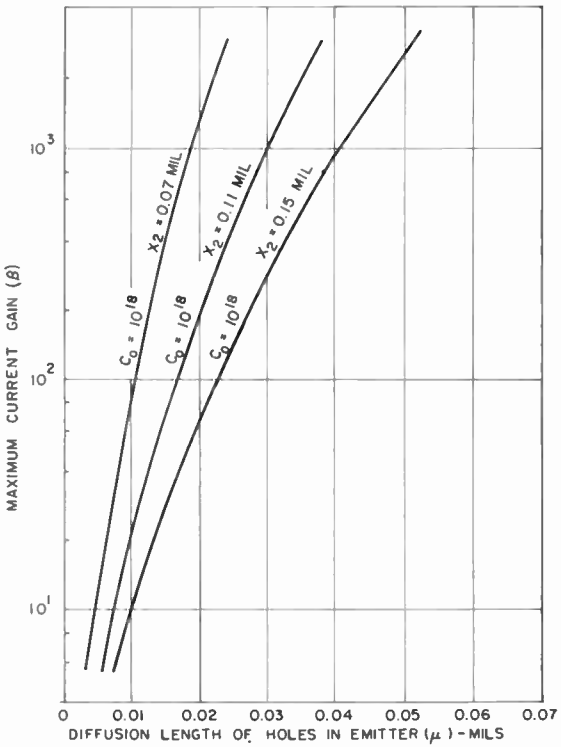

Fig. 8—The maximum beta of a double-diffused transistor as a function of the diffusion length in the emitter with several diffusion variables as the plotted parameters.

Base-Width Control in Double-Diffused Transistors

One technique of boron diffusion is the deposition of atoms on the surface of silicon at one temperature and redistribution of the atoms at a higher temperature. One suitable deposition technique confines the impurities in a platinum box.[10] This approach establishes the vapor

[9] H. L. Armstrong, "Current Gain of Junction Transistors," *Trans. I.R.E. PGED*, Vol. 6, p. 1, Jan., 1959.

[10] L. A. D'Asaro, "Diffusion and Oxide Masking in Silicon by the Box Method," *Solid-State Electronics*, Vol. 1, p. 3, March, 1960.

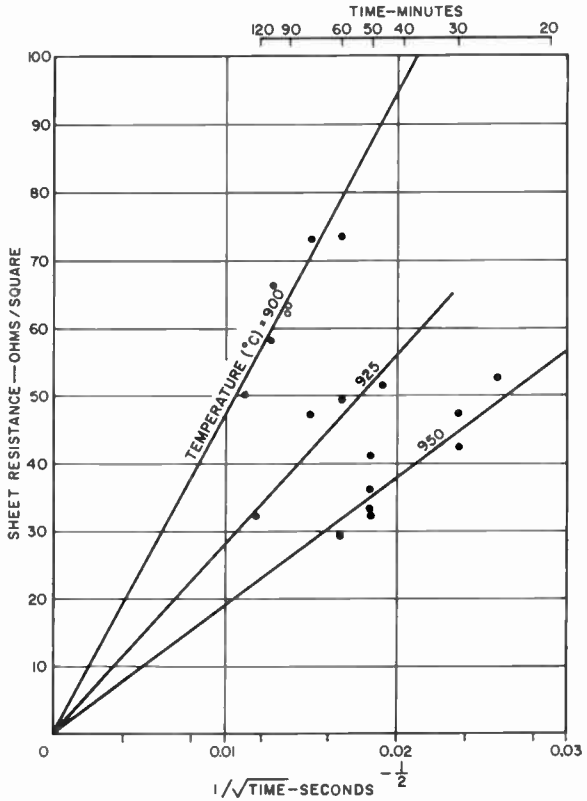

Fig. 9—The sheet resistance of the deposited boron layer as a function of diffusion time.

pressure of B_2O_3 above the surface of the silicon wafers, which are enclosed in a box or capsule. The limiting value of surface concentration is the solid solubility of boron in silicon at the deposition temperature.

Figure 9 shows the sheet resistance, R_s, in ohms per square as a

Table I

Temp. (°C)	Time (hrs.)	Z	D (cm^2/sec.)	K	R_1 (ohms per	R_2 square)
1125	2.5	3.2	6×10^{-13}	3×10^{-8}	50	300
1150	7.0	2.5	1×10^{-12}	2×10^{-8}	50	240
1200	0.5	2.5	3×10^{-12}	7×10^{-8}	100	280

function of time for three values of deposition temperature. If the B_2O_3 is considered an infinite source of boron and the surface concentration is assumed to be the solid solubility of boron in silicon at the deposition temperature, then the reciprocal square root of the slope of each line is proportional to the diffusion constant of boron in silicon. The diffusion constant was calculated for each case and presented for an assumed surface concentration of 3×10^{20}; results were found to be in agreement with Fuller's values.[11]

The conditions during the deposition operation determine the total number of impurities in the layer. During the redistribution step, the impurity profile is controlled. Two parameters which can be evaluated are the total number of impurities and the junction depth. From these two parameters[4] the impurity profile can be approximated. Table I shows values for Z and K evaluated from typical diffusion data (R_1 and R_2 are the sheet resistances after deposition and out-diffusion, respectively).

These data refer to a process in which oxide growth and redistribution occur simultaneously; the resulting distribution may be considerably different from the usual out-diffusion profile in the region near the surface where small differences are relatively unimportant. In the important region near the collector junction, the profile is rather insensitive to the way in which impurity atoms are removed from the crystal. Consequently, the results of Smits and Miller[4] can be used.

ACKNOWLEDGMENT

The authors acknowledge the advice and assistance of A. Blicher and the help of F. Herzfeld in programming and computing the problem.

[11] C. S. Fuller and J. A. Ditzenberger, "Diffusion of Donor and Acceptor Elements in Silicon," *Jour. Appl. Phys.*, Vol. 27, No. 5, p. 544, May 1956.

RCA TECHNICAL PAPERS†

Fourth Quarter, 1961

Any request for copies of papers listed herein should be addressed to the publication to which credited.

"Author's Comment 'The Amplitude Distribution and False Alarm Rate of Noise After Post-Detection Filtering'," S. Thaler and Coauthor, *Proc. I.R.E.* (October) (Correspondence) 1961

"Color Temperature Diagram," G. P. Kirkpatrick and Coauthor, *Jour. Opt. Soc. Amer.* (October) 1961

"Contribution a l'Etude de l'Emission Infrarouge dans le Germanium," J. I. Pankove, Thesis Presentees a la Faculte des Sciences de l'Universite de Paris (October) 1961

"Correction to 'Stable Low-Noise Tunnel-Diode Frequency Converter'," F. Sterzer and A. Presser, *Proc. I.R.E.* (October) (Correspondence) 1961

"Crystal Structure of Photoelectric Films of Cesium Antimonide," W. H. McCarroll, *Jour. Appl. Phys.* (October) (Letters to the Editor) 1961

"Determination of the Glide Elements and Recrystallization in InSb," M. S. Abrahams and G. W. Neighbor, *Trans. Metallurgical Soc. AIME* (October) 1961

"Energy-Level Model for High-Resistivity Gallium Arsenide," J. Blanc and L. R. Weisberg, *Nature* (October) 1961

"Fast-Risetime Excitation Scheme to Achieve Nonequilibrium and Amplifying Carrier Distributions," G. C. Dousmanis, *Jour. Appl. Phys.* (October) 1961

"Fundamental Reflectivity Spectrum of Semiconductors with Zinc-Blende Structure," M. Cardona, *Jour. Appl. Phys. Supplement* (October) 1961

"The Future of Pulse Radar for Missile and Space Range Instrumentation," D. K. Barton, *Trans. I.R.E. PGME* (October) .. 1961

"Investigation of the Electrochemical Characteristics of Organic Compounds—VIII. Hydrazine and Hydroxylamine Compounds," R. Glicksman, *Jour. Electrochem. Soc.* (October) 1961

"Majority Carrier Magnetosurface Effect," R. D. Larrabee, *Jour. Appl. Phys.* (October) 1961

"Personal Microphones," H. F. Olson, J. Preston, and J. C. Bleazey, *Jour. Aud. Eng. Soc.* (October) 1961

"Phonon Spectrum of Germanium-Silicon Alloys," R. Braunstein, A. R. Moore, and F. Herman, *Jour. Physical Soc. Japan* (October) 1961

"Some New Measurements of Infrared Luminescence in Tunnel Diodes," J. I. Pankove, *Jour. Electrochem. Soc.* (October) 1961

"A Study of Interference Effects in Magnetic Recording," J. G. Woodward and M. Pradervand, *Jour. Aud. Eng. Soc.* (October) 1961

"Super-Power U.H.F. Tubes," R. E. Reed and A. C. Tunis, *Electronics World* (October) 1961

† Report all corrections to *RCA Review*, RCA Laboratories, Princeton, N. J.

"Vidicon Light-Transfer Characteristics and Film Reproduction," R. G. Neuhauser, *Jour. S.M.P.T.E.* (October) 1961

"Determination of Contributions to the Residual Resistivity of Gallium at 4.2°K," L. R. Weisberg and R. M. Josephs, *Phys. Rev.* (October 1) 1961

"Enhancement of Superconductivity by Extraction of Normal Carriers," R. H. Parmenter, *Phys. Rev. Letters* (October 1) 1961

"Log-Log Presentation of Transistor Characteristics," J. Adams, *Electronics* (October 6) (Electronics Reference Sheet) 1961

"R-F Techniques for Controlled Thermonuclear Fusion," C. D. Allen, G. A. Senior, and S. M. Zollers, *Electronics* (October 27) 1961

"Author's Comment 'Tunnel-Diode Microwave Oscillators'," D. Sterzer and D. E. Nelson, *Proc. I.R.E.* (November) (Correspondence) 1961

"Communications — A Look Ahead," D. Sarnoff, *Signal* (November) 1961

"Control of Livestock Breeding in Sweden," T. I. Bradshaw, *Computers and Automation* (November) 1961

"Feed System for Clockwise and Counterclockwise Circular Polarization," S. G. Komlos, P. Foldes, and K. Jasinski, *Trans. I.R.E. PGAP* (November) (Communications) 1961

"Input Loading in Audio Amplifiers," A. M. Seybold, *Electronic Equipment Engineering* (November) 1961

"Modern TWT Focusing Methods," C. L. Cuccia, *Electronic Industries* (November) 1961

"The Non-Directional Aspect of Stereo," C. J. Hirsch, *Trans. I.R.E. PGBTR* (November) 1961

"Performance and Evaluation of Satellites Tiros I and Tiros II," S. Sternberg and A. Schnapf, *ARS Jour.* (November) 1961

"Phonetic Typewriter III," H. F. Olson and H. Belar, *Jour. Acous. Soc. Amer.* (November) 1961

"Preflight Checkout of Moon Rocket," R. G. Gillen, *Computers and Automation* (November) 1961

"A Solution for Certain Types of Partitioning Problems," M. H. Greenblatt, *The Mathematics Teacher* (November) 1961

"Quenching Effects and Negative Photoconductivity in Amorphous Selenium," J. Dresner, *Jour. Chem. Phys.* (November) 1961

"Value-Engineering — An Engineer's Heritage and Discipline," A. D. Zappacosta, *Trans. I.R.E. PGPEP* (November) 1961

"Radar Observation of Venus," I. Maron, G. Luchak, and Coauthor, *Science* (November 3) 1961

"Degenerate Germanium. II. Band Gap and Carrier Recombination," H. S. Sommers, Jr., *Phys. Rev.* (November 15) 1961

"Air Lubrication, a Development Tool," M. L. Levene, *Mechanical Engineering* (December) 1961

"Analysis of Double-Stream Interactions in the Presence of a Finite Axial Magnetic Field," B. Vural, *RCA Review* (December) .. 1961

"Antenna Noise Temperature in Plasma Environment," M. P. Bachynski, I. P. French, and G. G. Cloutier, *Proc. I.R.E.* (December) 1961

"An Automatic-Frequency-Controlled Phase-Shift-Keyed Demodulator," W. Hannan and T. Olson, *RCA Review* (December) .. 1961

"A Dynamic-Capacitor Electrometer Suitable for Measuring Electrophotographic Recording Media," E. C. Giaimo, *RCA Review* (December) 1961

"The Effect of a D-C Magnetic Field on the UHF Permeability and Losses of Some Hexagonal Magnetic Compounds," R. L. Harvey, I. Gordon, and R. A. Braden, *RCA Review* (December) 1961

"Effects on Impurity Content of Cropping Directionally Frozen Ingots," L. R. Weisberg, *Trans. Metallurgical Soc. AIME* (December) 1961

"An Electrical Analog for Electroluminescent Layers," S. M. Thomsen, *RCA Review* (December) 1961

"Electronic and Motion-Picture Systems in the Space Age," B. Kreuzer, *Jour. S.M.P.T.E.* (December) 1961
"The Enhanced-Scan Post-Acceleration Kinescope," H. B. Law, L. Davne, and E. G. Ramberg, *RCA Review* (December) 1961
"An Examination of the Power Losses in Tower Antennas as a Function of Galvanizing," G. H. Brown, *Broadcast News* (December) 1961
"Generalized Appleton-Hartree Equation for Any Degree of Ioniization and Application to the Ionosphere," I. P. Shkarofsky, *Proc. I.R.E.* (December) 1961
"High-Speed Logic Circuits Using Common-Base Transistors and Tunnel Diodes," J. J. Amodei and W. F. Kosonocky, *RCA Review* (December) 1961
"How to Align Microwave Antennas," J. B. Bullock, *Broadcast News* (December) 1961
"Measurement of Small, Fast Variations in Complex Permittivity at Ultra-High Frequencies," E. Fatuzzo, *Monograph No. 491 E, IEE* (British) (December) 1961
"A Method for the Measurement of Short Minority Carrier Diffusion Lengths in Semiconductors," A. M. Goodman, *Jour. Appl. Phys.* (December) 1961
"New 5KW VHF Television Transmitter," H. E. Small, *Broadcast News* (December) 1961
"New RCA-6DS4 Nuvistor Triode Improved Two-Meter Converter," R. M. Mendelson, *RCA Ham Tips* (December) 1961
"New Television Camera Tubes in Perspective," R. G. Neuhauser, *Jour. S.M.P.T.E.* (December) 1961
"New 20-KW FM Transmitter," I. H. Lubash, *Broadcast News* (December) 1961
"Optimum Binary FM Reception Using Discriminator Detection and I-F Shaping," A. A. Meyerhoff and W. M. Mazer, *RCA Review* (December) 1961
"Plasma Physics — An Elementary Review," M. P. Bachynski, *Proc. I.R.E.* (December) 1961
"The Purpose and Function of PGEWS," E. M. McElwee, *Proc. National Symposium on Engineering Writing and Speech*, Michigan (December) 1961
"The RCA TR-11 A 'Compact' TV Tape Recorder," H. H. Klerx, *Broadcast News* (December) 1961
"Stability Criteria for a Tunnel-Diode Amplifier," H. Boyet, D. Fleri, and C. A. Renton, *Proc. I.R.E.* (December) (Correspondence) 1961
"Super-Power U.H.F. Tubes," R. E. Reed and A. C. Tunis, *Electronics World* (December) (Letters from our Readers) 1961
"Technique for Preparing Fine Mesh of Refractory Metals," J. Gross, *Rev. Sci. Instr.* (December) (Notes) 1961
"Thermal Emissivity and Conductivity of Alumina Heater Coatings," N. Rudnick and J. J. Carrona, *RCA Review* (December) 1961
"Transfluxor Frequency Memory," A. G. Samusenko, *RCA Review* (December) 1961
"Transistors as RF Power Amplifiers," J. B. Fisher, *RCA Ham Tips* (December) 1961
"Inverted Nature and Significance of Negative-Mass Landau Levels," G. C. Dousmanis, *Phys. Rev.* (December 1) 1961
"Instabilities of a Cylindrical Electron-Hole Plasma in a Magnetic Field," M. Glicksman, *Phys. Rev.* (December 15) 1961
"Properties of Injected Plasmas in Indium Antimonide," Betsy Ancker-Johnson, R. W. Cohen, and M. Glicksman, *Phys. Rev.* (December 15) 1961
"Four Advanced Computers — Key to Air Force Digital Data Communication System," R. J. Segal and H. P. Guerber, *Proc. Eastern Joint Computer Conf.*, Vol. 20, p. 264, The Macmillan Co., New York 1961

"The Logic Design of the FC-4100 Data-Processing System," W. A. Helbig, A. Schwartz, C. S. Warren, W. E. Woods, and H. S. Zieper, *Proc. Eastern Joint Computer Conf.*, Vol. 20, p. 158, The Macmillan Co., New York 1961

"The Plasma Triode — A Low Temperature Thermionic Converter," W. B. Hall and K. G. Hernqvist, *15th Ann. Proc. Power Sources Conf.* 1961

"A Versatile Man-Machine Communication Console," P. B. Lazovick, J. C. Trost, A. W. Reickord, and Coauthor, *Proc. Eastern Joint Computer Conf.*, Vol. 20, p. 166, The Macmillan Co., New York 1961

AUTHORS

S. B. ADLER received the B.S. degree cum laude in physics from the University of Massachusetts. Afterwards, he attended the University of Pennsylvania and later Temple University, where he earned the Ph.D. degree in physics. He spent five years in the Army during World War II, holding the rank of Major in the Signal Corps. Prior to joining RCA, Dr. Adler was an electronics engineer with Link Aviation Inc. His principle activities at RCA have been in the fields of precision tracking radar, and missile range instrumentation. He was project engineer for the Army fire control system for the Terrier missile, was in charge of the development of the AN/FPS-16 monopulse radars, the tracking and guidance radars for the Talos weapon system, and was later manager of the DAMP system activity, a scientific program for measuring ballistic missile re-entry phenomena.

Dr. Adler is a member of Phi Kappa Phi Honor Society, the American Physical Society, and the Institute of Radio Engineers.

CHARLES R. FUSELIER received the B.S. degree from Louisiana State University in 1958. After completing one year of graduate work in physics at Columbia University, he joined the Computer Device Development group of the RCA Semiconductor Division at Somerville, N. J. where he was involved in semiconductor device design. In the fall of 1961, he joined the RCA Laboratories at Princeton.

Mr. Fuselier is a member of the American Physical Society.

E. C. GIAIMO served in the U.S. Navy as an Electronic Technician from 1943 to 1946. In this capacity, he was a laboratory assistant in microwave research at the Naval Research Laboratory, Washington, D. C., from 1944 to 1946. He received a B.S.E. in 1950 and an M.S.E. in 1955 in electrical engineering from Princeton University. He joined RCA Laboratories in 1951, where he made contributions to ruggedization of traveling-wave-tube structures, germanium purification and testing devices. He has been actively associated with electrophotographic research since 1952. From 1957 to 1959 he was assigned to the technical staff of C Stellarator Associates to perform system specification and coordination duties in the design of a thermonuclear fusion reactor. Mr. Giaimo is a member of the Institute of Radio Engineers and Sigma Xi.

ADOLPH PRESSER received the B.E.E. degree from the Institute of Technology, Vienna, Austria, in 1950 and the M.E.E. degree from the Polytechnic Institute of Brooklyn, N. Y., in 1961, where he is presently studying for the D.E.E. degree. He was a production engineer for Schrack A.G. in Vienna, Austria, from 1950 to 1952, was employed in industry from 1953 to 1954, and was a development engineer for the Allied Control Co., in New York, N. Y., from 1954 to 1959. He joined the RCA Electron Tube Division in 1959 and is now a Member of the Technical Staff of the Microwave Applied Research group at the RCA David Sarnoff Research Center in Princeton, N. J. As a member of the Microwave Electronics section of this group, he is engaged in the development of various solid-state microwave devices. This work includes the design and development of parametric amplifiers, tunnel-diode amplifiers, tunnel-diode frequency converters, and tunnel-diode oscillators.

DANIEL RAUSCHER received the B.S. degree in physics from Pennsylvania State University in 1951. He did graduate work and served as a teaching assistant at Cornell University until 1954. He was employed by the Capehart-Farnsworth Corporation from 1954 to 1957, when he joined Columbia Broadcasting System Laboratories. Since 1958 he has been a device development engineer in the Semiconductor and Materials Division of RCA, where his efforts have been concentrated on both germanium and silicon high-frequency switching transistors. Mr. Rauscher is a member of Phi Beta Kappa and Sigma Pi Sigma.

WIESLAW W. SIEKANOWICZ received the B.S. degree in Electrical Engineering from the Imperial College of Science and Technology, London University, England, in 1948, the M.S. degree from Columbia University in 1950, and the D.E.E. degree from the Polytechnic Institute of Brooklyn in 1960. He joined the RCA Electron Tube Division at Harrison, N. J. in July 1950 and transferred to the David Sarnoff Research Center, Princeton, in 1956. He has specialized in the fields of traveling-wave tubes, klystrons, and electron beams. He is now group leader in high-power electronics. Dr. Siekanowicz is a member of the Institute of Radio Engineers and Sigma Xi.

FRED STERZER received the B.S. degree in physics from the College of the City of New York in 1951, and the M.S. and Ph.D. degrees from New York University in 1952 and 1955, respectively. From 1952 to 1953 he was employed by the Allied Control Corporation, New York, N. Y. During 1953 and 1954 he was an instructor in physics at the Newark College of Engineering, Newark, N. J., and a research assistant at New York University. He joined the RCA Tube Division in Harrison, N. J., in October, 1954, and was transferred to the Microwave Applied Research Group in Princeton, N. J., in 1956. He is now group leader in microwave physics, working in the field of microwave spectroscopy, traveling-wave tubes, backward-wave oscillators, solid-state microwave amplifiers, oscillators and converters, microwave computing circuits, and r-f light modulators.

Dr. Sterzer is a member of Phi Beta Kappa, Sigma Xi, and the American Physical Society.

IVAN H. SUBLETTE received a B.S. degree in electrical engineering from Purdue University in 1949 and M.S. and Ph.D. degrees from the University of Pennsylvania in 1951 and 1957, respectively. Dr. Sublette joined an advanced development group at the Camden plant of RCA in 1949. After working for two years on the application of television techniques to radar systems, he entered the digital computing field. He worked on diode switching circuits, coincident-current magnetic memories, magnetic logic, and contributed to the logic design for the first electronic digital computer developed by RCA. Later, he developed techniques for processing radar data in digital computers and worked on computer systems engineering for the BMEWS program. In 1959, he transferred to the RCA Laboratories, where he is now directing research on character recognition.

Dr. Sublette is a member of the Institute of Radio Engineers, the Association for Computing Machinery, Eta Kappa Nu, and Tau Beta Pi.

JURI TULTS received the B.S. and M.S. degrees in electrical engineering from Purdue University in 1954 and 1955, respectively. Since 1955 he has been employed by RCA Laboratories, where he has been engaged in research on color television and infra-red imaging systems, and most recently on character recognition systems. He has developed an optical scanner for character recognition and has contributed to the writing of computer programs which simulate the logic of reading machines. Mr. Tults is a member of the Institute of Radio Engineers, Eta Kappa Nu, and Tau Beta Pi.

HAROLD S. VELORIC received the B.A. degree from the University of Pennsylvania in 1951 and the M.S. and Ph.D. degrees from the University of Delaware in 1952 and 1954, respectively. He joined the Technical Staff of Bell Telephone Laboratories, Murray Hill, N. J., in 1954, and was engaged in the development of various types of silicon diodes. In 1958 he joined the RCA Semiconductor and Materials Division in Somerville, N. J., where he is Manager of design and development work on silicon computer devices. This activity includes development and production of all high-frequency silicon switching transistors, as well as all computer silicon devices.

Dr. Veloric is a member of the American Chemical Society, the Electrochemical Society, and the Institute of Radio Engineers.

PAUL P. WEBB graduated from McGill University with a B. Eng. degree in Engineering Physics in 1955, and was awarded an Athlone Fellowship to study in the United Kingdom from 1955 to 1957. He received the M.Sc. degree in Engineering from the University of London, and the Diploma of Imperial College in 1957. Mr. Webb joined the staff of the RCA Victor Research Laboratories of Canada in February 1958. He has been engaged in research on semiconductor devices including the study of voltage breakdown phenomena in diffused silicon p-n junctions and the development of silicon-junction nuclear particle detectors. Mr. Webb is a member of the Institute of Radio Engineers.

ROBERT L. WILLIAMS obtained the B.Sc. in Mathematics and Physics in 1951 from the University of Western Ontario, then transferred to the University of British Columbia where he obtained the M.A. for studies on crystal counters, and the Ph.D. (1955) for studies on the electrical properties of liquid argon and helium ionized by alpha particles. From 1955 to November 1959, when he joined RCA Victor, Canada, he worked in the infrared section of the Canadian Armament Research and Development Establishment. At RCA Victor, as head of the Nuclear Devices group, he has been engaged in research on the diode and transistor forms of semiconductor nuclear particle detectors, and on large area photo diodes.